

University of Groningen

## Chalcogenides by Design

Kooi, Bart J.; Wuttig, Matthias

*Published in:*  
Advanced materials

*DOI:*  
[10.1002/adma.201908302](https://doi.org/10.1002/adma.201908302)

**IMPORTANT NOTE: You are advised to consult the publisher's version (publisher's PDF) if you wish to cite from it. Please check the document version below.**

*Document Version*  
Publisher's PDF, also known as Version of record

*Publication date:*  
2020

[Link to publication in University of Groningen/UMCG research database](#)

*Citation for published version (APA):*

Kooi, B. J., & Wuttig, M. (2020). Chalcogenides by Design: Functionality through Metavalent Bonding and Confinement. *Advanced materials*, 32(21), [1908302]. <https://doi.org/10.1002/adma.201908302>

**Copyright**

Other than for strictly personal use, it is not permitted to download or to forward/distribute the text or part of it without the consent of the author(s) and/or copyright holder(s), unless the work is under an open content license (like Creative Commons).

**Take-down policy**

If you believe that this document breaches copyright please contact us providing details, and we will remove access to the work immediately and investigate your claim.

*Downloaded from the University of Groningen/UMCG research database (Pure): <http://www.rug.nl/research/portal>. For technical reasons the number of authors shown on this cover page is limited to 10 maximum.*

# Chalcogenides by Design: Functionality through Metavalent Bonding and Confinement

Bart J. Kooi\* and Matthias Wuttig\*

**A unified picture of different application areas for incipient metals is presented. This unconventional material class includes several main-group chalcogenides, such as GeTe, PbTe, Sb<sub>2</sub>Te<sub>3</sub>, Bi<sub>2</sub>Se<sub>3</sub>, AgSbTe<sub>2</sub> and Ge<sub>2</sub>Sb<sub>2</sub>Te<sub>5</sub>. These compounds and related materials show a unique portfolio of physical properties. A novel map is discussed, which helps to explain these properties and separates the different fundamental bonding mechanisms (e.g., ionic, metallic, and covalent). The map also provides evidence for an unconventional, new bonding mechanism, coined metavalent bonding (MVB). Incipient metals, employing this bonding mechanism, also show a special bond breaking mechanism. MVB differs considerably from resonant bonding encountered in benzene or graphite. The concept of MVB is employed to explain the unique properties of materials utilizing it. Then, the link is made from fundamental insights to application-relevant properties, crucial for the use of these materials as thermoelectrics, phase change materials, topological insulators or as active photonic components. The close relationship of the materials' properties and their application potential provides optimization schemes for different applications. Finally, evidence will be presented that for metavalently bonded materials interesting effects arise in reduced dimensions. In particular, the consequences for the crystallization kinetics of thin films and nanoparticles will be discussed in detail.**

unprecedented progress of the semiconductor industry and information technology. Yet, we have reached a stage where a simple evolution along established research lines might no longer bear much fruit. Advanced functional materials require increasingly complex and demanding property combinations. Their optimization would thus benefit from novel concepts. In thermoelectrics, which convert waste heat into electricity, for example, materials must show the unusual combination of high electrical and small thermal conductivity. This is demanding since a high electrical conductivity is usually accompanied by a high thermal conductivity. In phase change materials (PCMs) employed for data storage and processing, materials are required which possess a pronounced contrast in optical and/or electrical properties between two different states. Usually one of these states is a metastable one, which is typically amorphous, while the second state is then stable crystalline.

## 1. Introduction

The ability to produce and process materials has shaped human progress for centuries. Advances in the understanding and manufacturing of semiconductors have enabled the


The metastable state has to be stable at room temperature and slightly above for 10 years; but it should crystallize, i.e., return to the stable crystalline state in a few nanoseconds if heated to temperatures of typically around 500 °C. The combination of pronounced property contrast and hence presumably different atomic arrangements in the two different phases, yet rapid crystallization is indicative for an unusual correlation of chemical bonding, atomic arrangement, and resulting properties, including crystallization kinetics. Topological insulators, expected to help realize novel electronic functionalities, possess topologically protected spin-polarized surface states with high mobility. These states should govern the sample conductivity, if the bulk is insulating.

This raises the question how these demanding requirements can be met and how superior materials can be identified. A number of different approaches have been developed in the past two decades to meet these needs. Combinatorial material synthesis, i.e., the fast preparation of stoichiometric libraries and their efficient analysis to identify superior compounds, has already been promoted over two decades ago.<sup>[1,2]</sup> While this scheme has indeed been successful in improving certain materials such as metal hydrides for hydrogen storage<sup>[3]</sup> and benchmarking electrocatalysts for solar water splitting,<sup>[4]</sup> for many material classes still empirical optimization schemes are employed. Machine learning is an emerging strategy to identify materials with a unique property portfolio.<sup>[5–7]</sup> This novel

Prof. B. J. Kooi  
Zernike Institute for Advanced Materials  
University of Groningen  
Nijenborgh 4, Groningen 9747 AG, the Netherlands  
E-mail: B.J.Kooi@rug.nl

Prof. M. Wuttig  
Institute of Physics IA  
RWTH Aachen University  
Aachen 52074, Germany  
E-mail: wuttig@physik.rwth-aachen.de

Prof. M. Wuttig  
JARA-Institute: Energy-Efficient Information Technology (Green IT)  
Forschungszentrum Jülich GmbH  
Jülich 52428, Germany

 The ORCID identification number(s) for the author(s) of this article can be found under <https://doi.org/10.1002/adma.201908302>.

© 2020 The Authors. Published by WILEY-VCH Verlag GmbH & Co. KGaA, Weinheim. This is an open access article under the terms of the Creative Commons Attribution-NonCommercial License, which permits use, distribution and reproduction in any medium, provided the original work is properly cited and is not used for commercial purposes.

DOI: 10.1002/adma.201908302

approach has undoubtedly huge potential, but at present it is unclear which limits regarding an in-depth material's understanding this approach will run into. However, note that a systematic understanding of materials has already been strived for in the 1970s, when material maps<sup>[8,9]</sup> were introduced to explain the structure and properties of solids. Given the success in the quantum mechanical (QM) description of solids in the last half century, it seems reasonable to revisit such approaches building on recent advances in quantum-chemical tools and concepts. This could help in employing chemical intuition and understanding to develop superior materials.

The present review is structured in the following way. Section 2 focuses on multivalent bonding, starting from a novel type of map derived from quantum-mechanical calculations (Section 2.1), subsequently macroscopic physical properties are addressed that act as fingerprints of bonding (Section 2.2), followed by the discussion of a unique bond breaking mechanism for an unconventional class of materials ("incipient metals") as observed by atom probe tomography (Section 2.3). In Section 2.4 different material maps and their power to separate different bonds are presented, while in Section 2.5 the unconventional properties of incipient metals are derived from a small number of assumptions on their atomic arrangement and electronic structure. In Section 2.6, we demonstrate that multivalent bonding constitutes an independent bonding mechanism, which differs from resonant bonding as encountered in benzene, graphite, and graphene. The link from bonding mechanisms to applications is discussed in Section 2.7, while thin film effects for GeTe and SnTe are presented in Section 2.8. Section 3 addresses nanoscale confinement with particular emphasis on the crystallization temperature of phase-change materials and focuses on confinement in thin films (Section 3.1) and nanoparticles (Section 3.2). Finally, Section 4 provides a short outlook on next developments in these two fields addressed in Sections 2 and 3 and on the effect of nanoscale confinement on multivalent bonding.

## 2. Introducing a New Bonding Mechanism: Multivalent Bonding

### 2.1. The Power of Maps to Separate Bonding Mechanisms and Classify Materials

Material scientists and solid-state physicists frequently relate material properties to the arrangement of the constituting atoms of the sample. Thus they exploit the intimate relationship between structure and properties to explain advanced functional materials. Both properties and the atomic arrangement can be measured with very high accuracy by a multitude of techniques. Hence, structure–property relationships have been developed thoroughly and are frequently employed. It is also generally accepted that the atomic arrangement in solids is a result of the underlying chemical bonds between adjacent atoms. Therefore, tailoring bonds between atoms should directly enable modifying the atomic arrangement and thus the resulting material properties. Interesting enough, this approach has not been frequently utilized in recent years. One key obstacle on this path is the difficulty to precisely quantify the nature of chemical bonds, leading



**Bart J. Kooi** obtained his Ph.D. degree in materials science in 1995 from Delft University of Technology, Netherlands and worked since then at the University of Groningen (Netherlands) as assistant, associate, and full professor, starting in 2009 his own research group Nanostructured Materials and Interfaces within the Zernike Institute for Advanced Materials. His main research interests are nanostructure–property relations, advanced transmission electron microscopy, interfaces, phase transformations, and telluride- and antimonide-based materials for thermoelectric and phase-change memory applications.



**Matthias Wuttig** received his Ph.D. in physics in 1988 from RWTH Aachen/Forschungszentrum Jülich. He was a visiting professor at several institutions including Lawrence Berkeley Laboratory, CINaM (Marseille), Stanford University, Hangzhou University, IBM Almaden, Bell Labs, DSI in Singapore and the Chinese Academy of Sciences in Shanghai. In 1997, he was appointed Full Professor at RWTH Aachen. Since 2011, he has been heading a collaborative research center on resistively switching chalcogenides (SFB 917), funded by the DFG.

to controversies which are as old as the entire discipline of quantum chemistry.<sup>[10,11]</sup> Indeed, bonding is usually defined heuristically, e.g., through observable properties, or in the van Arkel/Ketelaar triangle,<sup>[12,13]</sup> but there is no QM operator for "bonding." Nevertheless, the concept of chemical bonding is extremely useful, since it can help to understand and classify the property portfolio of different material classes.

Fortunately, there has also been significant progress in recent years, describing and quantifying bonding in solids, employing the Quantum Theory of Atoms in Molecules (QTAIM).<sup>[14]</sup> In this Quantum Chemical Topology scheme, which can also be used for crystals, the solid can be divided into nonoverlapping domains corresponding to quantum atoms.<sup>[15]</sup> Various quantities have been suggested within this framework to characterize the electron distribution. The first one is the domain population which is derived from the electron density and yields the effective atomic charge. Compared with the number of electrons of the corresponding atom, i.e., the atomic number, this quantity hence characterizes the transfer of charge to/from this atom. The second one is the delocalization index (DI), which

characterizes the degree of electron delocalization between the corresponding domains.<sup>[16,17]</sup> This quantity can be interpreted as the covalent bond order between adjacent atoms. It is derived from the conditional probability, which determines the probability of finding an electron at position  $r_2$ , while the second electron is located at position  $r_1$ , and which is derived from one- and two-electron densities. In the following, two related quantities will be employed to characterize bonding in solids. The first one is the number of electrons transferred to/from an atom. In simple binary solids, where every anion is only surrounded by cations and we have equal number of anions and cations, it is sufficient to consider the norm of the charge transferred, which is called “electrons transferred” in **Figure 1**. The second quantity we employ is twice the delocalization index between neighboring atoms. Hence, we consider the number of electrons shared between these atoms instead of their bond order. This might appear at first sight less appealing, since the classical view of covalent bond formation is the formation of electron pairs as suggested originally by Lewis.<sup>[18]</sup> Yet, it stresses the view that electrons can either be transferred to or shared between adjacent atoms. In Figure 1, these two quantities are depicted in a 2D map for a large number of elemental and simple binary solids.<sup>[19]</sup>

It has to be stressed that the results of these computations only depend weakly on the details of the calculations, i.e., they are rather robust. Comparing the results of two computational codes (DGRID<sup>[20]</sup> and critic2<sup>[21]</sup>) leads to deviations of about 0.01 for the number of electrons transferred and shared for SnTe. This deviation is characterized by the size of the red ellipse in Figure 1. It hence seems fair to conclude that even with improved computational schemes, we do not need to worry that a revised map would look very different. Still, it would be highly desirable to perform systematic studies of possible differences between various quantum-chemical codes such as

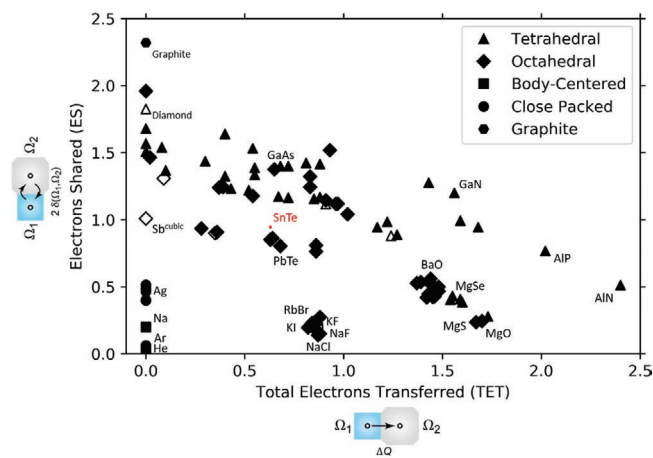


**Figure 1.** A 2D materials map using the total number of electrons transferred ( $x$ -axis) and the number of electrons shared between adjacent atoms ( $y$ -axis) as coordinates for a large number of solids. Triangles, diamonds, squares, circles, and hexagons are tetrahedrally bonded solids, octahedrally coordinated structures, body-centered solids, close-packed metals as well as graphite, respectively. Filled and open symbols represent thermodynamically stable and metastable phases. The small red ellipse represents the variation of the number of electrons shared and transferred for SnTe calculated with two different programs.<sup>[20,21]</sup>

DGRID and critic2. One can ponder which information can be obtained from the map displayed. The first striking observation is the clustering of points in certain regions of the map. The solids of noble gases such as He, and Ar, for example, as well as Ne, Kr, and Xe (not shown), are located in the same region of the map. This lower left corner is characterized by vanishing charge transfer and minor electron sharing. This is in line with textbook knowledge, which argues that the solids of noble gases are held together by weak van der Waals forces.

On the other hand, ionic solids such as NaCl or MgO are found in the lower region of the map towards the right side. They are characterized by significant charge transfer but only small electron sharing. Again, this is in line with common knowledge which states that ionic solids are held together by the Coulomb attraction of the oppositely charged ions. However, this information is obtained in Figure 1 from quantum topological concepts employing solutions of the Schrödinger equation, i.e., it is deeply rooted in quantum mechanics instead of empirical quantities. Notably, the data points for the ionic compounds cluster in two regions. The alkali halides are found in the first cluster, centered around an electron transfer of about 0.8 to 0.85, while II–VI compounds are found in the second group, characterized by an electron transfer of about 1.5. Hence, one might argue that the II–VI are more ionic than the alkali halides. However, the maximum charge transfer of these compounds is governed by the formal oxidation state of the constituting ions, which is two for the II–VI compounds, but only one for the alkali halides. It is hence evident to develop a new map in which the electron transfer of the atoms involved is divided by the formal oxidation state. The division by the oxidation state is unproblematic for most solids, but examples such as multivalent ions or certain intermetallics such as AuTe<sub>2</sub> resist the simple assignment of a formal oxidation state. In this case, maps like the one displayed in Figure 1 have to be utilized to characterize electron sharing and transfer. In Figure 1S (Supporting Information), obtained by dividing the electrons transferred by the formal oxidation state, ionic compounds now form one large cluster centered around a renormalized electron transfer of about 0.8.

On the other hand, elemental semiconductors or insulators like Si or diamond feature no charge transfer but share nearly 2 electrons. They, hence, approach the limit of an electron pair, suggested by Gilbert Lewis as the building block of covalent bonds. Metals finally are characterized by small or vanishing charge transfer and a small fraction of shared electrons, in line with their delocalized electrons and electron-deficit bonding. Hence, by now we have identified regions of ionic, covalent, metallic and van der Waals bonding in Figure 1S (Supporting Information).

However, there are materials located in two regions, to which we have not yet assigned a bonding mechanism. Compounds such as InP, ZnS, PbO, ZnO, GaN, or AlN lie on or close to the connecting line between perfect covalence (no electron transfer, sharing of 2 electrons) and perfect ionic bonding (no sharing of electrons, complete transfer of valence electrons). Hence, there apparently exists a continuous transition between ionic and covalent bonding. Again, this is in line with the view that, e.g., ZnO and GaN are neither fully covalent nor fully ionic compounds, but are instead frequently denoted as polar

semiconductors, which possess an ionic and covalent bonding contribution.

The only remaining group of materials that is now left without an assigned bonding mechanism contains chalcogenides such as GeTe, PbSe, Sb<sub>2</sub>Te<sub>3</sub>, and AgSbTe<sub>2</sub>. These materials find application as phase change materials, thermoelectrics and topological insulators. This makes it even more interesting to identify their bonding mechanism. Their location in the map implies at first sight that their bonding mechanism is intermediate between metallic and covalent or ionic bonding, an impression that needs to be refined later. Hence, how could this bonding mechanism be classified better?

## 2.2. Physical Properties as Fingerprints of Bonding

One can also turn this question around and ponder how many different physical properties are needed to distinguish the different bonding mechanisms. In doing so, we will focus on “the big three,” i.e., the three strong bonds in solids stemming from ionic, metallic, and covalent interactions. Clearly, the electrical conductivity can help to distinguish metals from the other two bonding mechanisms. However, this is not sufficient to distinguish between ionic and covalent bonding. To differentiate between these two, the effective coordination number (ECoN)<sup>[22]</sup> can be employed, but also other properties such as the optical dielectric constant often differ. In total, we suggest to focus on five different properties, which together act as bond indicators and provide a clear fingerprint of the three different bonding mechanisms.<sup>[23]</sup> These five different material properties are summarized in **Table 1**, which provides a 5D property vector of different bonding mechanisms.

Crystalline phase change materials like GeTe, Sb<sub>2</sub>Te<sub>3</sub>, or Ge<sub>2</sub>Sb<sub>2</sub>Te<sub>5</sub> possess a unique property portfolio. Surprisingly, these materials also appear useful for applications as thermoelectrics.<sup>[24]</sup> These materials are neither located in the region where metals are found, nor are they located on the line between ionic and covalent materials. This raises the question which bonding mechanism they utilize. All three compounds have electrical

conductivity values between the ones of metals and covalently bonded solids. Their effective coordination number (ECoN) is incompatible with the 8-N rule, which states that the number of nearest neighbors is determined by the number of valence electrons (N). According to this rule, the Ge and Te atoms in GeTe should have three nearest neighbors. Instead, the effective coordination number is closer to 5, signaling a significant deviation from ordinary covalent bonding. In addition, crystalline phase change materials like GeTe or Ge<sub>2</sub>Sb<sub>2</sub>Te<sub>5</sub> are characterized by high values of the optical dielectric constant  $\epsilon_{\infty}$ . Furthermore, these crystalline phases possess large values of the Born effective charge  $Z^*$ , a measure of the chemical bond polarizability, which is indicative for a strong electron–phonon coupling. This explains why several crystalline phase change materials are also superconductors. Finally, they are characterized by high values of the Grüneisen parameter for the transverse optical modes,  $\gamma_{TO}$ . This is a sign for very anharmonic behavior, which helps to understand why these materials have such low thermal conductivities, which benefits their application as thermoelectrics. It is important to note that the property vector displayed for materials like GeTe or PbTe is not a combination of the property vectors of other bonding mechanisms such as covalent, ionic and metallic bonding. This can be seen for example by a comparison of typical values of the Grüneisen parameter  $\gamma_{TO}$ . It is high for materials such as GeTe or PbTe, while materials with metallic or with covalent bonding generically show low values of  $\gamma_{TO}$ . Therefore, the bonding in GeTe cannot be considered a bonding just at the boundary between covalent and metallic bonding. One might still wonder, if the bonding in GeTe or PbTe could be a nonlinear combination of the properties of, e.g., metallic and covalent bonding. However, we are not aware of any other region between two bonding mechanisms that is observed in nature, where such a nonlinearity is observed. Hence, it seems advisable to consider bonding in GeTe or PbTe as a unique and novel bonding mechanism, distinctively different from covalent and metallic bonding.

Since this bonding mechanism seems to be related to covalent bonding but transcends its limits, it has been coined meta-valent (MVB), where the Greek word “meta” indicates

**Table 1.** Property-based “fingerprints” to define bonding in inorganic materials.<sup>[23]</sup> The fingerprint for meta-valent solids is a combination of five different identifiers, all of which need to be present in a given material (e.g., NaCl and PbTe have the same structural identifier, but the electronic conductivity in NaCl is extremely low).

Bonding property identifier	Ionic (e.g., NaCl, MgO)	Covalent (e.g., Si, GaAs)	Meta-valent (incipient metals, e.g., GeTe, PbTe)	Metallic (e.g., Cu, NiAl)
Electronic conductivity (electrical identifier)	Very low ( $<10^{-8}$ S cm <sup>-1</sup> )	Low to moderate ( $10^{-8}$ – $10^2$ S cm <sup>-1</sup> )	Moderate ( $10^1$ – $10^4$ S cm <sup>-1</sup> )	High ( $>10^5$ S cm <sup>-1</sup> )
Coordination number <sup>a)</sup> (structural identifier)	4 (ZnS), 6 (NaCl), 8 (CsCl)	8-N rule typically satisfied	8-N rule not satisfied	8 (bcc), 12 (hcp/fcc)
Optical dielectric constant $\epsilon_{\infty}$ (optical identifier)	Low ( $\approx 2$ – $3$ )	Moderate ( $\approx 5$ – $15$ )	High ( $>15$ )	– <sup>b)</sup>
Born effective charges $Z^*$ (chemical bond polarizability)	Low (1–2)	Moderate (2–3)	High (4–6)	Vanishes (0)
Mode specific Grüneisen parameters (anharmonicity)	Moderate (2–3)	Low (0–2)	High ( $>3$ )	Low (0–2)

<sup>a)</sup>For ionic and metallic systems, representative structure types are given, but there are many others especially for multinary systems (e.g., in Zintl phases); <sup>b)</sup>This indicator is not normally applicable to the metallic state. Reproduced with permission.<sup>[23]</sup> Copyright 2018 RWTH Aachen University. Published by WILEY-VCH.

that this bonding is beyond or adjacent to covalent bonding. This wording also refers to the proximity to both metallic and covalent bonding in the map. Yet, it has to be emphasized that metavalent bonding is not a mixture (mélange) of metallic and covalent bonding, but differs fundamentally from these two as well as ionic bonding. The materials which utilize this bonding mechanism have been coined incipient metals. Interestingly, they possess a property portfolio which makes them attractive for a variety of applications including phase change materials, thermoelectrics, topological insulators and photonic devices. We will return to their application potential later. To conclude this section, we replot Figure 1S, but now assign the different symbols a color which denotes the corresponding property portfolio and hence bonding mechanism. This is displayed in Figure 2, where materials employing either metallic, ionic and covalent bonding are located in different regions of the map. Incipient metals, such as GeTe, Bi<sub>2</sub>Se<sub>3</sub> or AgSbTe<sub>2</sub> are found in a well-defined region between ionic, covalent and metallic bonding, where MVB is employed.

### 2.3. A Unique Bond Breaking Mechanism

It might seem bold to link a unique property portfolio to a unique bonding mechanism, but chemical bonding is at its best if it is employed to explain material properties. Nevertheless, it would be highly desirable to obtain further support and confirmation for the notion that there is a novel bonding mechanism at work in solids besides ionic, metallic and covalent bonding, yet also different from the weaker hydrogen and van der Waals bonding. Indeed, such support is obtained by studies of various solids employing atom probe tomography (APT). This technique

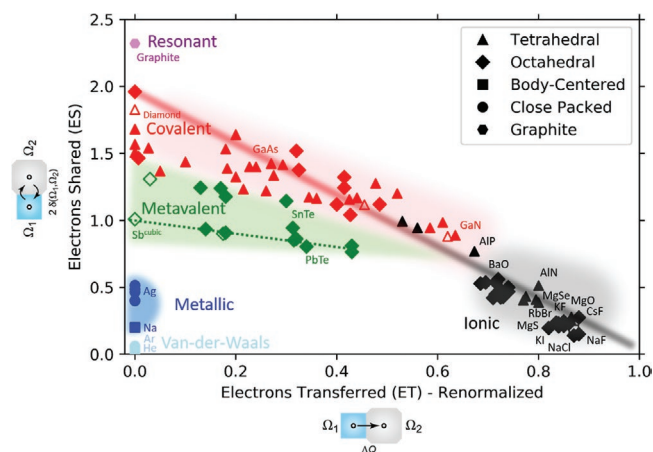


**Figure 2.** 2D map describing bonding in solids. The map is spanned by the renormalized electron transfer between adjacent atoms obtained after division by the formal oxidation state and the sharing of electrons between them. Triangles, diamonds, squares, and circles denote tetrahedrally bonded solids, distorted, and ideal rocksalt-type (octahedrally coordinated) structures, body-centered solids, and close-packed metals, respectively, while filled and open symbols represent thermodynamically stable and metastable phases. All ideal rocksalt structures for materials with half-filled p-bands are located on the green-dotted line, spanning from AgSbTe<sub>2</sub> to PbSe, while all distorted octahedrally coordinated structures are situated above it, characterized by a larger number of electrons shared.

is frequently employed to characterize the elemental distribution in solids on the nanoscale.<sup>[25,26]</sup> In atom probe tomography, a voltage is applied to a sharp tip of a specimen creating a high field strength at the apex of the tip (see Figure 3). In samples which are nonconducting, in addition, a short laser pulse is applied to dislodge atomic or molecular fragments from the surface. The mass of the ions created is derived from the flight-time of the ions, while their point of arrival at the 2D detector enables the determination of their point of origin in the tip. Hence, a 3D image of the sample with atomic resolution is created. Usually, low pulse powers are employed, where only a small fraction of all pulses leads to the rupture of bonds at the apex of the specimen and hence to the formation of ions, contrary to “nulls,” i.e., the majority of laser pulses which do not produce such ions. The percentage of pulses, which is successful in creating ions is called the “detection rate” in APT. In our case, detection rates between 0.5% and 2.5% have been chosen.

Generally, during an APT measurement, a successful laser pulse, i.e., one that manages to dislodge a fragment from the tip, most probably leads only to a single ion on the detector (single event), while only a small fraction of laser pulses leads to a release of several fragments and therefore to more than one ion arriving on the detector, which is called “multiple events.” A small but not-zero probability of multiple events is always observed during APT measurements.<sup>[28,29]</sup> Surprisingly, in crystalline phase change materials like GeTe or Ge<sub>2</sub>Sb<sub>2</sub>Te<sub>5</sub>, this is very different. If a laser pulse manages to dislodge fragments, in crystalline phase change materials typically more than 70% of the ions come as multiples. These different ions are not formed by fragmentation of one larger entity on the flight path to the detector. Instead the vast majority of multiples formed is created at the tip surface. This implies that the bond breaking in crystalline phase change materials is unique, as depicted in Figure 4. Upon laser-assisted field evaporation in crystalline GeSe, Si, or InSb, or metals such as Al, Fe, or W, on the contrary, only a small probability to form multiple fragments is observed. Hence, there is an astonishing difference in bond breaking between these different classes of materials. It is furthermore interesting to note that the bond breaking in amorphous and crystalline Si does not differ, indicating that in both cases a similar bonding mechanism is at work. For Ge<sub>2</sub>Sb<sub>2</sub>Te<sub>5</sub> on the contrary, the bond breaking is very different in the amorphous and the crystalline states. The most plausible explanation for this striking difference is a change of bonding mechanism upon crystallization of phase change materials such as Ge<sub>2</sub>Sb<sub>2</sub>Te<sub>5</sub>.

To conclude this section, in Figure 5, the 2D map (cf. Figure 2) is combined with the probability of multiple events. This map shows that an unconventional bond rupture, i.e., a high probability for multiple events, is observed for all those materials which employ MVB. This further supports the view that MVB is a fundamental, unconventional bonding mechanism.

### 2.4. A Comparison of Maps to Sort Materials and Bonding Mechanisms

Figure 2 now provides a map which appears very powerful. It separates the different bonding mechanisms (ionic, metal, and

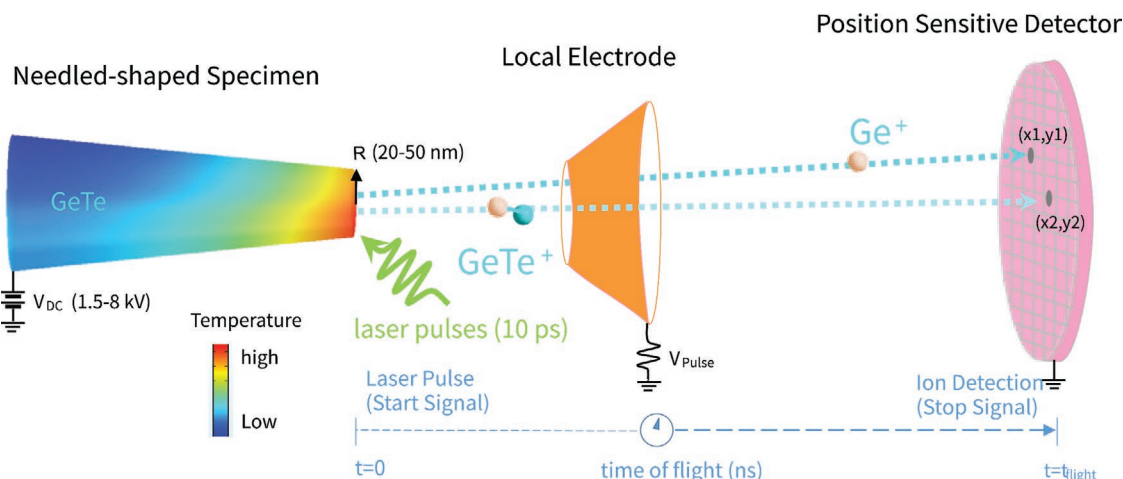


**Figure 3.** Schematic of the laser-assisted atom probe tomography. The needle-shaped specimen (left hand side) is subjected to a voltage of 1.5–8 kV and illuminated by 10 picosecond laser pulses, triggering the field evaporation of atoms or molecular fragments. These atoms or molecular fragments are ionized and successively projected on the position sensitive detector (right hand side). Reproduced with permission.<sup>[27]</sup> Copyright 2018, RWTH Aachen University. Published by Wiley-VCH.

covalent) and furthermore provides evidence for a new bonding mechanism. While this is the first map that claims the existence of MVB, maps such as the one shown in Figure 2 have a long

history in chemistry, since they help to sort and understand property trends. Hence, we have to ponder how this map compares with maps that have previously been suggested. The oldest map

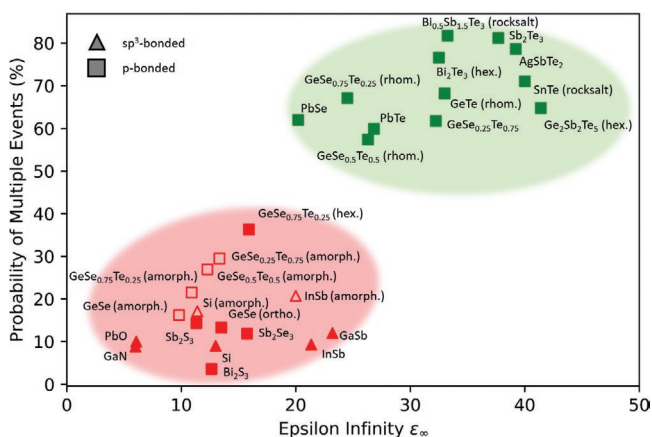


**Figure 4.** Correlation between the probability to produce multiple events and the optical dielectric constant  $\epsilon_{\infty}$ , an optical identifier of bonding mechanisms. A wide variety of materials are shown, which can be categorized into two classes considering their bonding mechanism. Covalently bonded materials are denoted in red, while compounds utilizing the characteristic features of crystalline PCMs are depicted in green. Open symbols characterize amorphous phases, filled symbols depict crystalline phases, while triangles describe tetrahedrally coordinated materials, squares denote p-bonded compounds (octahedral-like atomic coordination), amorph., rhomb. and ortho. denote amorphous, rhombohedral, and orthorhombic phases, respectively. Crystalline PCMs have much larger values of the optical dielectric constant ( $\epsilon_{\infty}$ ) than all other materials and can hence be found on the right side of the viewgraph. Interestingly, these materials also differ from all other materials in terms of laser-assisted field evaporation. Crystalline PCMs are characterized by a high number of multiple events, not observed in any other material class studied here. This provides strong evidence for a different bonding mechanism in crystalline PCMs, which is characterized by a higher “collectiveness” in bond rupture. Reproduced with permission.<sup>[27]</sup> Copyright 2018, RWTH Aachen University. Published by Wiley-VCH.

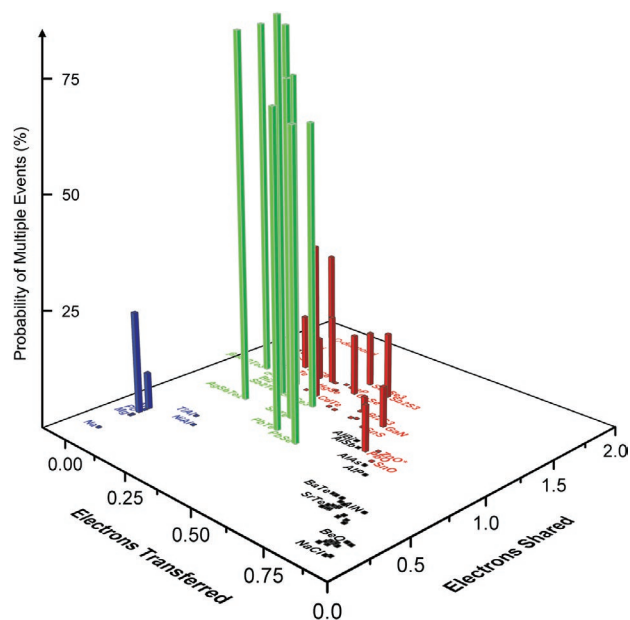


**Figure 5.** Correlation between the probability to produce multiple events and the bonding mechanism. A 3D map using the basal plane of electrons transferred (ET, i.e., renormalized by the oxidation state) and electrons shared showing the “probability of multiple events” (PME) measured by laser-assisted atom probe tomography. All compounds with a high probability of creating several fragments upon exposure to a single laser pulse are located in an area of the map, which is characterized by sharing about one electron between neighboring atoms. In this region, the probability of multiple events ranges from about 60% to more than 80%, while the highest value observed outside this region is about 33%. There is thus apparently a close correlation between the property portfolio of solids characterized by different colors, the bonding mechanism as described by the number of electrons transferred and shared and the bond breaking as measured by the atom probe. Reproduced with permission.<sup>[24]</sup> Copyright 2019, The Authors. Published by Wiley-VCH.

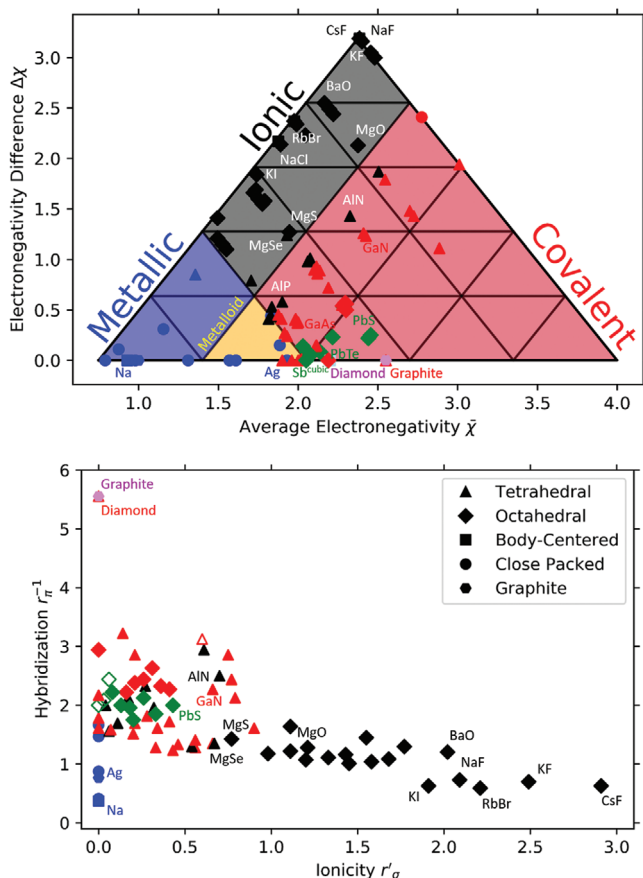


**Figure 6.** Comparison of different maps to identify bonding trends. Van Arkel/Ketelaar map (top), Littlewood map (bottom). The colors for each entry were determined by the material properties. The two maps, which employ different axes, show regions where materials cluster, which show predominantly metallic, ionic, or covalent bonding. However, these maps do not separate covalent compounds very well from metals or ionic compounds. Furthermore, these maps do not contain structure information, and can hence not distinguish different allotropes. Finally, compounds that employ multivalent bonding do not occupy a well-defined region and are not separated from the other bonding mechanisms, even though their properties and their bond breaking differ significantly.

that we are aware of was published in 1941 by van Arkel<sup>[12]</sup> and in 1947 modified by Ketelaar<sup>[13]</sup> (see Figure 6a). In it, they suggest using the average electronegativity as well as the difference in electronegativity as the two decisive parameters to span the map, which already separates ionic, metallic, and covalent bonding. Interesting enough, in the transition region between “the big three” a region with a different color is found, but it is not attributed to a particular bonding mechanism. Instead, it is referred to as the region of metalloids. Several decades later, similar maps became fashionable to explain property trends in solids. In these maps, the average electronegativity has often been replaced by the hybridization, a concept to describe the ease of mixing different orbitals, usually considering an estimate of the size of the *s*- and *p*-orbitals of the valence electrons (see Figure 6b). However, all of these maps are still based on empirical parameters characterizing atoms to derive their positions on the *x*- and *y*-axes. Hence, these maps lack structure information and two allotropes of one compound would occupy the same position in the map. Considering

a case like carbon, this shows that it would be impossible in such a map to distinguish graphite from diamond, even though both differ significantly in terms of bonding and properties. This weakness has been removed, by novel maps which include the atomic arrangement in DFT calculations and hence obtain a structure sensitive view on bonding,<sup>[30,31]</sup> yet still use ionicity (the difference in electronegativity) as well as hybridization as the map coordinates. Finally, advances in Quantum Chemical Topology sketched in Section 2.1 enable an unprecedented view on bonding in solids, leading to maps as presented in Figure 2. One can now compare the ability of these different maps to classify materials in terms of the bonding mechanism utilized as well as their ability to identify borders between bonding mechanisms. We have hence used the properties of different materials to assign them a bonding mechanism and plot them in different types of maps.

Both maps depicted in Figure 6 utilize the ionicity as one of the two parameters to distinguish different bonding mechanisms. However, this seems to be problematic, since the electron transfer in, e.g., alkali halides such as KF (0.86) and KI (0.82) is very similar, yet the difference in electronegativity varies significantly more (2.49 vs 1.91). Hence both quantities make different predictions concerning bonding. The ionicity difference implies that there is a substantial variation in bonding going from KF to KI. The map in Figure 2 instead implies that the ionic bonds in both materials are rather similar, due to the similar electron transfer. This raises the question which of the different coordinate systems (average electronegativity vs difference of electronegativity; ionicity vs hybridization or electrons transferred vs electrons shared) is better suited to separate different bonding mechanisms and to predict property trends. Visual inspection of the three maps implies that the map presented in Figure 2 separates the different bonding mechanisms best and has the clearest borders between bonding mechanisms. These advantages can be attributed to the fact that the algorithm to produce the map in Figure 2 includes the atomic arrangement in deriving its coordinates. Furthermore, it seems as if the number of electrons transferred (ET) and the number of electrons shared (ES) are the “natural” coordinates to describe bonding in solids. Hence, these coordinates are advantageous, if we try to reach our key goal, the identification of property trends and superior advanced functional materials, as will be shown in Section 2.7.

## 2.5. From Multivalent Bonding via Crystal and Band Structure to the Unique Property Portfolio of Incipient Metals

In the preceding sections it has been argued that MVB constitutes a unique bonding mechanism characterized by an unconventional property portfolio and a remarkable bond rupture upon laser-assisted field evaporation. Furthermore, it was shown that multivalently bonded materials are located in a well-defined region of the ES–ET map. They share about one electron between adjacent neighbors and are characterized by small or moderate electron transfer. In this section, we will turn the argument around and will demonstrate that the properties described in Section 2.2 as a unique fingerprint of multivalently bonded materials result from their unique position in the map depicted in Figure 2, which is closely related to the materials’



“orbital scheme,” i.e., the orbitals utilized to form bonds between adjacent atoms.

Interestingly, the crystalline compounds depicted in the green region of the map (see Figure 2) share a common motif as far as the atomic arrangement is concerned. They are characterized by an octahedral-like atomic arrangement. Many compounds possess a rocksalt structure, i.e., a perfect octahedral arrangement, where the atoms are surrounded by 6 nearest neighbors. Such an arrangement is frequently found in ionic compounds. Yet, materials such as PbTe or PbSe possess a metallic luster and moderate electrical conductivity, incompatible with ionic bonding. Other materials like GeTe or Bi<sub>2</sub>Se<sub>3</sub> can be described by a distorted octahedral arrangement. These different atomic arrangements are depicted in Figure 7a. The similarity of atomic arrangements indicates that the structures are a consequence of close similarities in chemical bonding. The bonding mechanism utilized can be best depicted when looking at the simplest possible materials showing MVB, elemental Sb or Bi. Both elements display a rhombohedral structure, i.e., an octahedral-like atomic arrangement. This atomic arrangement can be described as a simple cubic structure with small distortions. In Figure 7a, such a hypothetical cubic structure of Sb is displayed, which reveals the octahedral atomic arrangement of Sb atoms. Sb and Bi have 5 valence electrons, i.e., 2 s- and 3 p- electrons in their outermost shell. However, the s- and p- electrons are too far apart in energy, so that they hardly hybridize. Hence, the p-electrons

alone are responsible for bonding. With 3 p-electrons per atom and 6 nearest neighbors, for a pair of neighboring atoms only ½ p-electron per atom is available to form a bond. Hence, each pair of atoms is held together by just a single p-electron (Figure 7b).

In the language of band structure, this corresponds to a half-filled p-band. One would hence expect metallic behavior. This is depicted in Figure 7d. Instead, however, compounds like GeTe, PbTe, or Bi<sub>2</sub>Se<sub>3</sub> are narrow gap semiconductors. There are two different mechanisms at play which lead to an opening of the bandgap. The first is related to distortions of the simple cubic (for elements) or rocksalt structure (for compounds). This distortion, which is frequently denoted as a Peierls distortion,<sup>[33]</sup> opens a band gap, as depicted in Figure 7c,d. Many, but not all of the p-bonded systems in Figure 2 reveal such a Peierls distortion, which can be quantified for octahedral-like systems by  $r_{PD} = r_1/r_s$ , where  $r_s$  is the average distance to the first (three) neighboring atoms, while  $r_1$  represents the average distance to the next (three) adjacent atoms. However, there is a second mechanism, which these p-bonded systems utilize to open a bandgap. This is charge transfer between adjacent (dissimilar) atoms as displayed in Figure 7c, too.

As discussed above, the ideal case of MVB corresponds to a perfect octahedral arrangement without any charge transfer between atoms. This configuration is characterized by the sharing of one electron between adjacent neighbors (ES = 1) and no electron transfer (ET = 0). This MVB reference point

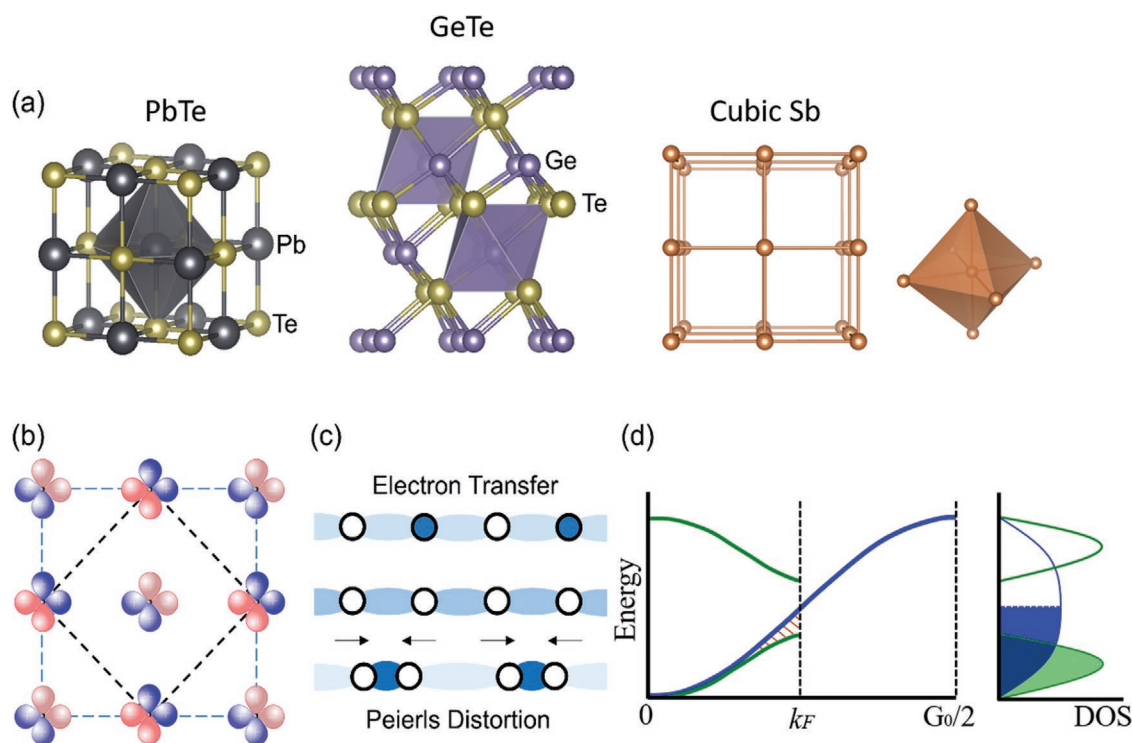


**Figure 7.** a) Octahedral-like coordination in PbTe, GeTe, and hypothetical cubic Sb. b) Schematic diagram of the (001) plane of PbTe, displaying the  $\sigma$ -bonds formed from p-orbitals, which are responsible for the octahedral-like atomic arrangement. c) The middle sketch shows the symmetric atomic arrangement without charge transfer (as encountered in cubic Sb). The distribution of electrons is either modified by a Peierls distortion (bottom), denoted by arrows or by electron transfer (top). d) Density of states for the symmetric case (blue) and a situation with a Peierls distortion or alternatively charge transfer between the atoms leading to bandgap opening (green curve). Adapted with permission.<sup>[24]</sup> Copyright 2019, The Authors. Published by Wiley-VCH.

describes cubic Sb and Bi, as displayed in Figure 2. We can now plot the size of the Peierls distortion as a function of ES and ET. This is shown in Figure 8. In Figure 8a, the size of the Peierls distortion is depicted for the p-bonded systems with octahedral-like atomic arrangement. One can see that the distortion vanishes (open circles) for all solids on the dashed line. The further we move up and away from the dashed line, the more the size of the Peierls distortion increases. Hence, we can describe systematic trends regarding a change in atomic arrangement with the two quantities, which describe trends in chemical bonding (ES, ET). While the size of the Peierls distortion increases with the distance from the dashed green line, a clear dichotomy of values is observed (Figure 8b). While metavalently bonded systems are characterized by a range of  $r_{PD}$  values between 1 and about 1.1, covalently bonded systems are characterized by  $r_{PD}$  values above 1.2. This is an interesting finding, since there is no a priori reason, while the range of  $r_{PD}$  values between about 1.1 and 1.2 should not be occupied. This implies that the transition from MVB to covalent bonding upon increasing Peierls distortion is possibly discontinuous. Such a potential discontinuity would provide further support to the notion that the MVB is a unique and fundamental bonding mechanism. Still, it has to be kept in mind that the relevant coordinate system to depict systematic property trends, including those for the Peierls distortion is 2D. One hence has to explore trends for the Peierls distortion as a function of electrons shared and transferred, as depicted in Figure 8.

At the beginning of this section, it has been argued that a half-filled p-band should lead to metallic behavior. However, Peierls distortions and charge transfer lead to the formation of a small bandgap as illustrated in Figure 7c,d. Hence, one can expect a moderate electrical conductivity even for undoped compounds at room temperature. Figure 9 displays the room temperature electrical conductivity in a 3D map as a function of the number of electrons transferred and shared. Again, systematic trends are visible for the metavalently bonded systems. They show room temperature electrical conductivities between ( $10^1$  S cm<sup>-1</sup> and  $10^4$  S cm<sup>-1</sup>), i.e., fall within a narrow range in close proximity to good metals ( $\sigma > 10^5$  S cm<sup>-1</sup>). They therefore live up to their name as “incipient metals.” Furthermore, the electrical conductivities show a systematic trend with increasing Peierls distortion, i.e., increasing vertical distance away from the dashed green line for the cubic systems. Yet, the electrical conductivity also

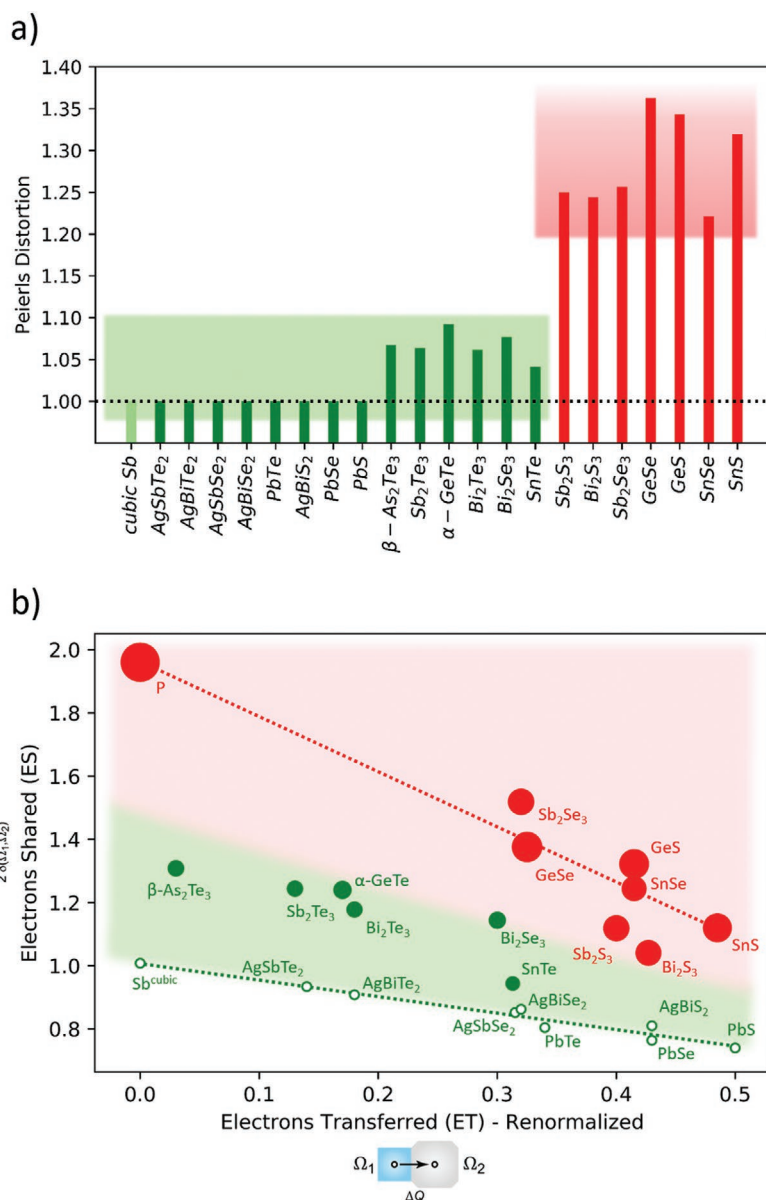


**Figure 8.** Variation of the size of the Peierls distortion. a) Size of the Peierls distortion for various p-bonded systems. Interestingly, the size of the Peierls distortion falls into two well-defined ranges; values of  $r_{PD}$  between 1 and about 1.1 characterize the metavalently bonded systems, while the covalently bonded systems have  $r_{PD}$  values above 1.2. Hypothetic cubic Sb is depicted as a light green bar. b) Size of the Peierls distortion upon variation of the number of electrons shared between adjacent atoms and the renormalized electron transfer. The size of the circles characterizes the size of the Peierls distortion. Open circles denote cubic systems and thus a vanishing Peierls distortion, i.e.,  $r_{PD} = 1.0$ . All these cubic systems are located on the dashed line. p-bonded systems with an average of 3 p-electrons per atom, i.e., a half filled p-band that are located further away from this dashed line reveal an increasing Peierls distortion.

decreases with increasing electron transfer for the cubic systems along the same line. Hence, for metavalently bonded systems increasing both ES or ET leads to a decrease of electrical conductivity. This conclusion provides a new perspective on the bonding in these incipient metals and enables tailoring an important property for applications, the electrical conductivity of the crystalline state. Apparently, these unconventional materials possess valence electrons, which are neither fully

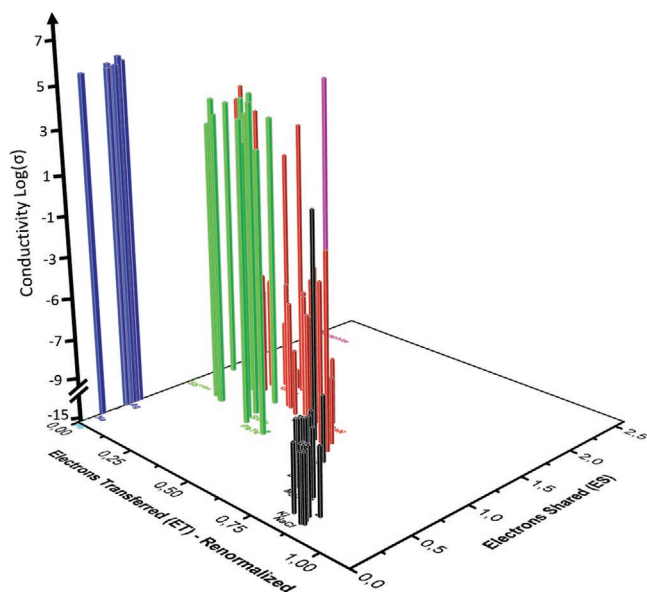


**Figure 9.** Correlation between the electrical conductivity of solids and their bonding mechanism. A 3D map using the basal plane of electrons transferred (ET, i.e., renormalized by the oxidation state) and electrons shared showing the electrical conductivity of solids without extrinsic doping at room temperature. All compounds that utilize multivalent bonding possess a conductivity between  $10^1$  and  $10^4$   $\text{S cm}^{-1}$ , which approaches the typical range of metals (around  $10^5$   $\text{S cm}^{-1}$ ). With increasing Peierls distortion, which is also reflected in an increase of the number of electrons shared between adjacent atoms, the electrical conductivity decreases for multivalently bonded solids. Ionic and most covalent compounds have a much lower electrical conductivity. Only a few covalently bonded semiconductors with narrow bandgap like InSb also reveal a high electrical conductivity at room temperature. Reproduced with permission.<sup>[24]</sup> Copyright 2019, The Authors. Published by Wiley-VCH.

localized as observed in ionic or covalent compounds, nor fully delocalized as in metals. Instead, their bonding mechanism is characterized by a competition between electron delocalization (metallic bonding) and electron localization (ionic or covalent bonding). Interestingly, this competition, which characterizes multivalently bonded solids, leads to a unique portfolio of properties that can be tailored.

Figure 10 shows three additional fingerprints of multivalently bonded solids, large values of the Born effective charge  $Z^*$ , high values of the optical dielectric constant  $\epsilon_\infty$  as well as large Grüneisen parameters for the transverse optical modes  $\gamma_{\text{TO}}$ , a measure of anharmonicity. Clear dependencies on chemical bonding are observed for all three properties ( $Z^*$ ,  $\epsilon_\infty$ , and  $\gamma_{\text{TO}}$ ). The chemical bond polarizability, which is characterized by the Born effective charge  $Z^*$ , is very high for those p-bonded materials (marked by green diamonds), which employ MVB.  $Z^*$  notably decreases upon increasing size of the Peierls distortion, and the concomitant increase of the number of electrons shared between neighboring atoms (ES). In contrast, the chemical bond polarizability ( $Z^*$ ) appears less affected by increasing electron transfer (ET). Upon approaching the border to ionic bonding  $Z^*$  apparently remains still rather large. This is interesting, since it implies that different properties change differently when approaching different borders, a finding that

is indicative of a significant potential to tailor the properties of multivalently bonded materials.

It should also be noted that high values of the Born effective charge  $Z^*$  are also observed for ferroelectric oxides, which do not employ MVB. For these oxides, the high value of  $Z^*$  is indicative of a structural instability, which is also frequently accompanied by soft modes, in particular transverse optical modes with particularly low frequency. Nevertheless, ferroelectric oxides and multivalently bonded materials also show very pronounced differences in material properties and hence do not employ the same bonding mechanism. This can be seen, for example, when looking at the optical dielectric constant  $\epsilon_\infty$ , a measure of the electronic polarizability. This quantity is very high for multivalently bonded materials, as displayed in Figure 10b. The large values observed are indicative of an electronic instability, which has been already sketched in Figure 7. Ferroelectric oxides, on the contrary do not possess high values of  $\epsilon_\infty$ . While they are characterized by a structural instability, they lack an electronic instability. Multivalently bonded materials, on the contrary, possess an electronic instability, which is accompanied by a concomitant structural instability.

Finally, in Figure 10c, the Grüneisen parameter for the transverse optical modes is depicted. The Grüneisen parameter describes the logarithmic derivative of the frequency of transverse optical phonons with respect to volume. This quantity is a measure of the anharmonicity of the solid. For acoustic modes in normal solids values between 1 and 2 are usually found. For multivalently bonded materials, instead, much higher values are observed. Again, these values decrease with increasing Peierls distortion and the associated increase of the number of electrons shared between adjacent atoms.

Summarizing the main message of this section, we can explain the unique property portfolio of incipient metals based upon the half-filled p-bands leading to  $\sigma$ -bonds between adjacent atoms. The related electronic instabilities (localization vs delocalization) lead to charge transfer and distortions. This provides the opportunity to tailor the unique property portfolio compiled in Table 1.

To evaluate the ability to separate materials utilizing different bonding mechanisms and to visualize the predictive power of the various maps introduced in chapter 2, an interactive representation of the bonding maps was created. This interactive tool,<sup>[34]</sup> which is briefly described in the supplement can be accessed at materials-map.rwth-aachen.de.

## 2.6. Distinguishing Multivalent Bonding from Resonant Bonding

In the past, many scientists (including us) have denoted the bonding mechanism of crystalline phase change materials as resonant bonding. The concept of resonant bonding has been employed to explain the property contrast between the amorphous and crystalline phase of these compounds,<sup>[35,36]</sup> the low thermal conductivity of GeTe and PbTe<sup>[37]</sup> as well as a number of other interesting properties. Thus, the concept of resonant bonding in chalcogenides has been widely accepted by the community. Hence, we should pause for a moment to check if a change of the bonding name is really mandatory. Interestingly, we are not suggesting this name change since any of the

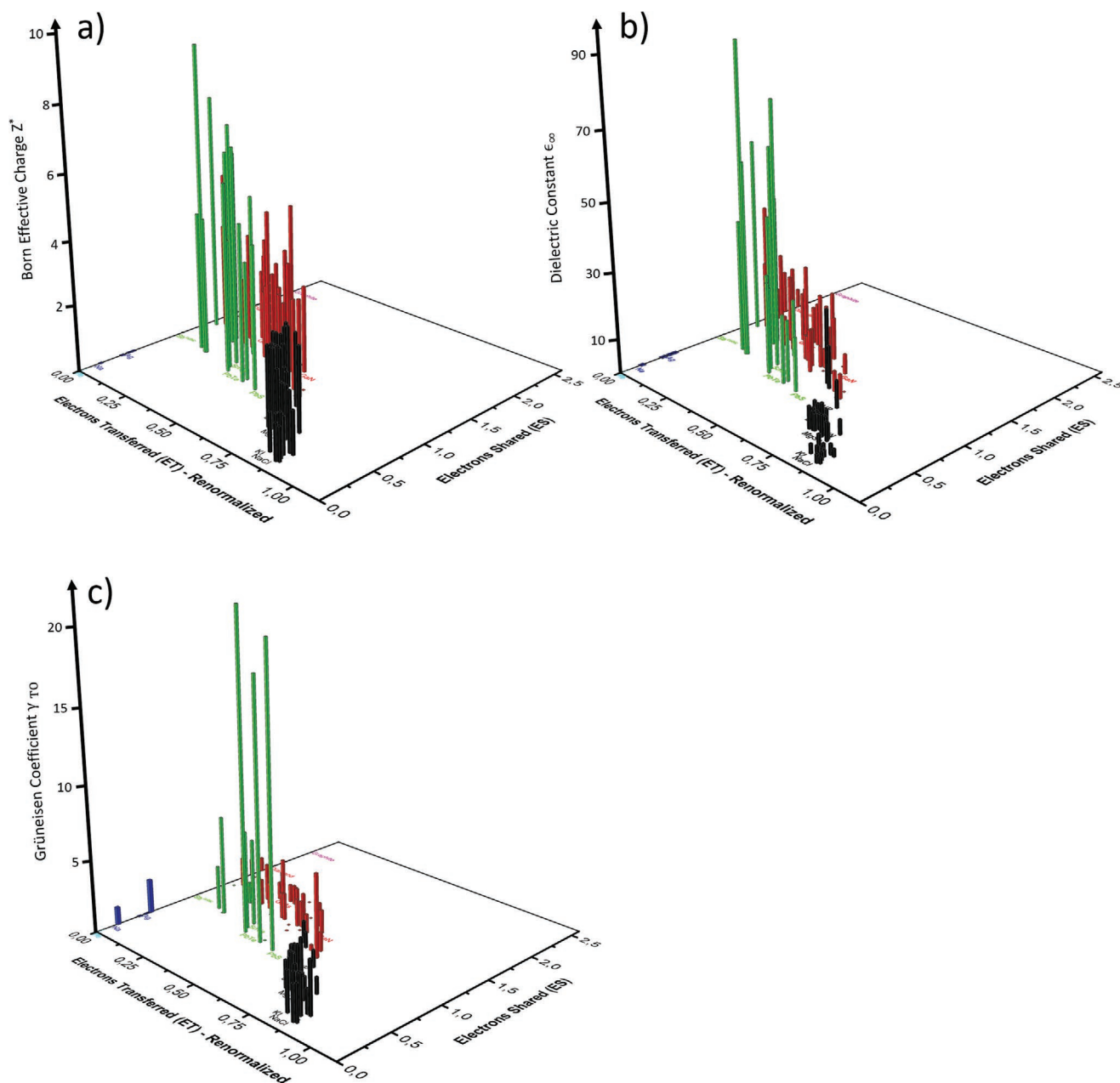


**Figure 10.** Correlation between different characteristic material properties and the related bonding mechanism. A 3D map using the basal plane of electrons transferred (ET, i.e., renormalized by the oxidation state) and electrons shared showing the a) chemical bond polarizability as characterized by the Born effective charge. b) Electronic polarizability which can be described by the optical dielectric constant  $\epsilon_{\infty}$ . Finally, in c), the Grüneisen parameter for transverse optical modes  $\gamma_{TO}$  is depicted, providing a measure of the lattice anharmonicity. Systematic trends are observed for all three properties within the region where metavalently bonded systems are found. Increasing electron transfer, as well as pronounced electron sharing lead to a strong decrease of  $Z^*$  and the optical dielectric constant  $\epsilon_{\infty}$ . Adapted with permission.<sup>[24]</sup> Copyright 2019, The Authors. Published by Wiley-VCH.

previous measurements or calculations were wrong. There is no controversy regarding the unconventional properties of crystalline phase change materials such as GeTe, Sb<sub>2</sub>Te<sub>3</sub>, or Ge<sub>2</sub>Sb<sub>2</sub>Te<sub>5</sub>. These compounds are characterized by large values of  $Z^*$  and  $\epsilon_{\infty}$ , as well as high values of the Grüneisen parameter for transverse optical modes  $\gamma_{TO}$  and an effective coordination number (ECoN) incompatible with ordinary covalent bonding. Finally, they possess an electrical conductivity in the

crystalline phase, which is neither typical for metals nor for covalently bonded semiconductors. Are these unconventional properties sufficient to denote the bonding in these materials as resonant bonding? This seems justified if we can prove that materials like benzene or graphite, where the concept of resonant bonding has stronger historical roots explaining atomic arrangement and material characteristics, have properties which closely resemble those of GeTe, Sb<sub>2</sub>Te<sub>3</sub>, or PbTe.

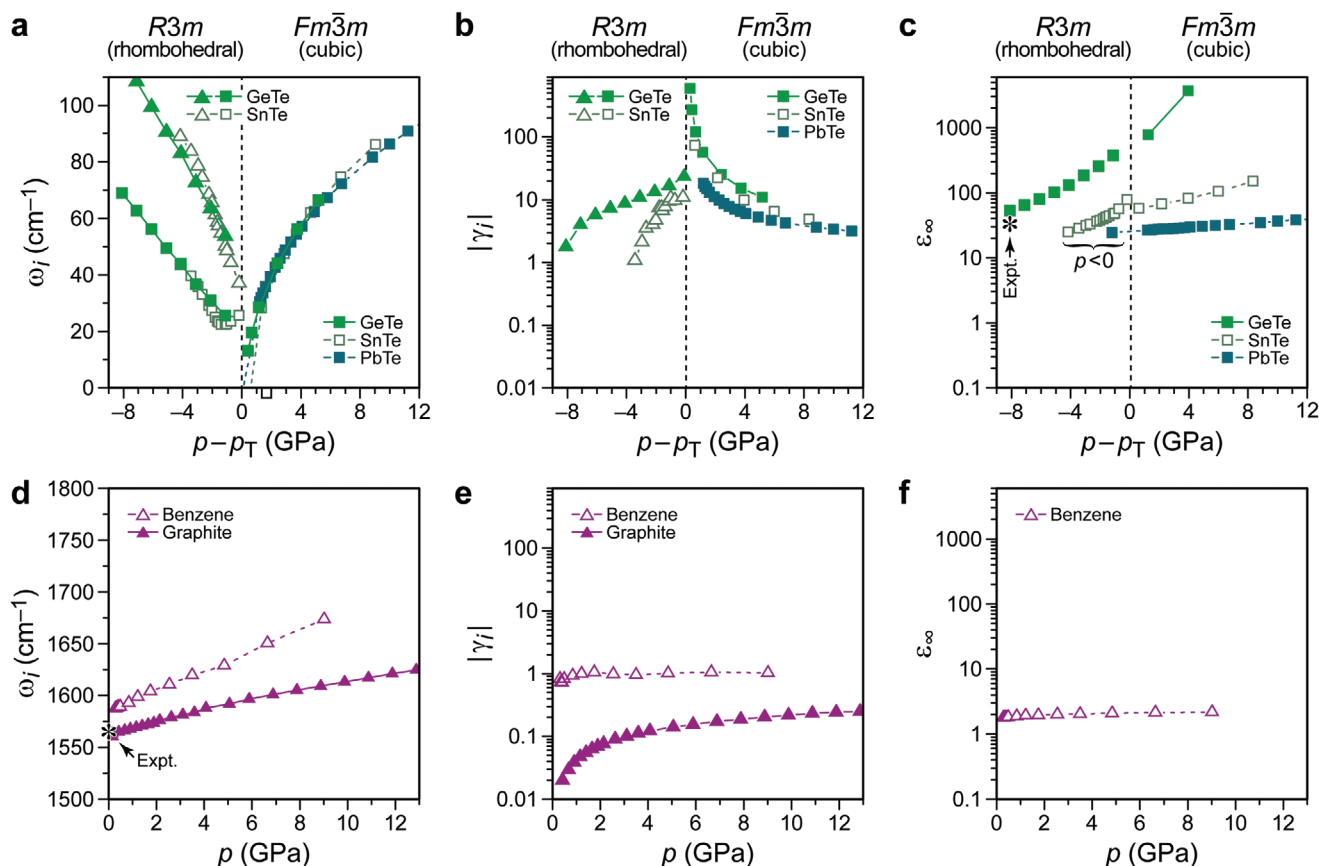


**Figure 11.** Physical properties of different materials previously called “resonantly bonded.” a) Phonon frequencies,  $\omega_i$ , for transverse optical modes in GeTe, SnTe, and PbTe as a function of pressure. Since GeTe and SnTe transform from a rhombohedral to a cubic structure, the respective transition pressure is set as reference ( $p_T = 8.1$  GPa for GeTe, 0.7 GPa for SnTe). b) Absolute Grüneisen parameters,  $|\gamma_i|$ , for transverse optical modes, as an indicator for an anharmonic lattice instability. c) Optical dielectric constants,  $\epsilon_\infty$ , as an indicator for the electronic susceptibility. d–f) Same for the textbook examples of Pauling-like resonant bonding in molecules (benzene) and solids (graphite), respectively. No anharmonic behavior and no unusually high values of  $\epsilon_\infty$  are observed. Where available, experimental data are included to ascertain the suitability of the computational method (asterisks); these data are taken from refs. [35] and [38] panel d), respectively. The remarkable differences between the upper and lower panels suggest that the bonding nature in both materials classes must be fundamentally different, and that therefore the use of the term “resonant bonding” in PCMs needs to be abandoned. Reproduced with permission.<sup>[23]</sup> Copyright 2018, RWTH Aachen University. Published by Wiley-VCH.

However, this is not the case as we can see in **Figure 11**, where several different properties of GeTe, SnTe, and PbTe are compared with benzene and graphite.

In **Figure 11a**, the dependence of the frequency of optical phonons,  $\omega_i$  on external pressure is depicted for GeTe, SnTe, and PbTe. In all of them,  $\omega_i$  changes strongly with external pressure, leading to very large absolute Grüneisen parameters  $|\gamma_i|$ . The results in **Figure 11b** not only reveal that the interaction potential for GeTe, SnTe, and PbTe is very anharmonic, but they explain why these materials have such a low thermal conductivity.<sup>[24,37]</sup> Large values of  $\gamma_i$  lead to low thermal conductivities of the lattice. As a consequence of this anharmonicity, incipient metals (in particular, PbTe and its chemical derivatives) are promising candidates for thermoelectrics.<sup>[15,24]</sup> Furthermore, the structural transition is linked to an electronic instability, reflected in an anomalous increase in the optical dielectric constant (**Figure 11c**). Such a link between structural and electronic anomalies is by far not universally present. For example, ionic ferroelectrics such as noncentrosymmetric

oxides show unique structural but not electronic instabilities near the phase transition.

For direct comparison, the same quantities for the textbook cases of<sup>[39]</sup> “resonance,” namely, benzene and graphite (**Figure 11d–f**) are displayed, too. No similar effect and no anomalous behavior are observed in these materials: the bonding is stiff (reflected in large vibrational frequencies that change only slowly with pressure), presumably due to the rigid  $sp^2$  backbone, and the optical polarizability is lower by orders of magnitude than in incipient metals (note the logarithmic axes in **Figure 11e,f**). Since the physical properties, as determined by the bonding, are quantitatively and qualitatively different between “resonantly” bonded materials and the above-mentioned chalcogenides, one should abandon calling the chalcogenides “resonantly bonded.”

There is further evidence that the underlying fundamental bonding mechanism must be different. Studying bond rupture in carbon nanotubes, which can be considered as rolled-up graphene sheets, reveals a conventional bond breaking, i.e., a low probability to form multiple events,<sup>[40]</sup> in striking contrast to

the bond rupture observed for crystalline phase change materials. This pronounced difference in bond breaking provides further evidence for the fundamental difference in bonding between resonantly bonded graphene and metavalently bonded chalcogenides. Finally, in Figure 2, graphite ( $ET = 0$ ,  $ES = 2.32$ ) is positioned in a very different region from the metavalently bonded materials, which are located in the region of  $ES$  around 1.0 and small values of  $ET$ . While the lack of charge transfer between the atoms in graphite is to be expected for an elemental solid, the large value of  $ES$  (2.32) is due to two different bonds between adjacent carbon atoms, a  $\sigma$ -bond coming from the  $sp^2$  orbitals of neighboring atoms, and a  $\pi$ -bond stemming from the  $p_z$ -orbital of those atoms. Hence, the properties of benzene, graphite, and graphene are dominated by these two bonds, one providing the covalent backbone ( $\sigma$ -bond) and the other one the states at the Fermi-level ( $\pi$ -bond). In contrast, in GeTe there is only a  $\sigma$ -bond, which comes from the half-filled p-band. As discussed in the previous section (2.5), this electronic configuration is unstable with respect to charge transfer and Peierl's distortions. Hence, we can summarize that there is compelling evidence that resonant bonding as in graphene, graphite, and benzene is fundamentally different from the bonding mechanism in GeTe, PbTe,  $Sb_2Te_3$ , and  $AgSbTe_2$ . This has led to the suggestion to call these chalcogenides and related compounds incipient metals and their bonding mechanism metavalent bonding.

In the outlook, we will describe the conceptional advantages of separating metavalent bonding from resonant bonding and will sketch a plethora of exciting questions for research which are a direct consequence of the emergence of a new, fundamental, bonding mechanism.

## 2.7. From Metavalent Bonding to Applications

In Section 2.5, it was shown how the unique property portfolio of incipient metals can be explained by very few assumptions about the mechanism underlying MVB. In Section 2.4, it was shown that all metavalently bonded materials are found in a rather well-defined region of the map depicted in Figure 2. However, the true value of a map does not only come from its ability to distinguish different regions (here bonding mechanisms), it also stems from its potential to predict. We will focus on this aspect in the following, which is relevant for applications. So far, property trends were displayed for five different quantities ( $\sigma$ ,  $Z^*$ ,  $\epsilon_\infty$ ,  $\gamma_{TO}$ , and  $E_{CoN}$  (or size of the Peierls distortion, respectively)) in Figures 8, 9, and 10, where clear tendencies were observed upon changing  $ES$  and  $ET$ . These changes could be related to systematic bonding changes. Hence, we now have a tool at hand to tailor properties. This is particularly promising, if advanced functional materials are to be designed, where the search for the best possible materials is a difficult task. Thermoelectric devices provide an interesting example. Such devices critically depend on the performance of the thermoelectric material used. The quality of a thermoelectric solid is defined by a single parameter, the figure of merit  $zT$ , which is

$$zT = S^2 \sigma T / (\kappa_e + \kappa_l) \quad (1)$$

where  $S$  and  $\sigma$  are the Seebeck coefficient and electrical conductivity and their product  $S^2 \sigma$  is called power factor;  $T$ ,  $\kappa_e$ , and  $\kappa_l$  are the absolute temperature, the electronic thermal conductivity, and the lattice thermal conductivity, respectively.<sup>[41]</sup>

Hence, the task to tailor thermoelectrics appears simple at first, "it is just optimizing a single quantity,  $zT$ ." Nevertheless, as pointed out by Singh,<sup>[42]</sup> this is like finding a needle in a haystack, since closer inspection of  $zT$  reveals, that we are looking for solids which are as conductive for charge as metals, which possess a high Seebeck coefficient, like typical semiconductors, and are poor thermal conductors, such as glasses. Clearly, this sounds like a set of contradicting requirements. Indeed, sophisticated concepts have been devised to solve this challenge, including optimum doping,<sup>[43]</sup> electron crystal—phonon glass concepts,<sup>[44]</sup> nanostructuring and the like.<sup>[45–48]</sup> Yet, we can also wonder, which potential a map such as the one shown in Figure 2 possesses. Notably, in the region between metallic and covalent bonding, a number of materials are found, which are known to be good thermoelectrics, including PbTe, PbSe,  $Bi_2Te_3$ , and GeTe based alloys. This implies that there should be a link between the application potential of these materials as thermoelectrics and the bonding mechanism they utilize. Indeed, we can now plot the relevant figure of merit as the third dimension of the map. In Figure 12, data are depicted showing the  $zT$  value of different intrinsic materials (prior to doping with foreign elements) for more than 50 compounds adopting different bonding mechanisms. These data reveal that materials which employ MVB possess particularly high values of  $zT$ . One could now search for clear property trends in this 3D map to identify suitable materials, which might even lead to the identification of compounds with higher values of  $zT$ . Clearly,

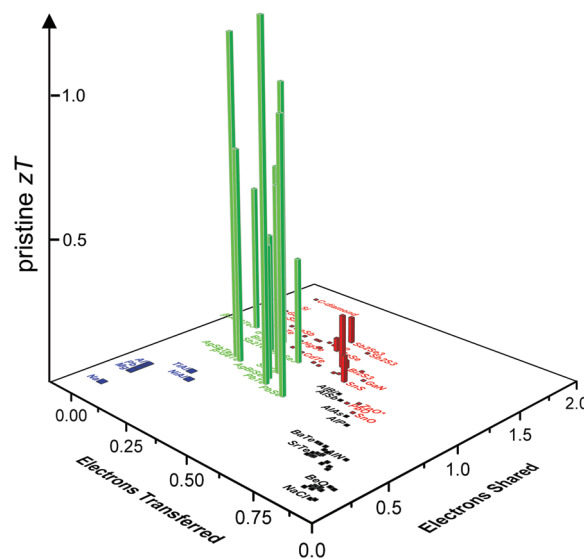


**Figure 12.** Correlation between the thermoelectric figure of merit  $zT$  and the bonding mechanism. A 3D map using the basal plane of electrons transferred ( $ET$ , i.e., renormalized by the oxidation state) and electrons shared showing the figure of merit  $zT$  of different intrinsic materials, prior to doping with foreign elements. All compounds with a high  $zT$  value in this map are characterized by metavalent bonding. Reproduced with permission.<sup>[24]</sup> Copyright 2019, The Authors. Published by Wiley-VCH.

the density of the data points is not yet sufficient to derive clear trends for  $zT$ . However, this is just a matter of time, before such higher data densities become available. Alternatively, experiments can be designed to search for such trends. For example, one could start with a given compound, say  $PbTe$ , and alloy it with say  $Sb_2Te_3$ . The map suggests such systematic studies of stoichiometry trends and provides a framework to discuss property trends in terms of the number of electrons shared and transferred.

However, there is a second option how to progress. One can also explore how other physical properties change with stoichiometry within a 3D map. This approach potentially provides a framework, to *explain and understand trends*. In Figures 9 and 10, four different quantities are depicted, namely the electrical conductivity  $\sigma$ , the Born effective charge  $Z^*$ , the optical dielectric constant  $\epsilon_\infty$  and the Grüneisen parameter (for transverse optical modes)  $\gamma_{TO}$ , which are potentially linked to the thermoelectric performance of the corresponding solids. One can now explore which of the quantities seems most closely related to  $zT$ . Clearly, for the quantities depicted in Figures 9 and 10, the Grüneisen parameter  $\gamma_{TO}$  and the electrical conductivity  $\sigma$  show a pronounced correlation to  $zT$ . This is not surprising, since high Grüneisen parameters should lead to low thermal conductivities, in line with experimental data for different chalcogenides,<sup>[49]</sup> as well as DFT calculations, which relate the low thermal conductivity to the unique bonding mechanism.<sup>[37]</sup> Yet, Figure 10 also shows systematic changes for the electrical conductivity upon changes in bonding. As clearly visible in Figure 10, the electrical conductivity should not be too small. This can be realized for metavalently bonded materials, if both the local distortions and the charge transfer are not too large.

Finally, high values of  $zT$  also require high Seebeck coefficients. Recently, it has been shown how large Seebeck coefficients can be combined with high electrical conductivities in materials which employ MVB.<sup>[50]</sup> This enabled the realization of power factors as large as  $8 \times 10^{-4} \text{ W m}^{-1} \text{ K}^{-1}$  at room temperature. Interestingly, upon the transition to ordinary covalent bonding, the power factor instantaneously is dropping by a factor of 8, providing further evidence for the intimate relationship between bonding mechanism and resulting material properties.

Many of the materials in Figure 2 such as  $GeTe$  and  $Sb_2Te_3$  are also well-known phase change materials. It is thus tempting to use the map in Figure 2 to optimize phase change materials. However, this task is facing several challenges. First of all, the term “phase change material” is ill-defined. There are phase change materials for optical and electrical data storage, those for reconfigurable photonic applications and even those for energy storage, which consist of an entirely different material class altogether. Furthermore, there is no single figure of merit that can be utilized to optimize phase change materials, in contrast with the situation encountered for thermoelectrics. This can be seen when comparing the different usages of phase change materials for data storage. In rewriteable optical data storage, for example, the optical contrast between the two different phases plays a prominent role, while in nonvolatile electronic memories a huge difference in the electrical conductivity of both phases is highly desirable. Further application-specific

requirements exist. For automotive applications elevated operation temperatures might be encountered, creating tightened requirements for the stability of the amorphous phase at these temperatures. On the other hand, fast switching speeds and cyclability are crucial for DRAM-like storage, as encountered in storage class memories.<sup>[51]</sup> Hence, the optimization of phase change materials for data storage depends significantly on the specific mode of application. Still, from the data and discussions presented here, a few conclusions can be drawn. To do so, we will focus on optical properties first. The word “phase change material” in this context refers to the fact that these materials can be stabilized in two different phases with different optical properties. It is advantageous to distinguish a phase change, which is temperature controlled as in  $VO_2$ , where around 340 K a transition from a semiconducting to a metallic state occurs,<sup>[52]</sup> from a transition between two different states which is controlled by transformation kinetics as is  $GeTe$ . In  $VO_2$  and other similar materials, it is not possible to stabilize the material in two different states at the same temperature. Hence, nonvolatile memory applications are impossible, however, smart windows and other advanced functionalities can be realized. To separate these two material classes, the term phase-transition material has recently been employed for  $VO_2$  and related materials.<sup>[53]</sup> In a phase change material like  $GeTe$ , it is possible to stabilize the material in two different phases at the same temperature, i.e., room temperature, to store data or realize a switch. For this application, the two phases need to have different optical properties. Such a difference in optical properties can have different origins. The Clausius-Mosotti equation shows that optical properties of a solid like the refractive index depend upon its density. Hence, a change in density, without a concomitant change in the electronic polarizability already produces a change of the refractive index. Usually such density changes in solids are quite modest. Amorphous Si, for example, is just 1.8% less dense than crystalline Si and hence only has a marginally lower refractive index. For  $Sb_2S_3$ , on the contrary, the density increases by 35% upon crystallization, leading to a significant change of the refractive index and the bandgap.<sup>[54]</sup> A pronounced density change also occurs for  $GeSe$ , where crystallization is accompanied by an increase in density of 5%, again leading to a discernible optical contrast between both phases.<sup>[55]</sup> For typical phase change materials like  $GeTe$ ,  $Sb_2Te_3$ , and  $Ge_2Sb_2Te_5$ , there is also a modest density change of 5%–10% between the amorphous and crystalline phase,<sup>[56]</sup> leading to a concomitant change in the joint density of states. However, a much larger contribution to the optical contrast comes from the change in the matrix element for the optical transition.<sup>[57]</sup> This is due to the much better alignment of the p-orbitals in the metavalently bonded crystalline state, compared to the amorphous state<sup>[36]</sup> which is characterized by higher levels of the Peierls distortion. In such a phase change memory, we are thus switching a compound between its metavalent crystalline and amorphous covalent state. Hence the optical contrast in phase change materials like  $GeTe$  or  $Ge_2Sb_2Te_5$  does not require a major density change upon crystallization, which is accompanied by mechanical stresses endangering the cyclability of the switching process.<sup>[58]</sup>

For photonic applications, at least a set of parameters has been identified that is crucial for successful applications. These

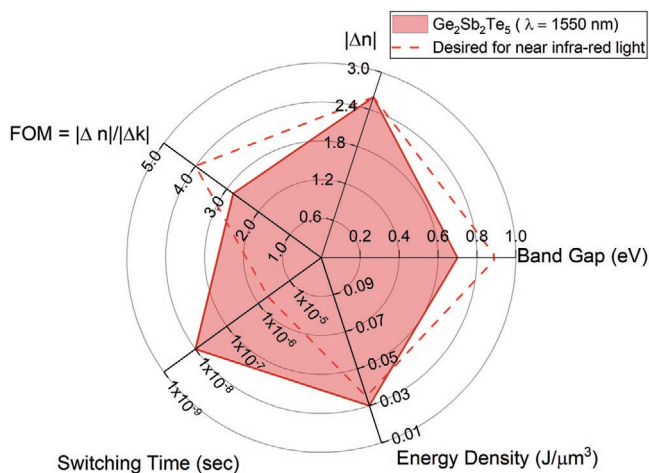


**Figure 13.** Set of requirements for a material to realize active photonic switches working at a near-infrared wavelength of 1550 nm. The red dashed line shows the set of desired properties, while the solid lines marks the properties offered by  $\text{Ge}_2\text{Sb}_2\text{Te}_5$ .

parameters are depicted in **Figure 13**. One can now use maps as shown in Figure 13 to search for tailored materials for reconfigurable photonic applications at a given laser wavelength. We are not aware of such systematic studies so far. The same holds for applications of phase change materials in nonvolatile electronic memories. Again, it seems rewarding to exploit the potential of maps such as the one depicted in Figure 2 to identify property trends and search for materials with tailored properties.

Finally, we would like to comment on another recent application area of incipient metals like  $\text{Bi}_2\text{Se}_3$  or  $\text{SnTe}$ . Since these materials contain elements with large atomic numbers, they possess strong spin-orbit coupling, one of the preconditions for topological insulators. Furthermore, as discussed in Section 2.5, the incipient metals discussed here are narrow gap semiconductors. This facilitates the band inversion required to create topologically protected (surface) states. Indeed, a number of compounds have been identified as topological insulators as displayed in **Figure 14**. In this figure, compounds that form a topological insulator are marked by yellow circles.<sup>[59,60]</sup> All materials that are depicted but are not marked by a yellow circle do not form a topological insulator. Please note, that in some cases materials form a topological insulator but not for the phase that has been characterized in this study. As Figure 14 shows, many chalcogenides such as  $\text{PbTe}$ ,  $\text{PbSe}$ , and  $\text{PbS}$ , but also  $\text{Bi}_2\text{Te}_3$ ,  $\text{Bi}_2\text{Se}_3$ , and  $\text{SnTe}$  form topological insulators. Yet, this information was known, before the concept of metavalent bonding has been introduced. Hence, one can raise the question if this concept provides any insights, which can help to tailor topological insulators. There are two reasons why the concept of MVB provides relevant insights to scientists working on topological insulators and their applications. As discussed in more detail in chapter 3, thin films of materials that show MVB possess a pronounced thickness dependence of the atomic arrangement and their properties, which can be attributed to the competition between electron delocalization and electron localization. Furthermore, in the relevant chalcogenides, the Fermi energy is often located in

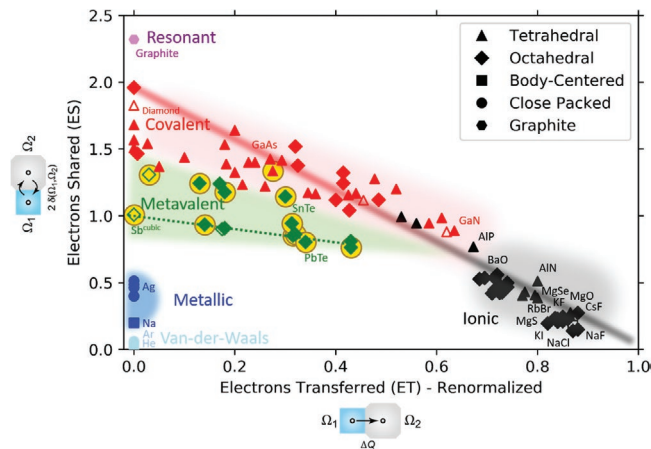


**Figure 14.** Correlation between the existence of a topological insulator phase and the bonding mechanism. 2D map using the basal plane of electrons transferred (ET, i.e., renormalized by the oxidation state) and electrons shared depicting materials which have phases, which are topological insulators by yellow circles. See text for further details.

the valence band (sometimes in the conduction band instead) since defects like vacancies can easily form in these materials. Under these circumstances, the electrical conductivity is dominated by a contribution from the bulk and not by the topologically protected surface states. This has been attributed to the ease of vacancy formation in these chalcogenides, which has been explained by the existence of antibonding states right at and below the Fermi energy.<sup>[61]</sup> In such a case, it is favorable to depopulate these antibonding states by vacancy formation. So, also regarding topological insulators one could look for systematic trends in the number of charge carriers versus map position.

## 2.8. Ultrathin Films of $\text{SnTe}$ and $\text{GeTe}$

In recent years, there have been several studies of the property dependence on film thickness in materials, which have been identified as topological insulators. In particular, for  $\text{Bi}_2\text{Se}_3$ <sup>[62]</sup> and  $\text{SnTe}$ ,<sup>[63]</sup> a pronounced dependence of the bandgap and the optical properties on the film thickness has been reported. It is intriguing to raise the question if this effect can be related to metavalent bonding, too. We have argued that MVB is characterized by a competition of electron delocalization as in metals and electron localization as in ionic or covalent compounds. Reducing the dimensions of the sample should thus impede electron delocalization, changing the structure and properties of thin films. Indeed, such effects have been reported for  $\text{SnTe}$  and  $\text{Bi}_2\text{Se}_3$  thin films. Hence, before progressing to the effect of nanoscale confinement on specifically phase change materials (PCMs), it is interesting to discuss materials possessing MVB showing unique behavior when scaled down to a few or monolayer dimensions.

$\text{SnTe}$  is an interesting case. It is not suitable for applications as a phase change material, since its amorphous phase is not stable enough against crystallization at room temperature. Nevertheless, it is located in the region characteristic for MVB in Figure 2. Furthermore, it is known for its superconducting,



thermoelectric and ferroelectric properties<sup>[64]</sup> and also as a topological crystalline insulator.<sup>[65]</sup> Its richness in properties likely stems from the competition of electron delocalization and electron localization, which characterizes MVB. This is closely associated with tunable structural instabilities.<sup>[66,67]</sup> Recently, it was discovered that the ferroelectric transition temperature  $T_c$  was as high as 270 K for 2 atomic layer (AL) thick SnTe films grown on graphene substrates by van der Waals epitaxy, whereas the  $T_c$  of bulk SnTe is only about 100 K.<sup>[63]</sup> This behavior is opposite to all ferroelectrics known at that time where  $T_c$  decreases when films approach the nanometer scale range. When the SnTe films were grown with a thickness above 10 nm their properties corresponded to those of bulk material.<sup>[68]</sup> The origin of the enhancement of  $T_c$  in ultrathin SnTe films, and a series of related phenomena, such as the dramatic reduction of defect concentration and the increase of its bandgap, were still open questions in 2016. The associated perspective article already coupled SnTe to MVB (referred to as resonant bonding at that time) and to a material at the cross-point of several competing structures, including possibly even the layered orthorhombic phase.<sup>[66]</sup>

Very recent papers now shed light on the peculiar behavior of ultrathin SnTe films.<sup>[64,67]</sup> As generally holds for MVB, there are three p electrons that stabilize six nearest neighbor bonds in an octahedral-like fashion. The basic structure is of rock-salt type ( $\beta$ -SnTe), but at low temperature, a Peierls-like rhombic distortion along one of the four  $\langle 111 \rangle$  directions takes place resulting in the  $R3m$  symmetry, which is a ferroelectric phase ( $\alpha$ -SnTe). This type of distortion is also characteristic for MVB and similar behavior is shown by GeTe (see Figure 7). The transition temperature  $T_c$  is 670 K for bulk GeTe, while it is only about 100 K for bulk SnTe. Both of these two materials, like many PCMs, suffer from a large amount of intrinsic cation vacancies,<sup>[61]</sup> which creates a p-type carrier concentration as high as  $10^{20}$ – $10^{21}$  cm<sup>-3</sup>, incompatible with robust ferroelectric behavior. Now the solution of the puzzle appears to be that in the ultrathin films a third structure is observed, a layered orthorhombic phase with the  $Pnma$  ( $\gamma$ -SnTe) space group, that also occurs at room temperature when a pressure higher than 18 kbar is applied to SnTe.<sup>[67,64]</sup> This  $\gamma$ -SnTe has an antipolar orthorhombic van der Waals structure and is isostructural to the stable (bulk) phase of SnSe. For a 2 AL film a net in-plane polarization occurs, but in a 4 AL film the pair of 2 ALs separated by a van der Waals gap align antiparallel and thus do not create a net polarization. For a 6 AL film again, a net polarization occurs. Since, compared to bulk SnTe, also the bandgap is dramatically increased and the charge carrier density is reduced by orders of magnitude when the film thickness is scaled down to 2 AL, robust ferroelectric behavior emerges. This example is intriguing, because it shows behavior typical for materials possessing MVB, being sensitive to distortions and thus external effects invoking such distortions which lead to large property changes. Moreover, this example probably shows the destruction of MVB prevailing in  $\alpha$ -SnTe to mixed ionic-covalent bonding in  $\gamma$ -SnTe, analogous when going from rock-salt SnTe to orthorhombic SnSe in the map depicted in Figure 2.

Also for ultrathin GeTe films striking observations have been made. GeTe is a well-known PCM of its own and even more

widely applied when combined with Sb<sub>2</sub>Te<sub>3</sub>. In addition, it is used in thermoelectric materials like TAGS,<sup>[69,70]</sup> a solid solution of GeTe and AgSbTe<sub>2</sub>. Recently, GeTe has also been shown to be the basis of the novel class of ferroelectric Rashba semiconductors.<sup>[71]</sup> As generally holds for (bulk) PCMs the crystalline phase is an incipient metal possessing MVB, whereas the amorphous phase shows predominantly covalent bonding as can be seen from its properties such as larger bandgap, reduced Born effective charge and lower ECoN. What happens for ultrathin films of GeTe? Of course when ultrathin films are grown at low temperatures such as room temperature, where the atomic mobility is insufficient, (metastable) amorphous films are formed. Upon growth at high temperature, well above the crystallization temperature of bulk GeTe, (stable) crystalline structures develop. However, ultrathin films of GeTe grown by molecular beam epitaxy (MBE) on a Si(111)-(1 × 1)-H substrate surface at a temperature as high as 260 °C, well above the crystallization temperature of bulk GeTe of 200 °C, turn out to be initially (up to four bilayers (BLs)) amorphous.<sup>[72]</sup> In contrast, when GeTe is grown using the same conditions on the Si(111)-( $\sqrt{3} \times \sqrt{3}$ )R30°-Sb surface it directly grows with a crystalline structure.<sup>[72]</sup> When the GeTe film is grown beyond four BLs on the Si(111)-(1 × 1)-H surface it switches to an epitaxial structure (for the entire film). These results show that the details of the initial surface are crucial for the type of structure that is formed in the thin film and therefore its properties (see another example in ref. [73]). This conclusion may sound rather obvious, but what is special here is that it can be associated with the switch from (predominantly) covalent bonding within GeTe films up to 4 BLs to MVB beyond 4 BLs. It could be a fingerprint that MVB depends sensitively on boundary conditions and this readily occurs when materials possessing MVB are confined to nanoscale dimensions. Hence, the observed unconventional dependence of structure and properties on film thickness for materials utilizing MVB can be related to their unconventional bonding mechanism.

### 3. Phase-Change Materials in Nanoscale Dimensions

The ability to scale down has been a critical requirement for any viable memory technology. The paradigm has been that a memory that cannot scale has no future. One of the strong points of phase change memory is that it appears to scale quite well.<sup>[74,75]</sup> Particularly for PCMs, scaling is required, not only to achieve higher data densities capable of processing larger amounts of information. It is also crucial to increase the power efficiency to switch between memory states. Yet, scaling is not only critical for the applications of PCMs, but it is also of fundamental interest to improve our understanding of this intriguing class of materials, showing so many remarkable properties. Hence, in the last section already peculiar properties were discussed in conjunction with MVB. In this section, we want to focus on the fundamental materials science aspects, hoping to systematically address the science of downscaling PCMs, where Section 3.1 focuses on thin films and Section 3.2 on nanoparticles, with particular emphasis on crystallization kinetics.

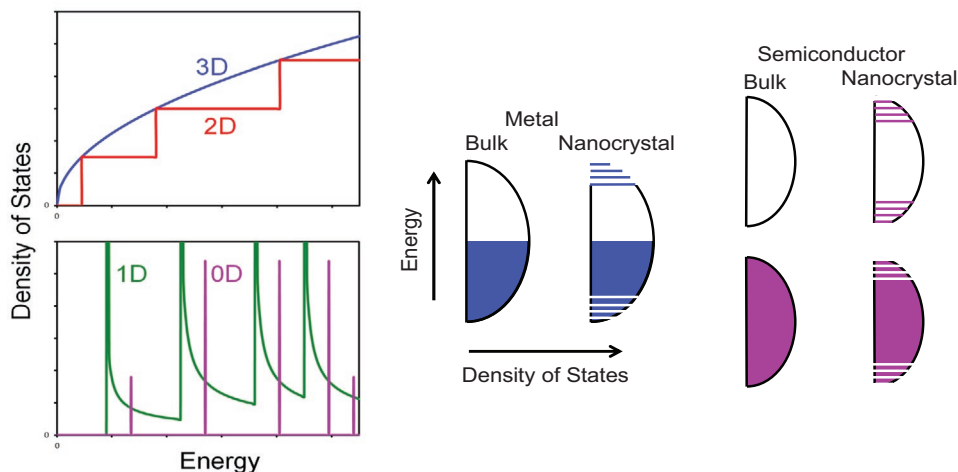


**Figure 15.** The fundamental physics of nanoscale confinement. Left: Density of states (DOS) in one band of a semiconductor as a function of dimension. Right: Schematic illustration of the difference in DOS of bulk and nanocrystals for metals and semiconductors, respectively. Figure inspired by ref. [77].

Reducing the size of materials toward the nanometer scale often has profound effects on their properties.<sup>[76–79]</sup> It can lead to properties that differ from those of the bulk material, but sometimes even provides novel or unique properties not found in the corresponding bulk materials or gives size-dependent behavior, which allows tailoring of properties for certain applications. These nanoscale size effects can have several physical origins, which for instance can be categorized as<sup>[76–79]</sup>

1. Large surface/interface area to volume ratio;
2. Quantum confinement;
3. Internal physical length scales in the material, e.g., correlation lengths like (magnetic, ferroelectric) domain wall widths, interact with limited object size;
4. In addition, we also expect unique nanoscale size effects in relation to MVB.

In phase-change materials (PCMs) mainly category 1 received attention and is considered to be the dominant effect for thin films. It will be reviewed in detail below. In the nanoscale object the fraction of atoms at the surface or interface is significant compared to atoms in the bulk and can be tuned by the object size. Related effects are the key role played by surface or interface energy, but also the stresses generated at interfaces or merely caused by the presence of free surfaces of nanoscale objects. The latter effect seems counterintuitive, because stresses can relax at free surfaces and the component perpendicular to the free surface must be zero. Still, a nanoparticle (which does not have to be spherical) with a size  $d$ , experiences an internal pressure that scales with  $\gamma/d$ , where  $\gamma$  is the surface energy.<sup>[80]</sup> Stresses can thus become huge when the nanoparticle reaches a size of one nanometer and can even induce phase transformations.<sup>[81,82]</sup> However, in thin films the internal pressure remains effectively zero, even if the film is scaled down to its ultimate limits. In this case, stresses can only be induced at the film substrate interface and can only act in-plane (and not out-of-plane).

This last paragraph shows the importance of making a proper distinction between the dimensions of down-scaling.

The effects of down-scaling are rather different for thin films, nanowires, or nanoparticles (either with free surfaces or embedded). For instance, the above mentioned category 2, quantum confinement, has a rather limited effect on thin films, but has a large impact on nanoparticles, in particular when of semiconductor type. To explain this more clearly, **Figure 15** is instrumental. It shows that downscaling initially only affects the (valence and conduction) band edges: the density of states (DoS) at these edges becomes quantized for thin films in steps, for nanowires in Van-Hove singularities characteristic for 1D systems and for nanoparticles the DoS approaches discrete atomic-like states. Now, since for metals the Fermi level is somewhere in the middle of the band, they remain unaffected by down-scaling as long as the size is over a few hundred atoms and the temperature is above a few Kelvin. For semiconductors, the Fermi level is centered in the bandgap and thus the electrical and optical behavior is rapidly affected by down-scaling, leading to pronounced size effects at room temperature for particles as large as 10 nm (see Figure 15).<sup>[77]</sup>

For PCMs the picture that thus emerges is that quantum confinement will hardly affect thin film properties, but can be quite relevant for nanoparticles or confined PCM volumes that will play an increasingly important role in aggressively downscaled phase change memory.<sup>[51,83,84]</sup> Of course the above picture is still oversimplified, because, for instance, it only holds for crystalline materials and is based on a free electron gas. The DoS of amorphous and crystalline semiconductors show important differences.<sup>[85]</sup> Moreover, the crystalline state of PCMs is generally considered metallic, in the sense that the Fermi level does not lie in the bandgap, but instead in a region with a significant DoS. Crystalline PCMs, particularly GeSbTe or GeTe alloys with structures close to the rocksalt one, are in general degenerate p-type semiconductors with the Fermi-level situated within the top of the valence band.<sup>[32]</sup> Therefore, quantum confinement can still affect the low resistance state for three-dimensionally confined PCMs (either as free particles or embedded volumes). To the best of our knowledge proof for explicit quantum confinement effects observed for PCMs is still lacking and in view

of the analysis presented here, deserves prime attention in future research. An additional intriguing open question is how specifically MVB will cope with and react to size effects within the above three categories including interfaces and quantum confinement. Some preliminary thoughts on this topic will be given in Section 4, while some initial results have been presented in Section 2.7.

### 3.1. Confinement in Thin Films

Very abundant is the PCM literature on the role played by interfaces when PCM films become progressively thinner. A hot topic of research in the field of PCMs, where interfaces play a dominant role, is centered around chalcogenide superlattices (CSLs), in particular superlattices formed by alternating units of  $\text{Sb}_2\text{Te}_3$  and  $\text{GeTe}$ . The excitement about CSLs is mainly due to the reported superior memory performance of these  $\text{Sb}_2\text{Te}_3$ - $\text{GeTe}$  superlattices compared to ordinary  $\text{Ge-Sb-Te}$  alloys (on the  $\text{Sb}_2\text{Te}_3$ - $\text{GeTe}$  tie-line), which rely on switching between amorphous and crystalline phases.<sup>[86]</sup> This new memory type based on CSLs has been coined initially iPCM (interfacial phase change memory)<sup>[86]</sup> and in a later stage also TRAM (topological-switching random access memory).<sup>[87]</sup> The former name stresses the importance of the interfaces present in the superlattice for the memory performance and the latter name highlights the potential role played by topological insulating behavior of the materials and its interfaces. Indeed, one of the sublayers of the CSL,  $\text{Sb}_2\text{Te}_3$ , is a well-known topological insulator.<sup>[88,89]</sup> This also holds for specific types of atomic stacking in the trigonal GST structures.<sup>[90]</sup>  $\text{GeTe}$  can be considered a normal insulator. Still, in its ground state it experiences a kind of Peierls distortion<sup>[32]</sup> leading to weak ferroelectric order with polarization along the<sup>[108]</sup> axis of the rhombohedral lattice (which is the [0001] axis when hexagonal notation is used for the trigonal structure) (see Figure 7). Therefore, the interfaces between  $\text{Sb}_2\text{Te}_3$  and  $\text{GeTe}$  may show special behavior, where the conductive states at the interfaces may be switched on or off by electrical field or potentially also stress (pressure).<sup>[90]</sup> Still, there is strong scientific debate about the actual mechanism that causes the improved performance of the CSL memory over the traditional GST memory. Since several recent reviews have addressed the current understanding and the open issues in this field<sup>[91,92]</sup> the present review will not focus on iPCMs. Instead, in the next sections, the focus will be on how nanoscale confinement in thin films and nanoparticles will affect the properties of PCMs with particular attention to a fundamental property, namely the crystallization temperature  $T_X$ . Maybe at first sight this does not appear as such a spectacular property. However, as the review below will show there is, similar to the glass transition temperature  $T_g$ , rich but also poorly understood physics underlying these transition temperatures. During glass formation, the microscopic structure of the material, as probed by, e.g., the radial distribution function  $g(r)$  or static structure factor  $S(k)$ , undergoes only very minor changes, yet both the viscosity and dynamic relaxation time increase by many orders of magnitude.<sup>[93]</sup> It is this seemingly paradoxical discrepancy between structure and dynamics that makes the glass transition such a difficult

theoretical problem already for the bulk, let alone for thin films and nanoparticles.

The influence of nanoscale size effects on the behavior of materials is a large branch of research in materials science. In PCMs, we have an additional property portfolio, because we are not only interested in the nanoscale size effects on the properties of a singular material, but particularly how they affect the transition between two (solid) phases of a material. In fact, most attention in the PCM literature has been on this latter effect and much less on how size effects influence the properties of the separate phases. This attention is also obvious given the importance of the phase transition for the applications of PCMs. Still, in addition, the reversible phase transition between the amorphous and crystalline material can be used as an effective sensor to monitor the influence of size effects. A property that relies on the difference between two phases can be more sensitive to size or other effects than the property of a single phase.

#### 3.1.1. Crystallization Temperature of PCM Thin Films

One of the most central properties of PCMs, relying on the difference mentioned in the last sentence of the previous section, is the crystallization temperature, here denoted as  $T_X$ . It is a strong indicator of the amorphous phase stability and thus data retention. Although it is standard procedure to determine the  $T_X$  of any newly synthesized PCM, there is no such thing as a single and unique value of  $T_X$  for a given PCM.  $T_X$  is dependent on thermal history, which most commonly is dictated by the heating rate. It is well known that  $T_X$  increases with increasing heating rate, an effect widely used to study the kinetics of the phase transformation, e.g., by applying the so-called Kissinger analysis.<sup>[94,95]</sup> So, instead of  $T_X$  it would be better to use the glass transition temperature  $T_g$ , because it is a better defined quantity. However,  $T_g$ -values of PCMs are generally not or very poorly known. PCMs must be poor glass formers (since it is required that only with very high cooling rates they become a glass) and upon heating the glass transition is then not visible as it is generally obscured by direct crystallization.<sup>[96]</sup> Only with special pretreatments it is sometimes possible to reveal  $T_g$ .<sup>[96,97]</sup> Therefore, it remains more practical to use  $T_X$ , but nevertheless it would be better if the PCM community would define it for a fixed slow heating rate, e.g.,  $10 \text{ K min}^{-1}$ . Yet, it is also important to know how high  $T_X$  is for the huge heating rates that are employed in practical applications.

Before focusing on the size dependence of  $T_X$ , an even more significant effect on  $T_X$  than heating rate has to be addressed. It is the actual amorphous (starting) structure of the PCM. In general, PCMs are initially deposited in an amorphous state, e.g., using sputter deposition. Then, reversible cycling between the crystalline and the amorphous phases occurs via melt-quenching. It has been shown, over and over again, that the crystallization kinetics can be dramatically different for the as-deposited amorphous phase and the melt-quenched amorphous phase (see an example in Figures 16 and 17a). Seminal work has been performed by van Pieterse et al.<sup>[98]</sup> in the realm of optical disks (where of course melt-quenching is achieved using laser pulses). For all (at least 12) investigated

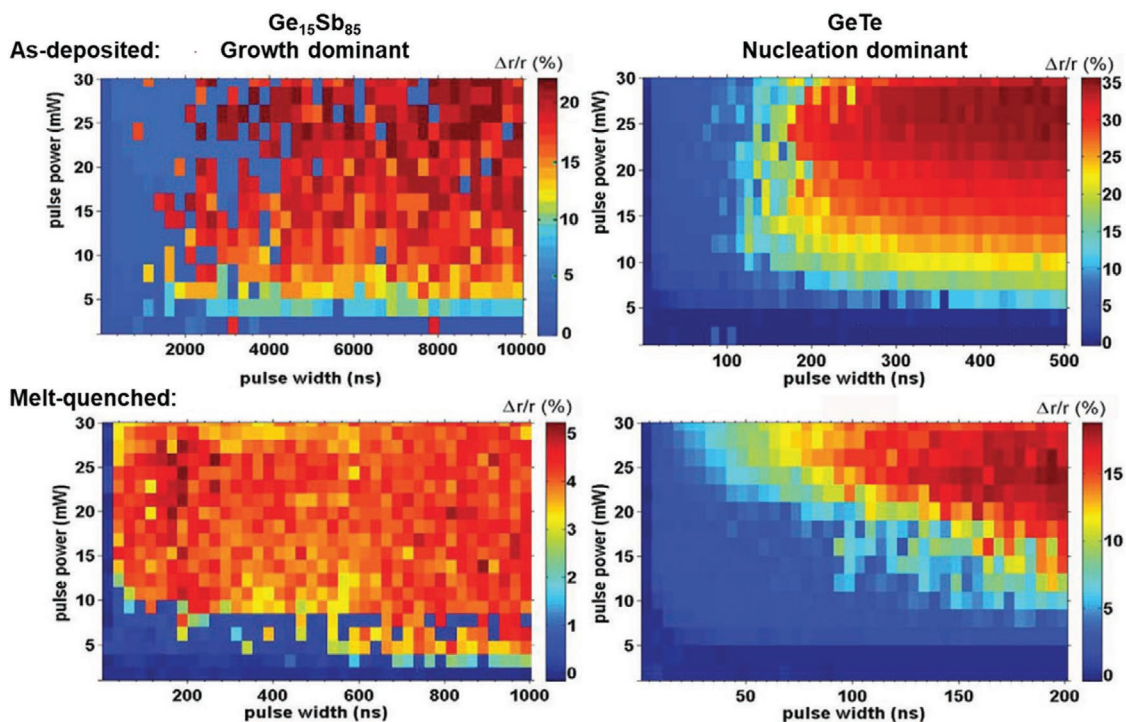


**Figure 16.** Crystallization speed of as-deposited and melt-quenched phase-change materials. Results of static laser tests for two amorphous PCMs, growth dominant  $\text{Ge}_{15}\text{Sb}_{85}$  on the left and nucleation dominant  $\text{GeTe}$  on the right, where pulse power is plotted versus pulse width. The color scale indicates the relative difference in reflectance achieved: when blue the phase stays amorphous and when red indicates switching to the crystalline state. The top row shows results for as-deposited amorphous phase and the bottom row for melt-quenched amorphous phase. Melt-quenched amorphous phase crystallizes faster; in particular, for the growth dominant material a dramatic increase is observed. Reproduced with permission.<sup>[100]</sup> Copyright 2009, Coach. Corp.

growth-dominated PCM alloys  $T_X$  decreases when going from the as-deposited to the melt-quenched structure. For  $\text{Ga}_8\text{Sb}_{77}\text{Te}_{15}$  the effect is most dramatic, where  $T_X$  was shown to decrease from 230 to 84 °C. It is unfortunate that in many later papers still PCMs with excellent data retention are proposed primarily based on the crystallization temperature of the as-deposited phase, see for instance.<sup>[99]</sup>

Unfortunately, it is less straightforward and thus relatively hard to determine  $T_X$  of melt-quenched PCMs. Widely used techniques to determine  $T_X$  are based on measuring the sheet resistance, optical reflectivity, differential scanning calorimetry (DSC) or temperature-dependent X-ray diffraction (XRD). This works for continuous thin films or when sufficient sample mass is available. Melt-quenching is possible by laser or electrical pulses in thin films, but then in general only small amorphous PCM volumes are produced. For such small samples sizes, it is not straightforward to determine  $T_X$ . Producing larger samples is almost impossible, since PCMs are such bad glass formers that they rapidly crystallize upon melt-quenching. Static laser testers have been powerful to scrutinize the crystallization behavior of many PCMs in particular also allowing comparison between the behavior of as-deposited and melt-quenched materials; see examples in Figures 16<sup>[100]</sup> and 17a.<sup>[101]</sup> Then the standard output is pulse power versus pulse width. The obvious result is then to determine the (maximum) crystallization speed, i.e., the minimum SET pulse duration to achieve, e.g., 90%

crystallization; see Figure 17a. Direct information on actual temperatures is then lost. The final outcome is that  $T_X$ -values are extremely well documented for as-deposited materials (but have limited meaning) and that crystallization speeds are documented to more limited extent for melt-quenched materials, but that  $T_X$ -values are generally lacking for melt-quenched materials.

### 3.1.2. Film Thickness Dependence

Now sufficient background information has been presented to properly address the film thickness dependence of  $T_X$ . Figure 17b shows as an example  $T_X$  as a function of film thickness for three different (as-deposited) PCMs, where  $\text{GeSb}$  is  $\text{Ge}_{15}\text{Sb}_{85}$  and  $\text{NGST}$  is nitrogen-doped  $\text{Ge}_2\text{Sb}_2\text{Te}_5$ .<sup>[74]</sup> These films are sandwiched between native  $\text{SiO}_2$  (on Si substrates) and  $\text{Al}_2\text{O}_3$ . For these three PCMs, a clear trend is observable that for thinner films  $T_X$ -values increase compared to the ones of the bulk (thick films). Typically, down to a thickness of 10 nm hardly any change in  $T_X$  occurs. Only below 10 nm thickness  $T_X$ -values increase dramatically. For the thinnest films, the increase can readily exceed 100 K. Similar results have been obtained for other as-deposited PCMs and in other studies when PCMs are sandwiched between oxides.<sup>[102]</sup> In fact, such results were earlier observed for amorphous Si and Ge films sandwiched between oxides or nitrides.<sup>[103–108]</sup> So, it appears a

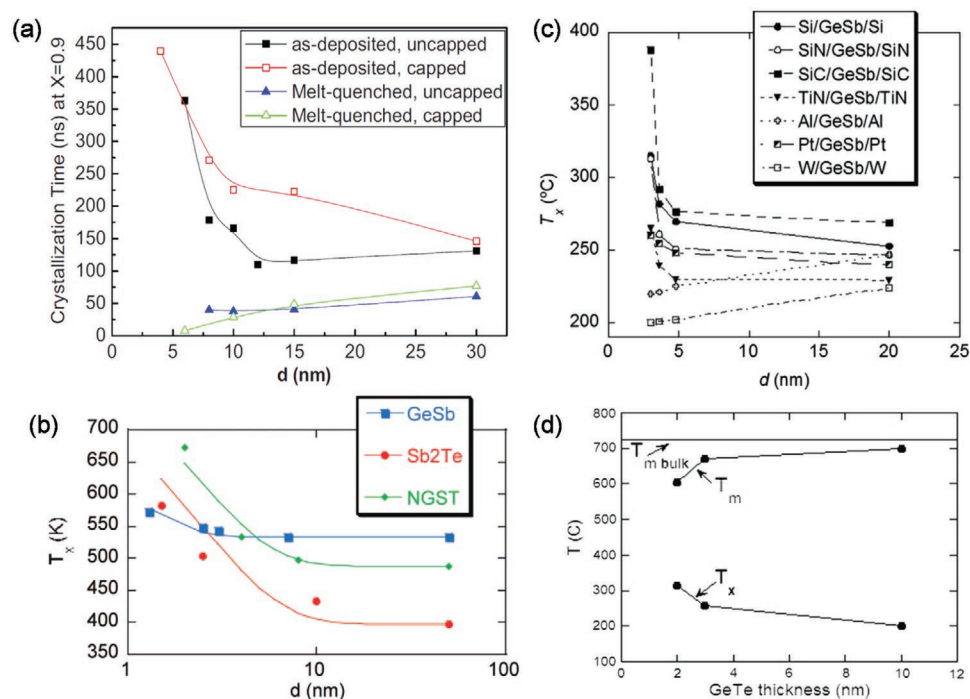


**Figure 17.** Size dependence of the crystallization temperature of PCM films. a) Crystallization time (to achieve 90% reflectance change related to one for full crystallization) versus film thickness for as-deposited and melt-quenched  $\text{Ge}_2\text{Sb}_2\text{Te}_5$ . Reproduced with permission.<sup>[101]</sup> AIP Publishing. b) Crystallization temperature  $T_x$  versus film thickness for three different (as-deposited) PCMs, where GeSb is  $\text{Ge}_{15}\text{Sb}_{85}$  and NGST is nitrogen-doped  $\text{Ge}_2\text{Sb}_2\text{Te}_5$ . Reproduced with permission.<sup>[74]</sup> AIP Publishing. c)  $T_x$  versus film thickness for  $\text{Ge}_{15}\text{Sb}_{85}$  sandwiched between the various layers as indicated in the legend. Reproduced with permission.<sup>[109]</sup> AIP Publishing. d) Crystallization temperature  $T_x$  and melting temperature  $T_m$  versus GeTe film thickness indicating a reduced temperature window for crystallization of ultra-for thin films. Reproduced with permission.<sup>[112]</sup> Copyright 2008, Elsevier B.V.

general trend that (amorphous) oxides (or nitrides) adjacent to as-deposited PCMs oppose crystallization.

When varying the type of layers between which a PCM is sandwiched, further remarkable results are observed. An example is provided in Figure 17c for  $\text{Ge}_{15}\text{Sb}_{85}$ .<sup>[109]</sup> In this case, the general trend of a dramatic increase in  $T_x$  below film thicknesses of 10 nm is not observed. The variation in  $T_x$  strongly depends on the type of sandwich layer. Here, it seems that some metal layers can decrease  $T_x$  when the PCM film thickness decreases (whereas nitride and carbide layers cause an increase). Again, similar results have been observed for amorphous Si and Ge films where metal-induced crystallization is a well-known phenomenon.<sup>[110,111]</sup>

### 3.1.3. Influence of Interfacial Energy

Based on these results in Figure 17c, it is very tempting to explain the film thickness dependence of  $T_x$  by the corresponding interfacial energy. It is obvious that when a film gets thinner its volume reduces (linearly), but the interfacial area remains constant and thereby the role played by the interface becomes increasingly dominant. Hence, qualitatively it must be possible to link the interfacial energy to an increasing  $T_x$  with decreasing film thickness. Indeed, a semiquantitative model has been developed to establish this link.<sup>[108]</sup> However, since basic assumptions in the model are debatable and some of them have even only been introduced to obtain the desired

known empirical outcome, this model cannot be used to explain what is actually causing the observed trend. Moreover, it only describes an exponential increase in  $T_x$  with decreasing film thickness and most data in Figure 17c do not comply with this behavior. Still, the solid lines in Figure 17b are based on this exponentially increasing behavior. It seems that proper quantitative models that describe the film thickness dependence of the crystallization temperature on the basis of interface energies are still lacking.

### 3.1.4. Influence of Surface Oxidation

Next to interfacial energy also other factors can contribute to the observed dependence of  $T_x$  on film thickness. A factor that must not be neglected is the effect of surface oxidation of the PCM. When the PCM films become progressively thinner, surface oxidation will have an increasingly dominant effect on properties and behavior of the films. Although it is known for a long time that oxidation of PCMs can have a huge impact on the crystallization in PCMs, see, e.g., an early work in ref. [113], systematic studies have been lacking. Only recently rigorous research has been performed to elucidate the influence of surface oxidation on the crystallization of  $\text{Ge}_2\text{Sb}_2\text{Te}_5$  and GeTe.<sup>[114,115]</sup> The general effect is that surface oxidation reduces  $T_x$ . For  $\text{Ge}_2\text{Sb}_2\text{Te}_5$  from 170 °C to 150 °C and for GeTe from 230 °C to 180 °C. Indeed, in most published work  $T_x$  of  $\text{Ge}_2\text{Sb}_2\text{Te}_5$  is in the range of 150–160 °C and therefore could be

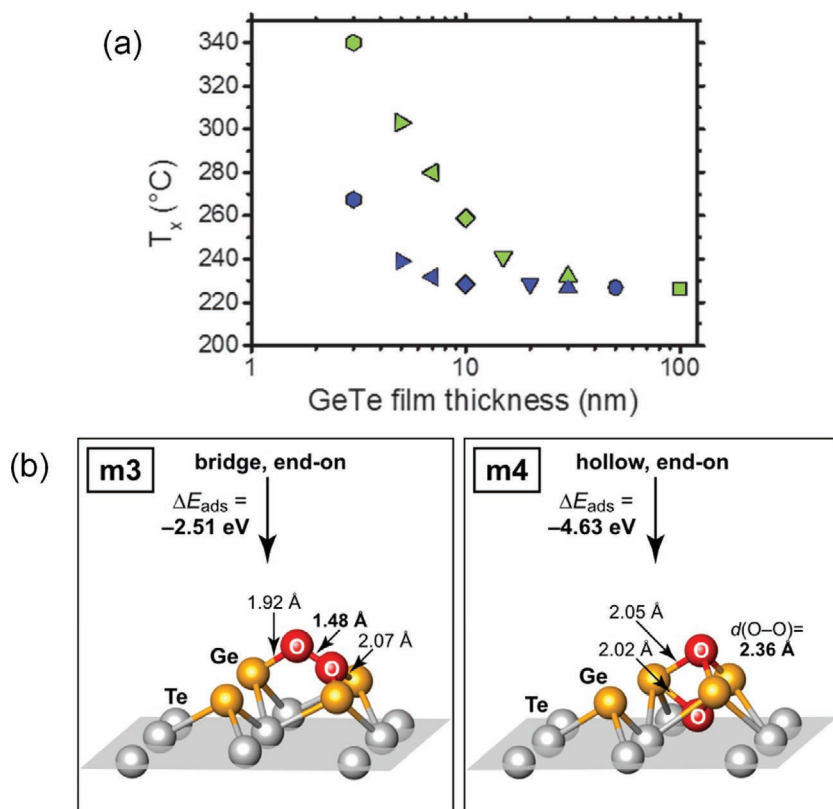


**Figure 18.** The role of surface oxidation. a) Crystallization temperature  $T_x$  of GeTe thin films as a function of the film thickness. Green symbols correspond to GeTe films that have been capped by a SiN protective layer without exposure to oxygen. Blue symbols correspond to GeTe films that have been briefly exposed to oxygen before deposition of the capping layer. Reproduced with permission.<sup>[84]</sup> IOP Publishing. b) Atomistic structural models of a GeTe surface in contact with an oxygen molecule. The left-hand side shows a configuration in which an  $O_2$  molecule has been adsorbed on the reactive Ge-terminated GeTe(111) surface, but not yet dissociated into its constituent atoms. On the right-hand side, a surface oxide has formed, concomitant with a substantial lowering of the computed total energy. Reproduced with permission.<sup>[116]</sup> Copyright 2014, AIP Publishing.

affected by surface oxidation (but of course variations in precise composition of the  $\text{Ge}_2\text{Sb}_2\text{Te}_5$  also cause variations in  $T_x$ ). Surface oxidation is not always prevented by capping layers. For instance, in situ applied  $\text{Ta}_2\text{O}_5$  capping layers, directly deposited after PCM film growth without breaking the vacuum, still provided the same result as uncapped films or capped films with 1 h air exposure before capping.<sup>[114]</sup> The effect of (minor) surface oxidation on the film thickness dependence of  $T_x$  is shown in **Figure 18a** for GeTe films.<sup>[84]</sup> Oxidation is minor, because otherwise already the 30 nm thick oxidized film would have a  $T_x$  of 180 °C and now it is still the same as the one of the non-oxidized film (close to the 220 °C). Nevertheless, a clear effect of oxidation on the  $T_x$  values for thinner films is observed. The oxidized films show a more modest increase in  $T_x$  with decreasing film thickness. Therefore, although statistics are limited, it is unlikely that surface oxidation can explain the general behavior that  $T_x$  increases for thinner PCM films sandwiched between oxides and nitrides. It seems that surface oxidation only dampens this behavior as evidenced in **Figure 18a** for GeTe films.

When viewing the oxidation of GeTe in more detail, DFT simulations have provided an in depth atom-resolved picture of how GeTe(111) surfaces interact with molecular and atomic oxygen; see **Figure 18b**.<sup>[116]</sup> The Te-terminated surface is unreactive toward molecular oxygen, in agreement with its overall stability<sup>[117]</sup> and forms no intermediary surface oxides.<sup>[118]</sup> The Ge-terminated GeTe(111) surface, on the contrary, reacts readily with oxygen as a means to stabilize itself. The reaction mechanism suggested by Yashina et al. on the basis of XPS measurements<sup>[118]</sup> has thus been corroborated by complementary DFT simulations.

### 3.1.5. Influence of Stress

A factor that can contribute to the observed dependence of  $T_x$  on film thickness is stress within the PCM film. As mentioned above the stress introduced by interfaces in thin films can only act in plane. Stresses can be introduced in the PCM as a result of thin film deposition (e.g., a small compressive stress has been observed in an amorphous  $\text{Ge}_2\text{Sb}_2\text{Te}_5$  film after deposition)<sup>[119,120]</sup> but in general these stresses are expected minor. A major source of stress is the amorphous-crystalline phase transformation, because it is in general associated with a large change in density. Typically, PCMs show a 5–10% increase in density (decrease in volume of 5–10%).<sup>[56,121]</sup> This would mean that a constrained PCM film would experience a tensile stress after crystallization. Indeed, this has been generally observed.<sup>[119,120,122]</sup> The only exception where a compressive stress is mentioned is in ref. [123], but results of the actual determination of the stress are lacking, whereas convincing (transparently obtained) results are shown in the cases of tensile stress. An important result is that the tensile stress is generally 100–200 MPa. However, when the total volume change would have been accommodated elastically, the stress must be on the order of 1–2 GPa. Hence, a large part (say 90%) of the stress is accommodated plastically, e.g., by viscous flow (and only 10% elastically).<sup>[120,58]</sup>

Now, it can be well understood that, when the volume change associated with crystallization is hindered by external constraints, this will impede crystallization. So, the harder an amorphous volume is confined the larger its increase in crystallization temperature. Still, this does not directly explain why  $T_x$  should increase with decreasing PCM film thickness. To demonstrate this, the results of **Figure 19** taken from ref. [120] are powerful. It shows the in-plane biaxial stress measured as a function of  $\text{Ge}_2\text{Sb}_2\text{Te}_5$  film thickness ( $h_{\text{GST}}$ ) for a fixed silicon nitride substrate thickness ( $h_{\text{SiN}}$ ). In fact, the substrate is relatively thin (218 nm), because it is a cantilever allowing

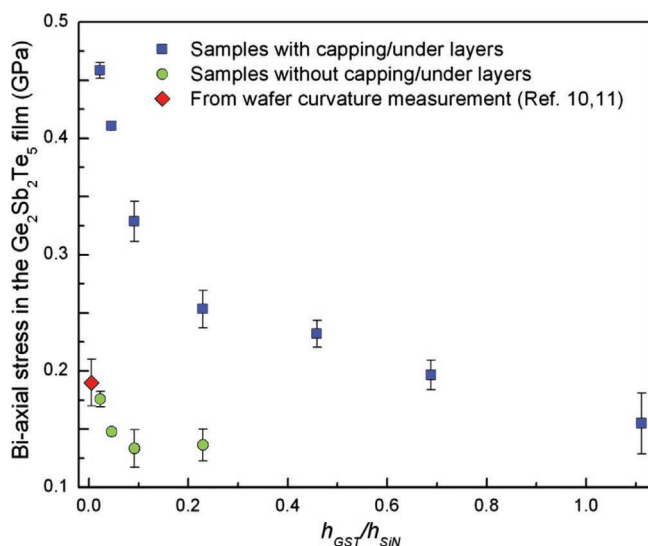


**Figure 19.** Film thickness dependence of in-plane stress in  $\text{Ge}_2\text{Sb}_2\text{Te}_5$  films. In-plane biaxial stress measured as a function of  $\text{Ge}_2\text{Sb}_2\text{Te}_5$  film thickness ( $h_{\text{GST}}$ ) for a 218 nm thick silicon nitride cantilever ( $h_{\text{SiN}}$ ). The (tensile) stress increases markedly for decreasing  $h_{\text{GST}}$ . GST films sandwiched between 5 nm  $\text{ZnS-SiO}_2(20-80)$  films show much higher stress than noncapped GST films having the same thickness. Reproduced with permission.<sup>[120]</sup> Copyright 2008, AIP Publishing.

by its deflection the determination of the thin film stress.<sup>[120]</sup> Figure 19 shows that the (tensile) stress increases markedly for decreasing film thickness. It also shows that the stress values in the GST films (of various thicknesses) sandwiched between 5 nm  $\text{ZnS-SiO}_2(20-80)$  films are much higher than the ones of the noncapped GST films with the same thickness. Again, when the density change upon crystallization would have been accommodated fully elastically then a stress on the order of 1–2 GPa is expected. The results thus clearly show that an increasing fraction of the volume change is accommodated elastically for a decreasing film thickness. So, plastic deformation becomes increasingly more difficult for thinner films. The most likely mechanism for plastic deformation is viscous flow in the amorphous matrix when crystals are formed. These results thus suggest that the viscosity of the amorphous phase increases when this phase is more confined in thinner films, particularly when also capped. (This was already suggested earlier to explain why crystal growth rates decrease when films become capped,<sup>[124]</sup> but at that time there were no explicit measurements supporting this view.)

Figure 19 is instructive, because, to explain the increasing  $T_x$  with decreasing PCM film thickness, there is now a direct correlation with the increasing in-plane biaxial stress. Similar as for  $T_x$  also the stress shows a nonlinear dependence on film thickness, with a strong upswing (kind of exponential increase) for the thinnest films. Although such a correlation is not a direct proof that the stress is responsible for the behavior of  $T_x$ , there is at least a much more explicit correlation than we could make earlier between  $T_x$  and interfacial energies. Still, factors like metal-induced crystallization can play an important role. When the interfacial energy of crystalline PCM and capping (or sandwich) layer is lower than the one of amorphous PCM and capping layer, this will mean that crystallization will

be increasingly promoted for thinner films where the effect of interface energy becomes more dominant. Similarly, when the interfacial energy of crystalline PCM and capping (or sandwich) layer is higher than the one of amorphous PCM and capping layer, this will mean that crystallization will be increasingly hindered for thinner films where the effect of interface energy becomes more dominant. So, in the end, it seems that a combined effect of interfacial energy and stress dictates the behavior of PCM scaled down to its ultimate limits (implicitly assuming that care is taken to avoid any oxidation of the PCM).

### 3.1.6. Separate Attention to Nucleation and Growth

Still, the discussion is not sufficiently settled. We have to take it another step further. Up to now little attention was devoted to the process of crystallization. Since we are concerned with a transformation between distinctly different phases, where latent heat is involved, the phase transformation is of first order type. This can only proceed via nucleation and growth. So, we must treat crystallization as a two-step process, where nucleation is inherently stochastic and growth is generally deterministic. One can wonder why and how this is relevant for  $T_x$ . At first sight, one can think that  $T_x$  is only linked to nucleation. However, most techniques can only detect  $T_x$  when sufficient volume is transformed clearly beyond the initial nucleation stage. For instance, (sheet) resistance requires percolation of the crystalline phase between the electrical contacts and this is only possible when a significant volume (at least several tens of percent) is transformed. Also in X-ray diffraction a sample still appears completely amorphous when in fact it consists of crystalline grains with sizes of only a few nanometers (the term “X-ray amorphous” is sometimes used for such samples). Only when the crystals grow to appreciable size (e.g., beyond tens of nm) crystallization is detected in XRD. So, growth is inherently involved when determining  $T_x$ .

The role of the heterointerfaces (i.e., with substrate or capping layer) and of stress can be that they only affect nucleation and not crystal growth in PCM films. However, this view is incorrect. There is currently sufficient experimental evidence that heterointerfaces also directly affect the crystal growth rate in thin PCM films. See two examples in Figure 20. Figure 20a,b holds for 20 nm thick Ge+In(8 at%) doped  $\text{Sb}_{3.3}\text{Te}$  films, which were either uncapped or sandwiched between 3 nm  $\text{GeCrN}$  films or  $\text{ZnS-SiO}_2$  films.<sup>[124]</sup> These films were analyzed using in situ heating in a transmission electron microscope (TEM), allowing separate analysis of nucleation and growth. In a TEM, the primary electron beam can influence the crystallization process.<sup>[125]</sup> Therefore, crystallization was performed by isothermal heating for fixed time intervals at elevated temperature without e-beam exposure and imaging was only performed in between these intervals when the sample was cooled sufficiently close to room temperature.<sup>[124]</sup> In this way, it is ensured that there is no influence of the electron beam on the crystallization process. Figure 20a shows, in an Arrhenius plot of crystal growth rate versus temperature, that both types of capping layers reduce the growth rate. This reduction is pronounced at lower temperatures around 160 °C and disappears at higher temperatures around 200 °C. In contrast, Figure 20b shows, in an Arrhenius

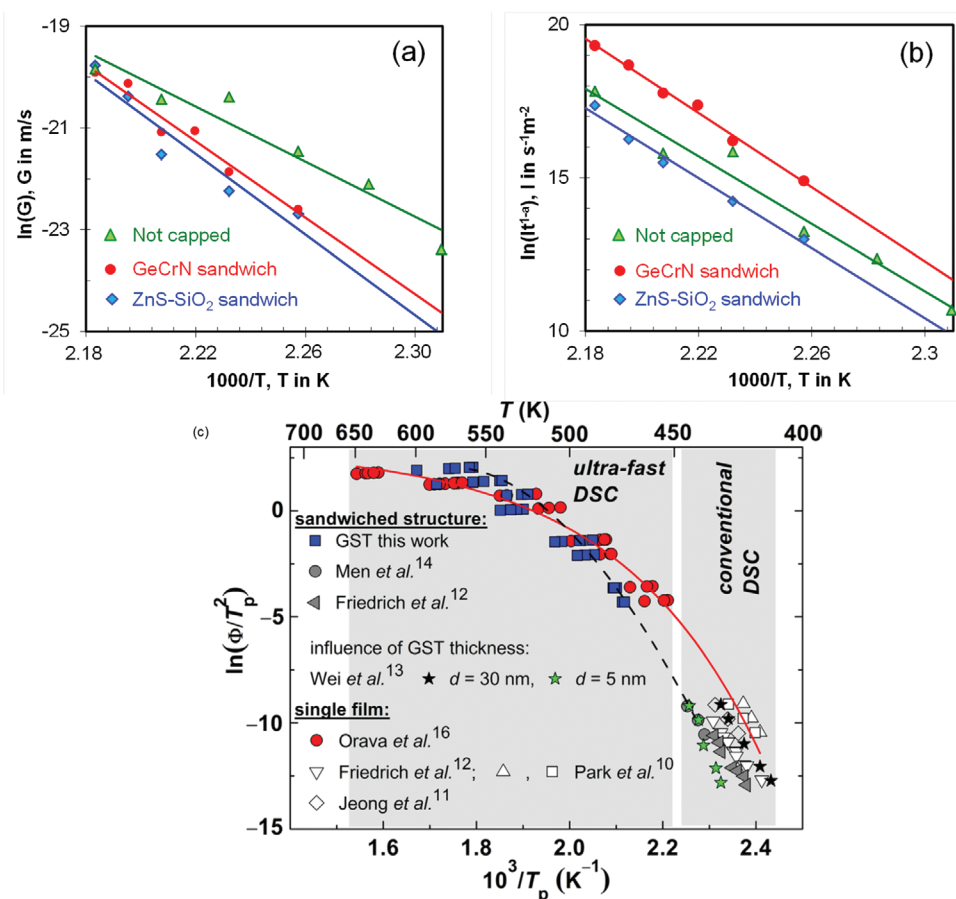


**Figure 20.** Arrhenius and Kissinger plots showing crystallization kinetics for not capped and sandwiched PCM films. a) Arrhenius plot of growth rate  $G$  versus temperature  $T$  for crystallization of Ge+In(8 at%) doped  $\text{Sb}_{3.3}\text{Te}$  films which were either uncapped or sandwiched between 3 nm GeCrN films or ZnS-SiO<sub>2</sub> films. b) Arrhenius plot of nucleation rate  $I$  versus temperature  $T$  for crystallization of Ge+In(8 at%) doped  $\text{Sb}_{3.3}\text{Te}$  films which were either uncapped or sandwiched between 3 nm GeCrN films or ZnS-SiO<sub>2</sub> films. c) Kissinger plot showing extensive DSC and ultrafast-DSC data for  $\text{Ge}_2\text{Sb}_2\text{Te}_5$  films either uncapped or sandwiched between dielectric layers. Reproduced with permission.<sup>[126]</sup> Copyright 2012, AIP Publishing.

plot of nucleation rate versus temperature, that GeCrN accelerates the nucleation by a factor of  $\approx 2$  whereas ZnS-SiO<sub>2</sub> decelerates it approximately four times.<sup>[124]</sup> So, a sandwich layer can reduce both nucleation and growth rate and thereby definitely increases  $T_X$ , but it can also accelerate nucleation and retard growth and then the net effect on  $T_X$  can vary (because it becomes dependent on the details of the method by which  $T_X$  is determined).

Figure 20c shows, in a Kissinger plot, results for  $\text{Ge}_2\text{Sb}_2\text{Te}_5$  films mainly obtained using ultrafast DSC.<sup>[126]</sup> Similar like in an Arrhenius plot, if data are lying on a straight line in a Kissinger plot, the slope of the linear regression is a direct measure of the activation energy of the phase transformation. A Kissinger plot only provides the activation energy for the overall transformation and not separately for nucleation and growth. In the undercooled liquid (UCL) state, strong liquids show Arrhenius-like behavior when their viscosity is plotted against the  $T_g$ -scaled inverse temperature. Fragile liquids on the other hand, exhibiting highly non-Arrhenius behavior, show a much steeper decrease in viscosity with increasing temperature just above the glass transition temperature.<sup>[127]</sup> The viscosity is (inversely proportionally) related to the atomic mobility via

the Stokes-Einstein relation (or via a fractional Stoke-Einstein relation<sup>[128]</sup>). Since the crystal growth rate and the nucleation rate are both limited by the kinetic factor (i.e., atomic mobility),<sup>[129]</sup> there is also a direct link between crystal growth rate, the nucleation rate, and viscosity.<sup>[96,130]</sup>

When the Avrami exponent is close to the dimensionality of the crystallization process (3 for flakes), it holds that the overall activation energy is dominated by the one for growth, since in this case all grains form first before crystallization is completed by grain growth.<sup>[96,124,130-132]</sup> For all other cases, nucleation and growth occur simultaneously and the Kissinger plot as given in Figure 20c gives insights in the combined effect of nucleation and growth. However, in Figure 20c, an Avrami exponent of 3, a glass transition temperature of  $T_g$  383 K and crystallization from the undercooled liquid (UCL) phase are assumed,<sup>[126,130]</sup> leading to the curved line (e.g., the solid red one) that is fitted to the data. Based on these assumptions, this curvature is supposed to represent the fragile behavior of  $\text{Ge}_2\text{Sb}_2\text{Te}_5$  in its undercooled state.<sup>[126,130]</sup> In this case, the vertical axis in Figure 20c corresponds to the logarithm of the crystal growth velocity, neglecting the effect of nucleation during crystallization (because of the assumed Avrami



exponent of 3). The effect of fragile behavior would be that the crystal growth velocity increases strongly just above the glass transition temperature and that this growth rate increase diminishes markedly at higher temperature when we are still in the regime where mobility is the rate limiting step for crystal growth. Of course, at even higher temperatures, when the melting temperature is approached, it is not anymore the mobility that is the rate limiting factor for crystal growth, but it is the small driving force for crystallization. Then, the crystal growth rate will eventually start to decrease and becomes zero at the melting temperature.

In contrast to the interpretation that  $\text{Ge}_2\text{Sb}_2\text{Te}_5$  crystallizes from the UCL, even at low heating rates, a later study on  $\text{Ge}_2\text{Sb}_2\text{Te}_5$  flakes came to a different conclusion.<sup>[96]</sup> Here, first the Avrami exponent of 5.8 was found to largely exceed the value of 3 clearly showing that  $T_X$  and therefore also the data in the Kissinger plot are a consequence of the interplay of both nucleation and growth. Moreover, the glass transition temperature was approximated from the heat release due to structural relaxation of the glass to be about 473 K, i.e., 90 K higher than assumed in the earlier study. The heating rate dependence of  $T_X$  was measured by ultrafast DSC, as in Figure 20c, but was extended to conventional DSC yielding an unprecedented heating rate interval spanning over six orders of magnitude. In combination with a high data density in the Kissinger plot, it is observed that  $T_X$  shows Arrhenius behavior from below 0.01 to  $10^4 \text{ K s}^{-1}$ . The observed Arrhenius behavior is incompatible with the hypothesis that  $\text{Ge}_2\text{Sb}_2\text{Te}_5$  crystallizes from the UCL, but instead it must crystallize from the glassy phase. This statement indicates that the glass transition in conventional or ultrafast DSC scans is obscured by crystallization. As the heating rate exceeds a critical rate of  $10^4 \text{ K s}^{-1}$ , the Kissinger plot shows a fourfold drop in activation energy, which was successfully described by modeling the crystallization when an instantaneous glass transition was introduced at that critical rate. So, in summary, the results of this study imply that this PCM crystallizes from the glass phase at rates below  $10^4 \text{ K s}^{-1}$  (and only from the UCL above this rate).<sup>[96]</sup>

Regardless whether  $\text{Ge}_2\text{Sb}_2\text{Te}_5$  crystallizes from the UCL or a glassy state, it is interesting that Figure 20c, like Figure 20a, shows that capping or sandwiching the PCM film reduces the crystal growth rate compared to uncapped films at temperatures below about 500 K. This reduction is most pronounced in the conventional DSC regime at about 400 K. The observed behavior suggests a relation between viscosity and stress. In the UCL at higher temperatures like 500 K, the viscosity decreases sufficiently to allow 1) relaxation of stress and 2) removal of the difference in crystal growth rate between capped and uncapped films.

### 3.1.7. Central Role Played by Viscosity

When two phases are in thermodynamic equilibrium, it is well known that the equilibrium temperature in general will shift when a stress is applied to the system. A compressive stress will favor the denser phase. When stress is replaced by pressure, the change in equilibrium temperature with pressure can be related to the Clausius-Clapeyron equation. Therefore, a direct

relation between stress and the transition temperature from the amorphous to the crystalline phase, say  $T_X$ , might be expected. However, this is a wrong view. At  $T_X$  or  $T_g$  the amorphous and crystalline phases are not at all in equilibrium. The amorphous phase is in thermodynamic sense extremely unstable compared to the crystalline phase, because we are at a huge undercooling compared to the equilibrium temperature, which is the melting temperature.<sup>[130]</sup> The only reason it cannot make the transition to the crystalline phase is its too limited atomic mobility. Stress can, therefore, not be a direct thermodynamic driving force for a change in  $T_X$ , but stress can only be a factor altering mobility, particularly via viscosity. Moreover, when there is sufficient mobility at higher temperatures stress will also relax and then cannot affect the viscosity anymore.

So, the more likely conclusion is that we have to reconsider, actually reverse the outcome of Section 3.1.5. The direct correlation between the increasing  $T_X$  with decreasing PCM film thickness and the increasing in-plane biaxial stress with decreasing PCM film thickness is not present because stress determines  $T_X$ . It is present because viscosity determines both stress and  $T_X$ . For thinner films, particularly when capped or sandwiched, the viscosity increases. The increasing viscosity reduces the mobility and the crystallization rate and thereby increases  $T_X$ . The increasing viscosity also reduces viscous flow, reduces plastic deformation, and thereby increases residual elastic stress associated with the amorphous-crystalline density change. Now it seems that many words were spent (hopefully still an interesting journey) to arrive at a relatively trivial conclusion: The observed increase in  $T_X$  in PCM (or any amorphous) films when they become thinner is particularly caused by an increasing  $T_g$  for decreasing film thickness and due to capping. Although this is of course not a new finding for glass-forming materials in general, as many papers have been devoted to this topic,<sup>[133–137]</sup> still this simple view is not sufficiently adopted in PCM literature when considering downscaling and confinement of PCMs.<sup>[83,84,102]</sup> This lack of attention is also not so surprising, because as quoted from<sup>[93]</sup> “although glasses are everywhere around us and fulfill important functions, we still understand very little about them.” In fact, after decades of intense research, there is still little consensus on which physical mechanisms underlie the process of glass formation. Unraveling the nature of the glassy state ranks among the “most compelling puzzles and questions facing scientists today,”<sup>[138]</sup> and Nobel laureate Philip Anderson even called it “the deepest and most interesting unsolved problem in solid-state theory.”<sup>[139]</sup>

The observed increase in  $T_X$  in PCM films when they become thinner as caused by an increasing  $T_g$  for decreasing film thickness and due to capping can in the context of Section 2 of the present review also be related to a weakening of MVB towards (ionic-)covalent bonding stabilizing the amorphous phase. Still, the bottom line at the moment is that  $T_g$  is not a material parameter. It is a system parameter including the dependence on the boundary conditions (including chemistry and roughness).<sup>[135]</sup> Even for a thin film  $T_g$  is not a constant but it is a function of distance to the interface and the surface, where  $T_g$  can, compared to the bulk value, increase directly adjacent to the interface and decrease for the free surface.<sup>[134]</sup> For low-molecular-weight glass formers, like PCMs, the affected length scale away from the interface then ranges from several

nanometers to several tens of nanometers.<sup>[134]</sup> For polymers, it ranges from tens of nanometers to beyond 100 nm.<sup>[134]</sup> Therefore, the size effects in PCMs are not only dominantly determined by the surface/interface to volume ratio, but also by correlation lengths within the PCM; see the categories 1 and 3 explaining confinement effects at the beginning of this Section 3. So, the final message concerning crystallization of nanoscale confined PCMs is that we should not forget about interfacial energy and stress, but that we must particularly pay more attention to viscosity.

A positive finding is that an increased viscosity and thus an increased  $T_x$  due to capping of the PCM or due to thinner PCM films do not have to be detrimental for the switching speed. The reason is that for increasing temperature the effect of confinement, particularly for fragile liquids, is rapidly vanishing. It is now widely believed that the slow dynamics of a supercooled liquid is related to the increasing correlation length of cooperative motions when  $T_g$  is approached.<sup>[136]</sup> The other way around, when the temperature is increased the large dynamic correlation lengths present near and below  $T_g$  in the undercooled liquid are rapidly replaced by shorter ones. So, effects that stabilize the amorphous phase and retard the crystallization at low temperatures near  $T_g$  do not have to slow down the maximum crystallization rate at higher temperatures as is demonstrated in Figure 20c, but also particularly in Figure 17a. There a large difference in the maximum crystallization speed (due to both nucleation and growth) is observed between as-deposited and melt-quenched GST, but the difference between capped and uncapped for both types of amorphous phases is clearly less significant. Even more interesting, for the melt-quenched GST, the crystallization speed increases when going to thinner films (see Figure 17a).<sup>[101]</sup> These results thus promise the best of both worlds. The analysis above (actually from Section 3.1.1 to 3.1.7) thus shows that thinner capped PCM films can show a better data retention at low temperatures around and below  $T_g$ , but simultaneously can still show a higher crystallization rate and thus switching speed at high temperatures sufficiently below  $T_m$ .

### 3.1.8. Melting Temperature of PCM Thin Films

After this positive message, there is still a reason for caution and that is the influence of size effects on the melting temperature  $T_m$  of PCMs. It is well known that the  $T_m$  of nanoparticles reduces dramatically when their sizes become smaller than 10 nm,<sup>[140–143]</sup> as also will be discussed in more detail in the next Section 3.2. This is mostly associated with the effect of surface melting, where free surfaces melt at temperatures much lower than the bulk one.<sup>[144,145]</sup> Reduced melting temperatures may seem technologically favorable for PCMs, since they lead to reduced power requirements for switching via the melt-quench route,<sup>[102,112]</sup> but a strongly reduced temperature window between  $T_g$  and  $T_m$  will also strongly reduce the achievable maximum crystallization rate and will thus have a negative effect on the switching speed of the memory; see Figure 17d.<sup>[112]</sup> Literature and data about the influence of size effects on the melting temperature of PCMs are relatively scarce. The general trend for thin films, nanowires, and nanoparticles indeed is

that the melting temperature is reduced.<sup>[112,146,147]</sup> Still, the results do not appear too bad, since the melting temperatures of GeTe decreases from 725 °C (bulk value) to 600 °C when the film thickness is reduced to 2 nm;<sup>[112]</sup> see Figure 17d. Note that these GeTe films are sandwiched between SiO<sub>2</sub> and therefore the melting temperature reduction is probably more modest than for a free surface. Of course a comparison with GeTe films with a free surface does not make sense, because then surface oxidation would make it a failed experiment. So, although the general effect is that the melting temperature reduces significantly for free surfaces, this does not have to be always the case for interfaces. For instance, superheating has been observed for Pb and In nanocrystals embedded in an aluminum matrix.<sup>[148,149]</sup> These experimental results indicate that the enhancement or depression of the melting temperature of the embedded nanoparticles depends on the epitaxy between the nanoparticles and the embedding matrix. Although epitaxy is clearly not a preferred strategy for confined PCMs, these results nevertheless show that there is plenty of room for interface engineering to optimize the melting behavior of PCMs. In case interfaces reduce the melting temperature significantly, it allows for choosing a PCM with higher bulk  $T_m$ , although this seems less preferable than interface engineering to maintain a desirable  $T_m$  close to the one of the bulk.

### 3.1.9. Ultrathin Monatomic Phase-Change Memory

To finalize this section, it is worthwhile to discuss recent fascinating work on monoatomic phase change memory.<sup>[150]</sup> The current paradigm in PCM research is to optimize properties and applications of PCMs by fine-tuning complex alloys, generally containing several different elements. Basic ingredients are Sb and/or Te, but then to optimize properties like data retention, switching speed, endurance, etc., various other elements like Ge, In, Ag, Ga, Sc, N etc. are added.<sup>[151–154]</sup> However, such alloys impose major challenges, because it is unclear whether such a composition can be kept stable i) when produced in nanoscale volumes, where some elements preferentially segregate to interfaces (or surfaces), ii) when switched repeatedly between the crystalline and amorphous phase via the liquid phase and thus between different densities and iii) when subjected to high temperatures and electrical fields (gradients) enabling diffusion and electromigration? Therefore, an alternative to complex alloy optimization has been advocated.<sup>[150]</sup> It starts from a single element, Sb in this case. Referring back to the bond characterizing maps in Section 2, probably only Sb, Bi, and possibly As might be suitable as a single elemental phase-change memory since they should exhibit MVB. Indeed, Sb shows the desired property contrast between its amorphous and crystalline phases. However, for Sb it is known that under normal conditions, i.e., standard film thickness of at least several tens of nanometers, the amorphous phase is not sufficient stable against spontaneous crystallization at room temperature and can even show explosive crystallization.<sup>[155,156]</sup> This recent work now demonstrates two strategies, which help to stabilize the amorphous phase of Sb. The first one is increasing the quenching rate by which the amorphous phase (glass) is produced. Ab initio molecular

dynamics simulations show that the stability of Sb against crystallization at room temperature depends significantly on the rate at which it was cooled from the melt. Then, experiments were conducted on actual memories using different electrical pulse shapes, different base temperatures (below room temperature) and different heat dissipation architectures to achieve different quench rates. Indeed, it is found that larger quench rates enlarge the window in which Sb can be produced amorphous. Still, the results are rather distant from what is required for actual memory applications. However, the next step is the confinement of Sb in ultrathin films down to 3 nm in the memory. Indeed, the stability of Sb against crystallization is boosted by more than 100 K in base temperature or by many orders of magnitude in time, when reducing the thickness of Sb from 10 to 3 nm<sup>[150]</sup> (see Figure 21). Although Salinga et al.<sup>[150]</sup> refer to proper literature when stating that “narrowing the confinement of a glass between interfaces with neighboring materials can be an effective way to stabilize it by restricting its structural dynamics,” they nowhere in their article refer to a word related to atomic mobility or viscosity. They also do not attempt to explain why the Sb confined in ultrathin films shows improved stability of the amorphous phase and thus robustness against crystallization. They mention (of course fully justified) the need for systematic investigations of alternative neighboring materials with particular focus on their atomic-scale roughness and rigidity and mention the importance of mechanical stress, but they do not mention engineering the atomic mobility in the PCM, particularly engineering by confinement the viscosity from glass to supercooled melt as primary underlying mechanism to achieve the desired goal. The latter mechanism is advocated in the present review.

In view of the discussion above on the confinement in thin films, this section concludes with the following somewhat

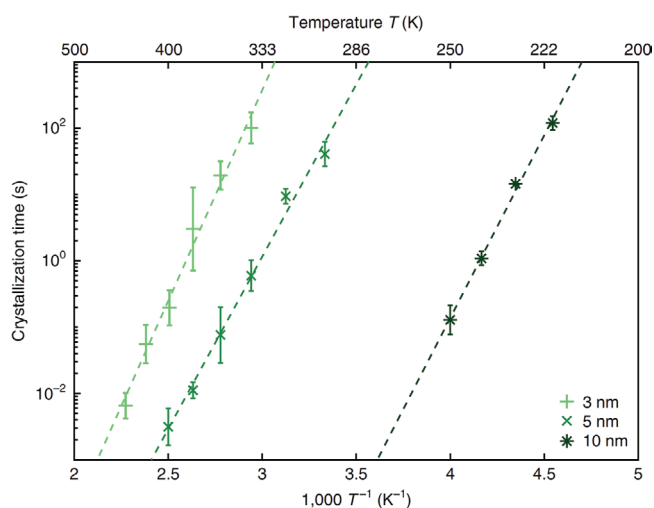


**Figure 21.** Crystallization rate of thin Sb films. Arrhenius plot showing crystallization time, defined as the time after the melt-quenched pulse required to reduce to the device resistance to a value twice the one of a fully crystallized device, versus temperature for three different Sb film thickness. The Sb is confined in-between SiO<sub>2</sub> bottom layer and (ZnS)<sub>80</sub>(SiO<sub>2</sub>)<sub>20</sub> top layer. Reproduced with permission.<sup>[150]</sup> Copyright 2019, Nature Research.

provocative quote from this recent work<sup>[150]</sup> on future research: “As a consequence, in this context, discussions about how a particular composition might be necessary for achieving improved phase change functionality become obsolete. In contrast, quantitative knowledge of effects related to nanoscale confinement emerges as a matter of the highest importance.”

### 3.2. Confinement in Nanoparticles

Although many confinement effects discussed in the previous section for thin films apply as well to nanoparticles (NPs), still it is considered worthwhile to pay more explicit attention to PCM NPs in this section. When a thin film is scaled down to a thickness of 2 nm about 20% of the atoms are at the surface/interface of the film, but when an NP is scaled down to 2 nm this fraction can approach 60%. Although NPs (like nanowires) are currently difficult to incorporate in high density bit arrays, the study of PCM NPs can still be useful to understand confined PCM volumes that will play an increasingly important role in aggressively downscaled phase change memory. In this review, we will only focus on research where PCM NPs have been produced: 1) initially in the amorphous phase allowing the subsequent study of their crystallization behavior and 2) with relatively narrow size distributions such that the role of size effects can be studied in a straightforward manner. Earlier works with large size distribution for GST NPs do not provide a consistent picture on the crystallization.<sup>[157–159]</sup>

Producing monodisperse NPs from PCMs is challenging, particularly when ternary alloys with composition control like Ge<sub>2</sub>Sb<sub>2</sub>Te<sub>5</sub> are desired. Various routes can be pursued to make NPs. The first distinction that can be made is between bottom-up and top-down approaches. The top-down approach typically relies on lithography or using a template with nanoscale pores. The bottom-up approach can be split into chemical methods, typically colloidal wet chemistry, and physical methods, typically based on physical vapor deposition.

#### 3.2.1. Top-Down Approach

The first systematic study of the crystallization of size controlled PCM NPs was performed on cone-shaped PCM particles having a base diameter of about 40 nm and a height of 50 nm as produced by electron beam lithography.<sup>[160]</sup> The NPs and the corresponding blanket films were capped with 10 nm Al<sub>2</sub>O<sub>3</sub>. Different PCMs were studied (GST225, N-doped GST225, Sb<sub>2</sub>Te, Ag+In-doped Sb<sub>2</sub>Te (AIST) and Ge<sub>15</sub>Sb<sub>85</sub>) and in all cases the differences in the crystallization temperature  $T_x$  between the corresponding blanket films and the NPs were not really significant. It can thus be concluded that the sizes of these films and NPs are so large that they can be considered as bulk. Then in a follow-up study high density ordered phase change nanodot arrays were fabricated using a lift-off technique on a self-assembled diblock copolymer template.<sup>[161]</sup> These nanodots had a diameter of about 15 nm and a height of slightly less than 10 nm. Their surface was expected to be

covered by a thin oxide layer since the sample was exposed to air before the SiO<sub>2</sub> capping layer was deposited. The results for GST225 and AIST nanodots are not conclusive, but show some weak evidence that crystallization is shifted to higher temperatures in the dots compared to the blanket films. The results for Ge<sub>15</sub>Sb<sub>85</sub> show that the crystallization temperature increases from 250 °C for the 15 nm thick blanket films to about 320 °C for the nanodots. The texture changes too, when going from the thin film to the nanodot array. This can be well understood, because Sb has a rhombohedral layered structure (with alternating long and short bonds due to a Peierls-like distortion such that Sb bilayers are formed) and is thus a growth dominated material. In thin films, Sb will then grow into large grains having these (bi)layers parallel to the substrate surface, which gives rise, as observed, to (000l) peaks in XRD patterns when hexagonal notation for Sb is used. When the Sb film is broken into very small disconnected dots, large grains cannot form and the tendency that all small crystals will align their (000l) planes parallel to the overall horizontal surface is also lost by the many vertical interfaces introduced into the dot array. Now it is worthwhile to refer back to the recent work on monoatomic phase-change materials,<sup>[150]</sup> where pure Sb can become interesting for memory applications when melt-quenched sufficiently fast and when made in sufficiently thin films. This previous work shows that, when the thin film would be confined also into a very thin channel, the amorphous phase would, as required, be stabilized even more. Of course an alternative, more simple route to stabilize the crystallization of Sb is adding Ge, where  $T_X$  of thick films effectively increases from below room temperature to about 200 °C when going from pure Sb to Ge<sub>10</sub>Sb<sub>90</sub>.<sup>[156]</sup>

### 3.2.2. Bottom-Up Approach: GeTe Nanoparticles

Switching to NPs produced by chemical synthesis, only GeTe NPs have been studied in-depth.<sup>[147,162–164]</sup> The dependence of  $T_X$  on NPs size provides a consistent picture; see also **Figure 22a**.  $T_X$ -values increase for decreasing NP size in a kind of exponential fashion. The smallest GeTe NPs produced with a size of 1.8 nm showed a  $T_X$  of 400 °C, that is about 200 °C higher than the one for bulk GeTe.<sup>[162]</sup> Interestingly, in all the four references (included in Figure 22a), where the size dependence of the crystallization temperature was studied for NPs, it was assumed that the  $T_X$  of bulk GeTe is 170–180 °C. However, recently it has been shown that this temperature holds for oxidized (thick) GeTe films, but that, when oxidation is completely prevented,  $T_X$  is 220–230 °C.<sup>[84,114,115]</sup> So, in principle all NPs with a size of 10 nm or larger in Figure 22a have  $T_X$ -values close to the one of bulk GeTe. Nevertheless, oxidation seems to only suppress the increase in  $T_X$ -with decreasing NP size, like already explicitly shown for thin films in Figure 17d, and therefore cannot explain the clear upward trend in  $T_X$ -with decreasing NP size. Therefore, it is possible that the  $T_X$ -values of NPs with a size of 10 nm or larger are still close to the one of bulk, because their small size increases  $T_X$ , whereas oxidation reduces  $T_X$  so that in the end there is hardly any net effect. The clear upward trend in  $T_X$  with decreasing NP size can be explained by similar arguments as put forward for thin

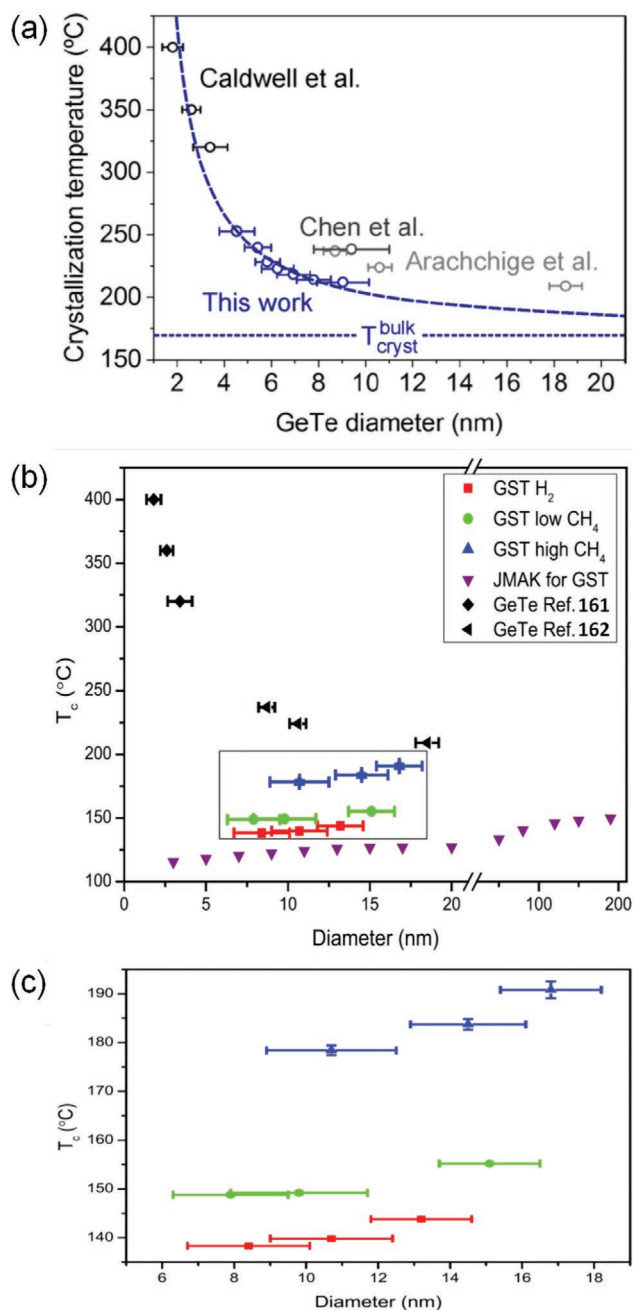


**Figure 22.** Size dependence of the crystallization temperature of PCM nanoparticles. a) Crystallization temperature strongly increases for decreasing GeTe nanoparticle diameter as based on data from four different publications. Reproduced with permission.<sup>[147]</sup> further permissions related to the material excerpted should be directed to the ACS. b,c) Crystallization temperature weakly decreases for decreasing Ge<sub>2</sub>Sb<sub>2</sub>Te<sub>5</sub> nanoparticle diameter. Rectangular box in b is enlarged in c. An effect stronger than the size dependence is observed when the nanoparticles are produced in a gas mixture of either Argon—trace H<sub>2</sub> or Argon—trace CH<sub>4</sub>. Reproduced under the terms of the CC-BY Creative Commons Attribution 4.0 International License (<http://creativecommons.org/licenses/by/4.0/>).<sup>[165]</sup> Copyright 2016, The Authors, published by Springer Nature.

films in the previous section. However, thin films and NPs are rather different and therefore potentially the size effects of NPs require their own arguments.

### 3.2.3. Classical Nucleation Theory

In the most recent publication on GeTe NPs, two explanations for the observed size dependence of  $T_X$  have been given.<sup>[147]</sup> One explanation is based on classical nucleation theory, using the argument that it is required to have one critical nucleus per NPs so that the density of critical nuclei  $N_c$  is directly proportional to the volume of the NP ( $V_{NP}$ ), i.e.:  $N_c = \frac{1}{V_{NP}} = \frac{6}{\pi d_{NP}^3}$ .<sup>[147]</sup> The steady-state nucleation rate is now directly proportional to this density by multiplication with the rate by which an atom attaches to the critical nuclei (in the Volmer-Weber theory) and by the additional multiplication with the Zeldovich factor (in the Becker-Döring theory)<sup>[166]</sup> The temperature dependence of the density of critical nuclei can be of Arrhenius type:  $N_c = N_0 \exp\left(-\frac{\Delta C_c^*}{k_B T_c}\right)$ .

Combining these two equations thus shows that smaller NPs require a higher density of critical nuclei and that this higher density is achieved by an increased crystallization temperature. Indeed, the exponential increase of  $T_X$  with decreasing NP size can be explained in this way. However, this argument is based on homogeneous nucleation. Then, indeed the number of critical nuclei is directly proportional to sample volume. However, for NPs with their exceptionally high surface area ( $A$ ) to volume ( $V$ ) ratio, it is a bit awkward to assume homogeneous nucleation. Instead, if heterogeneous nucleation is assumed, we know that, for thin films with thickness  $d$  and for nanowires and nanoparticles with diameter  $d$ ,  $A/V$  scales with  $1/d$ . So, at a single temperature the density of critical nuclei increases dramatically when  $d$  gets very small. Indeed, for nanowires extensive TEM analysis has shown that the nucleation rate (at a single temperature) due to heterogeneous nucleation scales roughly with  $1/d$ .<sup>[167]</sup> On top of this size effect also the activation energy barrier for nucleation  $E_n$  was, according to the same article, found to be size dependent, i.e., decreases for decreasing  $d$ .<sup>[167]</sup> These authors thus write the overall nucleation rate  $J_c$  in the following manner with respect to a reference having the largest value for  $d$ :  $J_c = J_0 \left(\frac{d^{ref}}{d}\right) \exp\left(\frac{E_n^{ref} - E_n^d}{k_B T}\right)$ . Since the nucleation rate at a single temperature strongly increases for decreasing  $d$ , this heterogeneous nucleation must imply that  $T_X$  decreases with decreasing NP size (or nanowire diameter, or film thickness), opposite to what is observed according to Figure 22a. So, we have an unlikely explanation based on homogeneous nucleation that can fit the data or we have a likely explanation based on heterogeneous nucleation that disagrees with the data. The most likely conclusion is that we should not try to explain the observed size dependence in Figure 22a directly on the basis of classical nucleation theory. In fact, basic assumptions of classical nucleation theory hold for vapor condensation (into liquid or solid) and approximate solidification (without diffusion) well, but it can be debated whether they hold for transformations in solids far out of equilibrium close to  $T_g$ .

### 3.2.4. Entropy Change

The second explanation in ref. [147] for the observed NP size dependence of  $T_X$ , based on entropy arguments, particularly

vibrational entropy, is interesting. The authors start from an equation that is used to explain the size-dependent melting temperature  $T_m$  of (semiconducting) NPs compared to the  $T_m$  of bulk

$$\frac{T_m^{NP}}{T_m^{Bulk}} = \exp\left(-\frac{2(\Delta S_m - R)}{3R\left(\frac{d_{NP}}{d_0} - 1\right)}\right) \quad (2a)$$

with  $\Delta S_m$  the entropy of fusion,  $R$  the gas constant and  $d_0$  a critical diameter of the nanoparticle defined as the size of the nanoparticle for which all atoms are surface atoms. They then replace  $T_m$  by the crystallization temperature  $T_c$  and replace the entropy of fusion with the entropy change due to crystallization  $\Delta S_c$ . The final equation used is then<sup>[147]</sup>

$$\frac{T_c^{NP}}{T_c^{Bulk}} = \exp\left(-\frac{2(\Delta S_c - R)}{3R\left(\frac{d_{NP}}{d_0} - 1\right)}\right) \quad (2b)$$

In fact, Equation (2a) is derived on the basis that  $(\Delta S_m - R)$  is equal to the difference in vibrational entropy  $\Delta S_{vib}$ .<sup>[168]</sup> It may appear surprising that the change in melting temperature of NPs or the change in crystallization temperature of NPs is not related to change in configurational entropy  $\Delta S_{conf}$  when going from the melt to the crystalline state or from the amorphous to the crystalline phase, respectively. Of course,  $\Delta S_{conf}$  is large for these phase transformation, but the central point is that the difference in behavior between NPs and bulk is not dominated by  $\Delta S_{conf}$  but by  $\Delta S_{vib}$ . Note that this equation not only can be used to explain for NPs the melting point depression or an increase in crystallization temperature, but also the other way around, i.e., an increase in  $T_m$  or a decrease in  $T_c$ .<sup>[142,149,168]</sup> For NPs with free surfaces indeed melting point depression and an increase in  $T_c$  are expected since the (near) surface atoms (compared to the bulk) have larger degrees of freedom reducing the stability of the crystalline phase in favor of the liquid or amorphous phase. However, for NPs embedded in certain types of surrounding it can be the other way around. This effect is lost in Equation 2b above because  $(\Delta S_c - R)$  will be negative and therefore only an increase in  $T_c$  for decreasing NP size is predicted. Still, it can describe in an elegant manner for GeTe NPs the change of  $T_c$  for decreasing NP size.

### 3.2.5. Mean-Square Displacement

Equation 2a is derived on the basis of the size-dependent amplitude of the atomic thermal vibrations of NPs in terms of the Lindemann criterion, where the underlying basis can be expressed as<sup>[142,149,159]</sup>

$$\frac{T_m^{NP}}{T_m^{Bulk}} = \frac{\langle \sigma_{Bulk}^2 \rangle}{\langle \sigma_{NP}^2 \rangle} \quad (3a)$$

with  $\langle \sigma_{NP}^2 \rangle$  the average mean square displacement (msd) of the atoms in the NP and  $\langle \sigma_{Bulk}^2 \rangle$  the msd of atoms in the

corresponding bulk crystal. Not only the surface atoms of a nanocluster experience an msd different from the bulk, but also the more interior atoms. In a seminal work, this resulted in the introduction of a critical diameter  $d_0$  (see Equation 2) such that the melting temperature  $T_m$  is not going to zero when the NPs size goes down to zero, but when the NP size goes down to  $d_0$ ,<sup>[142]</sup> which much better agrees with the wealth of experimental data available. A similar argument can come from nucleation theory, where  $T_m$  does not go to zero when the NP size goes to zero, but when the NP size goes down to the size of the critical nucleus. As mentioned above, Equation 3a cannot only describe the melting temperature depression (for free surfaces), but also superheating (for certain types of embedded surfaces). Equation 3a is consistent, in fact should be equivalent to Equation 2a. However, when directly translating Equation 3a to the case of crystallization of NPs

$$\frac{T_c^{\text{NP}}}{T_c^{\text{Bulk}}} = \frac{\langle \sigma_{\text{Bulk}}^2 \rangle}{\langle \sigma_{\text{NP}}^2 \rangle} \quad (3b)$$

this is inconsistent with Equation 2b, because for NPs with free surfaces  $T_c$  decreases for decreasing NP size according to 3b, whereas Equation 2b predicts that  $T_c$  increases for decreasing NP size. So, Equation 3b seems to be wrong. When going from Equation 2a to 2b, there is a change in sign of the entropy, also related to the fact that melting is endothermic, whereas crystallization is exothermic. However, such change cannot be (directly) implemented when going from Equation 3a to 3b. Still, Equation 3 is introduced, because it allows a useful discussion on thermodynamics versus dynamics, where the latter also brings us back to viscosity. Melting is a thermodynamic process close to equilibrium. Crystallization, when starting from the glass phase, is a kinetic process (far) out-of-equilibrium. Crystallization is then not hampered because of an insufficient thermodynamic driving force; it is hampered because of insufficient atomic mobility. So, we have thermodynamic processes like melting where the rate limiting factor is the driving force and we have kinetics processes like crystallization of a glass where the rate limiting step is (atomic) mobility. Using the same basic equations for both processes like in Equations 2 and 3 is thus problematic. Now an increased msd at free surfaces of a solid can have two effects: in the thermodynamic regime it destabilizes the crystalline phase (enabling surface melting and NP melting), but in the kinetic regime it increases mobility that can enable crystallization. These regimes seem well-separated, but particularly for heterogeneous nucleation at free surfaces this is not necessarily true. Surface melting can lead, particularly for NPs, to large melting point depressions closing the gap with the bulk  $T_g$ . Then we have interference between the thermodynamics and the dynamics. Normal glass formation in bulk can already be considered a thermodynamic transition that in practice is masked by the dynamic transition,<sup>[93]</sup> but now for NPs the thermodynamics may again submerge.

The (average) mean-square displacement (msd) is in the context of PCMs particularly used in ab-initio molecular dynamics (AIMD) simulations to derive atomic mobilities, which then via the Stokes-Einstein relation can be related to viscosities.<sup>[169–171]</sup> So, there must be a kind of relation between the msd used in

PCM research and the msd introduced in Equation 3a. However, we have to be careful mixing msd acting on different length and time scales. For surface melting, the msd is related to vibrations, which according to Lindemann criterion are then only a fraction (e.g., 0.15–0.3) of the interatomic distance. For atomic mobilities in PCM, the msd is related to atoms typically escaping the cage formed by its surrounding nearest neighbors. At low temperatures, this cage is quite rigid, and therefore, at short and intermediate times an atom will mainly rattle around within this cage. For longer times, the cage will open up and allow the atom to escape. With decreasing temperature toward  $T_g$ , this opening will take more and more time, and hence, the relaxation dynamics of the particles will slow down.<sup>[93,135]</sup> The cage effect includes the concept of cooperative motion since other particles have to move as well before the cage breaks up and the trapped atom can escape. The correlation length of these cooperative motions rapidly increases when  $T_g$  is approached upon cooling. This distinction between atoms rattling within their cage for intermediate time scales and the escape of atoms from the cage at large time scales in supercooled liquids have been named  $\beta$ - and  $\alpha$ -relaxations, respectively.<sup>[93,134,135]</sup>  $\alpha$ -relaxation resembles the correlation loss in normal liquids, although there is some difference in the time dependence of the relaxation.<sup>[93]</sup>  $\beta$ -relaxation becomes increasingly pronounced (i.e., extends in time) for supercooled liquids when approaching  $T_g$ , such that the  $\alpha$ -relaxation freezes-in at  $T_g$ .<sup>[172–175]</sup> So, in a glass  $\beta$ -relaxation is the major source of glass dynamics and can be associated with local fast atomic motion. A recent study reported the existence of  $\beta$ -relaxation in amorphous PCMs, which can be related to important material properties such as crystallization kinetics.<sup>[176]</sup> Now the point is that the effects of size, confinement and free surfaces can be different for the  $\alpha$ - and  $\beta$ -relaxation and can be different for dynamics and thermodynamics.<sup>[134]</sup> Therefore, currently we lack fundamental understanding to predict how crystallization of a glass or a supercooled liquid just above  $T_g$  will be affected by size, confinement, and free surfaces. So, although Equation 2b can reproduce the size-dependent crystallization temperature of GeTe NPs, it cannot provide with any certainty the mechanism explaining the increase in  $T_X$  with decreasing NP size observed for GeTe NPs.

### 3.2.6. Bottom-Up Approach: $\text{Ge}_2\text{Sb}_2\text{Te}_5$ Nanoparticles

$\text{Ge}_2\text{Sb}_2\text{Te}_5$  NPs, produced via the bottom-up approach, have only been made using magnetron sputtering.<sup>[165,177,178]</sup> This technique is usually applied to grow thin films, but when magnetron sputtering is combined with gas phase aggregation (i.e., enabling nucleation and growth of particles in the gas phase), it can also act as a dedicated nanoparticle source.<sup>[165]</sup> Such a source is a one-step and promising solution-free method to produce NPs. The NPs produced by this method are “clean” (without surrounding ligands), enabling to exclude the possible influence of ligands. Moreover, the relatively narrow size distributions of the produced NPs enable statistical studies on the size dependence of crystallization. Initial work on GST NPs with a diameter of  $5.7 \pm 1$  nm showed that  $T_X$  is  $\approx 180$  °C,<sup>[177]</sup> substantially higher than the one of bulk GST that is 150–160 °C.

Nevertheless, this difference in  $T_X$  probably originates from the difference in stoichiometry, since it was also reported that the composition of the NPs (Ge:Sb:Te = 28:27:45) differed considerably from the nominal stoichiometry of  $\text{Ge}_2\text{Sb}_2\text{Te}_5$  (Ge:Sb:Te = 22:22:56). The composition affects the  $T_X$  of GST ternary alloy pronouncedly.<sup>[179]</sup> For instance, the  $T_X$  of  $\text{Ge}_2\text{Sb}_2\text{Te}_4$  film (which of course is prone to phase separation) is reported as 175 °C.<sup>[61]</sup> Moreover, it is likely that the alumina layer used to embed the NPs also increases  $T_X$ . A striking observation is that the lattice parameter pertaining to the GST NPs, which have the rock-salt structure, is  $\approx 2\%$  larger compared to one of bulk GST.<sup>[177]</sup> Unfortunately, no further information on crystallization of GST NPs with varying sizes has been reported by this group.

Size-dependent crystallization of GST NPs has been presented more recently<sup>[165]</sup> (see Figure 22b,c). The average composition of the NPs was determined (according to energy-dispersive X-ray spectroscopy connected to the TEM analysis) as Ge:Sb:Te = 20:24:56 ( $\pm 1$ ) at%, which agrees well with the nominal stoichiometry of  $\text{Ge}_2\text{Sb}_2\text{Te}_5$ . Depending on deposition conditions both amorphous and crystalline GST NPs were produced. The  $T_X$  of the NPs was derived from in situ heating the amorphous ones in a transmission electron microscope (TEM). Like discussed before, in the case of the results presented in Figure 20a,b, the primary electron beam of the TEM can influence the crystallization process. Therefore, to obtain the results in Figure 22b,c heating was performed without electron beam exposure and only for short intermittent steps selected area electron diffraction (SAED) patterns were recorded with a strongly defocused beam such that the electron dose on the GST is low. Sufficient diffraction intensity is still obtained because on the order of ten thousand NPs contribute to each recorded SAED pattern.<sup>[165]</sup> Therefore, it is not likely that the electron beam influences the crystallization process. Both the as-deposited crystalline NPs as well as amorphous NPs that were crystallized by in situ heating and that showed the rock-salt structure exhibited the 2% lattice parameter expansion compared to bulk GST ( $0.611 \pm 0.002$  nm vs 0.600) as had been observed earlier.<sup>[177]</sup>

The results in Figure 22b,c show that  $T_X$  decreases when the NP sizes decrease, a behavior opposite to what is observed for GeTe NPs. However, the size dependence in  $T_X$  is only a few Kelvin when the sizes of the GST NPs are typically reduced by a factor of 2 (from 17 to 8 nm). Numerical modeling, based on Johnson–Mehl–Avrami–Kolmogorov (JMAK) theory including surface-induced heterogeneous nucleation that was derived from quantitative analysis of this type of nucleation for GST nanowires<sup>[167]</sup> (as described more extensively in Section 3.2.3), could explain the observed weak size dependence.<sup>[165]</sup> So, in this respect the size dependence of the crystallization of GST nanowires and NPs appear fully consistent. Although the modeled data in Figure 22b exhibits the proper size dependence, the predicted absolute  $T_X$  values appear about 20 °C too low. However, in case of the modeling it was assumed that the bulk  $T_X$  (actually the  $T_X$  of an NP having a diameter of 200 nm) is 150 °C. We now know that this is a lower value due to oxidation and that when oxidation is prevented the bulk value should be 170 °C. So, when this new bulk value would be used also the absolute values of the modelled  $T_X$  values would agree excellently with the experimental ones. This may seem paradoxical

and coincidental knowing that these GST NPs are not capped and thus prone to oxidation. However, oxidation does not seem to be a serious issue for these NPs. Typically, the samples (NPs attached to substrate surface) are exposed to air for not more than a few hours to one day before further detailed analysis is performed. TEM images show that oxide shells cannot be observed around these NPs even at atomic resolution.<sup>[165]</sup> Only when the NPs are exposed to ambient conditions for weeks, then a clearly observable germanium-oxide shell with a thickness of  $\approx 2$  nm develops around the NPs.<sup>[180]</sup> Still, the minor surface oxidation might cause surface-induced heterogeneous nucleation and thereby induces the weak size dependence observed in Figure 22b,c. At any rate, the most important conclusion from this work is that this very weak size dependence of GST NPs is favorable for applications in contrast to the strong size dependence observed for GeTe NPs which is a reason for concern, because it probably prohibits the use of GeTe in aggressively downscaled phase-change memory.

### 3.2.7. Carbon Doping in $\text{Ge}_2\text{Sb}_2\text{Te}_5$ Nanoparticles

Clearly more dominant than the size dependence observed in Figure 22c is the effect of carbon doping on  $T_X$ .<sup>[165,178]</sup> The presence of methane gas during the production of GST NPs gives rise to a large increase in  $T_X$  of  $\approx 35$  °C compared to when methane is absent and hydrogen is used instead (see Figure 22c). Although it is difficult to prove that carbon is incorporated in the GST NPs themselves, it is likely, because methane is dissociated in the plasma in which the NPs are produced and then C atoms are present that can actually also act as seeds for NP nucleation. The increase in  $T_X$  due to carbon doping is expected. In GST and GeTe films, carbon doping has been reported as an effective method to stabilize the amorphous phase. For example, 9 at% of carbon in  $\text{Ge}_2\text{Sb}_2\text{Te}_5$  films resulted (compared to the nondoped film) in an  $T_X$  increment of  $\approx 10$  °C. Further, a high amount of doping (18 at% of carbon) led to an increment of 40 °C.<sup>[181]</sup> In GeTe films, carbon doping influences the  $T_X$  more dramatically, where 4% of carbon dopant results in a  $T_c$  of  $\approx 290$  °C compared to  $\approx 180$  °C for the nondoped GeTe film.<sup>[182]</sup> Still, the effect for GST NPs observed here is surprisingly prominent since the partial pressure of methane used during the NP production was very low (less than 1% even with the highest amount of methane) compared to the overall deposition pressure (determined mostly by argon and helium flow and the target atoms).

### 3.2.8. Ultrafast Crystallization of $\text{Ge}_2\text{Sb}_2\text{Te}_5$ Nanoparticles

To close this section on crystallization of PCM NPs, we are also going to consider how the crystallization temperature changes when very high heating rates are employed. Ultrafast differential scanning calorimetry (DSC) employing heating rates in the range of 2 to 40 000 K s<sup>-1</sup> has been applied to  $\text{Ge}_2\text{Sb}_2\text{Te}_5$  films.<sup>[130,97]</sup> This only works fine if a low mass (order  $\mu\text{g}$ ) sample is positioned on the sensor surface. In addition, the sample height must be limited since heating is single sided from the sensor surface to the top of the sample. Thus thermal

gradients emerge with increasing heating rate or sample thickness.<sup>[183]</sup> One of the best choices in this case seems to be deposition of a thin PCM layer directly on top of the sensor surface (leaving the reference sensor clean). However, the high heating rates employed resulted in detachment of the PCM layer from the sensor surface (likely due to the thermal expansion difference). On the other hand, the material could be melted to the sensor. However, since PCMs crystallize before the transition to the supercooled liquid is observed,<sup>[96]</sup> this is not possible. The solution of the problem of good thermal contact was scraping an as-deposited thin film off glass substrates, and placing the flaky powder onto the sensor surface. This of course results in variation in the quality of the thermal contact with the sensor, leading to a spread in peak temperature for a given heating rate. In fitting the data, most weight must then be given to the lowest peak temperature, reflecting the best thermal contact. This seems a reasonable approach to apply the Kissinger method. However, this method thus introduces some drawbacks. Breaking up continuous films in small flakes of uncontrolled size can affect nucleation and growth behavior. For nucleation dominant materials like  $\text{Ge}_2\text{Sb}_2\text{Te}_5$  where the distances between nuclei tend to be much smaller than the flake size, it is not likely that this is a serious effect. More serious is the thermal contact between the flaky loose powder and the sensor surface as was shown by later work particularly for the higher heating rates like  $10\,000$  to  $40\,000\text{ K s}^{-1}$ .<sup>[178]</sup> To overcome these two drawbacks, a single planar flake consisting of GST NPs parallel to the sensor surface was adopted in this later work.<sup>[178]</sup>

The crystallization kinetics of GST NPs with a diameter of about  $16\text{ nm}$ , analyzed in this way using ultrafast DSC, are shown in **Figure 23**.<sup>[178]</sup> The observed crystal growth rates can be explained well by adopting a model for the viscosity of the GST NPs incorporating a fragile-to-strong crossover in the supercooled liquid (but note that this crossover might also be related to the observation that PCM crystallizes from the glass phase at rates below  $10\,000\text{ K s}^{-1}$  and only from the undercooled liquid above this rate<sup>[96]</sup>). Consistent with the results shown in Figure 22b,c, the results in Figure 23 show that a large difference in growth rate exists at relatively low temperatures in the strong regime for the GST NPs produced using either  $\text{H}_2$  or  $\text{CH}_4$  addition to Ar. This difference vanishes at higher temperatures in the fragile regime. This latter effect shows intriguing similarity with the results shown in Figure 20c. A strong difference in crystallization speed was observed between capped and uncapped GST (flakes) at low temperature. Here again a strong difference in growth rate is observed at low temperature, but now between carbon-doped and nondoped GST NPs and this difference vanishes at higher temperatures. So, this is again evidence that factors, like doping, interfaces, nanoscale confinement, have strong effects at low crystallization temperatures, but these tend to disappear (or even might switch to opposite effects) at higher temperatures. This is good news for phase-change memories, because it allows decoupling between low and high temperature processes and thus the possibility to separately optimize data retention, related to ultralow crystallization rates at low temperatures, and switching speed, related to maximum crystallization rates at high temperatures.

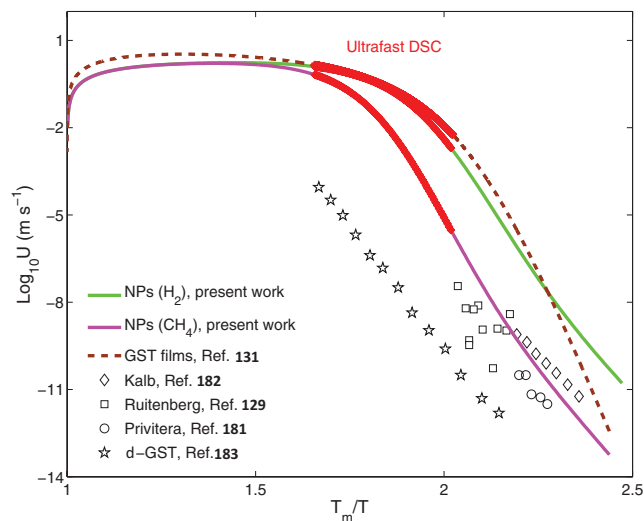


**Figure 23.** The growth rates of  $\text{Ge}_2\text{Sb}_2\text{Te}_5$  nanoparticles (GST NPs) over a wide temperature range. Green and purple solid curves represent the data for GST NPs produced in Ar + trace  $\text{H}_2$  and Ar + trace  $\text{CH}_4$ , respectively. The brown dashed curve is the growth rate for GST films,<sup>[130]</sup> while the open black data points are from direct measurements via TEM,<sup>[131,184]</sup> and AFM.<sup>[185]</sup> The directly measured growth rate for d(oped) GST films is also shown in this figure;<sup>[186]</sup> see the open black stars. The thicker red parts of the curves denote the actual measurement regime accessed by ultrafast DSC.

#### 4. Outlook

The present review has focused on two recent developments in the area of phase change materials, the concept of metavalent bonding and the impact of reduced dimensions. The concept of MVB has been employed to explain the unconventional properties of crystalline phase change materials. MVB has been attributed to the competition between electron delocalization as in metallic bonding and electron localization as in ionic or covalent bonding. This bonding mechanism is not only characterized by an unconventional portfolio of properties but also an unusual bond breaking. Furthermore, it has been demonstrated that these properties can be explained by the octahedral-like atomic arrangement in conjunction with half-filled bands of p-electrons. The resulting electronic structure is prone to the opening of a bandgap, either by Peierls distortions or by charge transfer. Both quantities are closely related to the number of electron shared and electrons transferred between neighboring atoms, i.e., the parameters that span the map in Figure 2. This map hence provides a novel and systematic approach to tailor properties. Yet, for this concept to become more rewarding, a few additional advances are highly desirable. First of all, it would be beneficial to add more data to the map in Figure 2 as well as the 3D maps presented in Figures 9 and 10. Having a higher data density would enable more specific predictions regarding the potential position of sweet spots for specific properties. Along those lines it would be desirable to also include ternary and quaternary alloys to these maps since this would increase the data density significantly.

The present map has focused on binary compounds, hence avoiding the justification of averaging schemes for bond parameters such as ES and ET. This is an important point since



most of the phase change materials presently employed are ternary or even quaternary materials. Hence, it is crucial to identify a roadmap how to tackle such solids. This is straightforward regarding the characterization of properties such as  $\epsilon_{\infty}$ ,  $Z^*$ , the electrical conductivity or ECoN. There are also no major obstacles applying the atom probe to these materials to determine the bond rupture. Recently, APT has even been used already to characterize chalcogenide superlattices<sup>[187]</sup> as well as nanoscale phase separation.<sup>[188]</sup> Hence, regarding the property portfolio and the bond breaking, it is possible to conclude without doubt if a certain solid employs MVB. However, it is still a challenge to determine a unique point for the bonding in the map (Figure 2) for a ternary compound. This can be demonstrated for a prototypical PCM such as  $\text{GeSb}_2\text{Te}_4$  or  $\text{Ge}_2\text{Sb}_2\text{Te}_5$ . As can be seen from Figure 2, the points for  $\text{GeTe}$  and  $\text{Sb}_2\text{Te}_3$  are very close. Hence the charge transfer between Ge and Te is very similar to the one for Sb and Te ( $ET = 0.17$  vs  $ET = 0.13$ ). The same holds for the number of electrons shared between Ge and Te, which is very similar to the one for Sb and Te ( $ES = 1.23$  vs  $ES = 1.24$ ). In this case, we could average both points and would obtain a data point in close vicinity of the two points for  $\text{GeTe}$  and  $\text{Sb}_2\text{Te}_3$  in Figure 2, supporting the argument that  $\text{Ge}_2\text{Sb}_2\text{Te}_5$  also employs metavalent bonding. This conclusion is in line with the unconventional bond breaking observed in the atom probe<sup>[27]</sup> and the unusual properties (the high values for  $Z^*$  for all atoms in the crystal and large values for  $\epsilon_{\infty}$ , as well as the high ECoN of all atoms).<sup>[23]</sup> However, it needs to be checked in each individual case if an averaging procedure as discussed above leads to reasonable conclusions. Therefore, we have only included very few data points for materials like  $\text{AgSbTe}_2$ ,  $\text{Bi}_2\text{Se}_3$  and a few others, where such an averaging procedure has been performed.

Then, it would be highly desirable to extend the 3D maps to additional properties, exploring which other material characteristics can be described by systematic bonding trends. It can be expected that there should be many more materials where the interplay between electron delocalization and electron localization governs the material's behavior. Identifying such materials is hence a highly rewarding goal. Finally, the competition between delocalization and localization should lead to unique phenomena. It would thus appear worthwhile to look for experimental confirmation. Two different areas can be specified where this immediately leads to exciting research questions. Since metavalent bonding is defined by the competition between electron localization and electron delocalization, this immediately raises the question how the borders between metavalent bonding and covalent, ionic, and metallic bonding look like. Will material properties change discontinuously or continuously? Answering this and related questions should even help to better understand one of the fundamental questions in chemistry: "what is the nature of the chemical bond?"<sup>[39]</sup> The discovery of a new, fundamental bonding mechanism provides significant opportunities to reach a better understanding of bonding in general. Due to the competition between electron localization and electron delocalization, there should also be effects due to nanoconfinement. It is highly desirable to verify if indeed bond parameters like ES and ET, as well as characteristic properties like  $Z^*$  and  $\epsilon_{\infty}$ , show significant changes upon confinement.

So far, this topic has hardly been addressed. Yet, we know that MVB is sensitive to (dis)order. Beyond a certain degree of disorder MVB cannot be maintained and a transition to localized covalent bonding occurs. Increasing disorder in crystalline PCMs, that has been attributed to an increasing disorder in the arrangement of vacancies, has been shown to induce a metal-insulator transition (MIT).<sup>[189–192]</sup> A similar transition has also been demonstrated in nanowires<sup>[193,194]</sup> and has been attributed to defect/dislocation formation and subsequent amorphization upon application of electrical pulses. Hence, it should also be possible to (de)stabilize MVB by progressively increasing the influence of boundary conditions. Such boundary conditions can be created readily by reducing the nanoscale thickness of thin films, or the diameter of nanowires and nanoparticles. In this context, it would be highly desirable to know which interfaces promote or destabilize MVB. It is relatively obvious that any interface breaking the symmetry of an ordered octahedral surrounding (like Peierls-like distortions do) or promoting the ionicity in the incipient metal will destabilize MVB (see Figure 7). Therefore, disordered ionic compounds like amorphous oxides are expected to destabilize MVB and promote localized covalent bonding. Indeed, it is generally observed that the crystallization temperature  $T_X$  of PCM films on amorphous oxides like  $\text{SiO}_2$  increase for decreasing film thickness. (In contrast, on metals  $T_X$  often decreases for decreasing film thickness, which might suggest that the presence of MVB is promoted on metals.) Also in Section 2.8 of this review, an interesting case was shown for ultrathin  $\text{GeTe}$  films grown by molecular beam epitaxy (MBE). When a film is grown on a  $\text{Si}(111)-(1 \times 1)\text{-H}$  substrate surface at a temperature as high as  $260^\circ\text{C}$ , well above the crystallization temperature of bulk  $\text{GeTe}$  of  $200^\circ\text{C}$ , it turned out to be initially (up to four bilayers (BLs)) amorphous.<sup>[72]</sup> In contrast, when  $\text{GeTe}$  is grown using the same conditions on the  $\text{Si}(111)-(\sqrt{3} \times \sqrt{3})\text{R}30^\circ\text{-Sb}$  surface, even at lower temperatures like  $230^\circ\text{C}$ , it directly grows with a crystalline structure.<sup>[72]</sup> When the  $\text{GeTe}$  film is grown beyond four BLs on the  $\text{Si}(111)-(1 \times 1)\text{-H}$  surface it switched to an epitaxial structure (for the entire film). The observed behavior can be well explained by (de)stabilizing effects of MVB, where, e.g., above a critical thickness a transition from localized covalent bonding in the amorphous phase to MVB in the crystalline phase is observed.

However, as explained in detail in Section 3 of this review one has to be careful using stability arguments and thus thermodynamics to explain behavior such as low temperature crystallization. Then, thermodynamics hardly plays a role, because the driving force for the crystallization is huge and it is thus not limited by thermodynamics. On the contrary, it is rate limited by atomic mobility, which can be related to viscosity. Nevertheless, it might be interesting to perform systematic (meta-)analyses verifying whether differences in crystallization kinetics can be observed for materials keeping the same type of bonding (metallic glasses, ionic glasses or when covalent in both phases) or when they switch from covalent(-ionic) to MVB. Anyhow, the latter materials are more interesting because they show much clearer property contrast between the amorphous and crystalline phases. Such a kind of meta-analysis has been performed,<sup>[195]</sup> but unfortunately only one incipient metal, the well-known  $\text{Ge}_2\text{Sb}_2\text{Te}_5$ , was included. This work aimed to

correlate the maximum in crystal growth velocity ( $U_{\max}$ ) with parameters like homologous temperature ( $T_{\max}/T_m$ ), reduced glass-transition temperature ( $T_g/T_m$ ), fragility and viscosity at  $T_m$  (where  $T_{\max}$  is the temperature at which  $U_{\max}$  occurs and  $T_m$  and  $T_g$  have the usual meaning of melting temperature and glass temperature, respectively). The results show that high  $U_{\max}$  values, which are desired for PCMs, require low  $T_{\max}/T_m$  (at least below 0.8), low  $T_g/T_m$  (at least below 0.45) and high fragility (although this is of minor secondary importance).  $T_{\max}$  is generally well correlated to  $T_g$  ( $T_{\max} \approx 1.48 T_g$ ). If for instance for automotive applications PCMs must have a data retention of 10 years at 150 °C, and we then assume a  $T_g$  of about 180 °C, then the melting temperature must be at least about 730 °C. This is somewhat higher than the  $T_m$  of most traditional PCMs like  $\text{Ge}_2\text{Sb}_2\text{Te}_5$ . Hence, this also shows that these PCMs cannot fulfill the retention requirements of automotive applications. Moreover, since it is well established that  $T_m$  can reduce dramatically for nanoparticles, it also shows that retention has to be carefully addressed for nanoscale PCM devices. Still, since  $T_m$  is a thermodynamic property also the  $T_m$  of embedded nanoparticles can be raised significantly by proper engineering of the boundary conditions (e.g., interfaces with surrounding material).

Instead of starting from the glass phase and measuring crystallization, which is rate limited by atomic mobility, a potential strategy could be to start with growing ultrathin crystalline incipient metal films at higher temperatures, which are subsequently annealed at temperatures close to the glass temperature (or crystallization temperature for slow heating) of the bulk phase. In this way, indeed it might be possible to observe stability effects of MVB, e.g., that certain boundary conditions destabilize MVB and that measuring electrical conductivity can be a sensitive probe to measure metallic behavior above and nonmetallic behavior below a certain temperature without the need to quench a disordered phase to invoke the localized

behavior. Of course, when pursuing such strategies, one has to be careful not to observe artifacts, e.g., due to intermixing at the interfaces.

A class of materials that appears closely related to incipient metals is transition metal dichalcogenides (TMDCs), since both classes are in principle based on chalcogenides. Moreover, in TMDCs nanoscale confinement has been shown to be of paramount importance. The intense interest in TMDCs particularly originates from their appealing properties when they are scaled down to the single or few layer regime, because for instance semiconductor TMDCs then experience a transition from indirect to direct bandgap and thus exhibit appealing optoelectronic properties. Compared to graphene, TMDCs show a wealth of varying properties as they can be insulators, semiconductors or metals and in this respect thus show a wider range in electrical conductivity than incipient metals. In order to compare TMDCs with incipient metals, or at least with layered  $\text{V}_2\text{-VI}_3$  materials, as well as pseudobinary IV-VI: $\text{V}_2\text{-VI}_3$  compounds, **Figure 24** taken from ref. [196] is instrumental. It compares the vdW gap spacing with a representative distance within the layer, called X-X plane spacing, as clearly defined on the right side of Figure 24. The graph in this figure demonstrates that TMDCs show vdW gap spacings systematically larger than the ones of the other layered compounds. All TMDCs are also found on a single straight line when plotting the vdW gap spacing versus the X-X plane spacing. These results suggest that TMDCs show ideal passivating behavior of the individual vdW blocks and thus suggest pure vdW bonding across the gaps, although this at first hand seems contradictory for metallic TMDCs. In the other layered structures, on the other hand, the vdW gap spacings are smaller, probably because delocalized electrons contribute to the bonding over the vdW gaps and one thus has to be careful calling them vdW gap, because bonding in the gap is not purely of vdW type. The present results thus seem to demonstrate that there is no MVB in

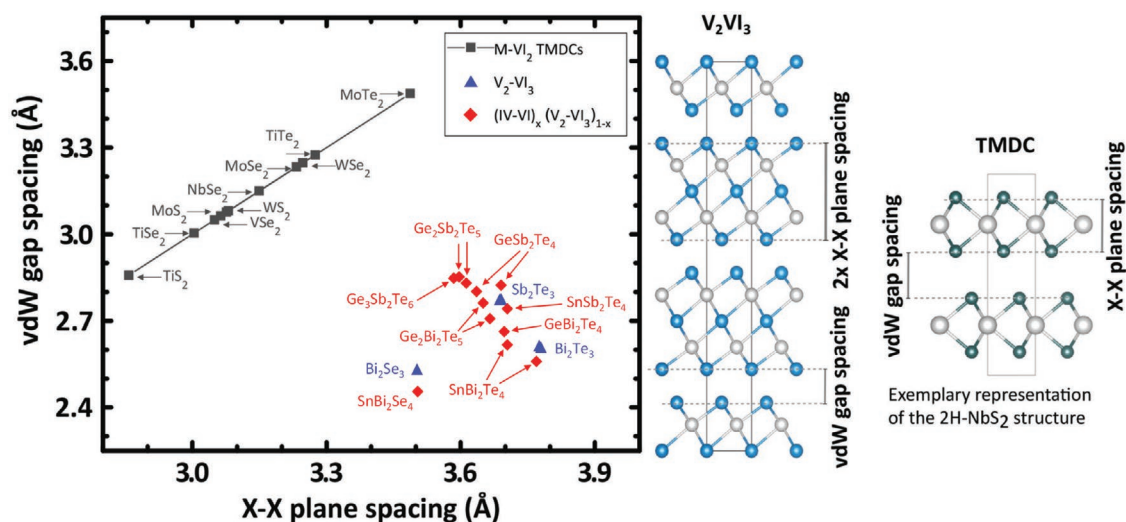


**Figure 24.** Size of vdW gaps versus average chalcogenide X-X plane spacing with X = S, Se, Te of 2D transition metal dichalcogenides (TMDCs), layered  $\text{V}_2\text{-VI}_3$  materials, as well as pseudobinary IV-VI: $\text{V}_2\text{-VI}_3$  compounds. In TMDCs, the X-M-X spacing (M being the metal atom) equals the vdW gap. In  $\text{V}_2\text{-VI}_3$  compounds and their alloys, however, the vdW gap is smaller, giving rise to a stronger coupling compared to TMDCs. Two data points for a single material indicate results obtained from two independent references. Adapted with permission.<sup>[196]</sup> Copyright 2018, Wiley-VCH.

TMDCs and that in layered incipient metals the apparent vdW gap has stronger interactions across these gaps than expected for pure vdW bonding, which can be regarded a fingerprint of MVB.<sup>[197]</sup> These stronger interactions enable strain engineering in layered V<sub>2</sub>-VI<sub>3</sub> materials, something that is not expected for TMDCs, as demonstrated in two recent papers.<sup>[196,198]</sup>

In Section 2.5, Figure 8, it is shown that a kind of forbidden gap is present in the Peierls distortion separating materials possessing MVB and the ones having localized covalent(-ionic) bonding. It appears that MVB can only be maintained for a maximum Peierls distortions of about 1.1. On the other hand, stable covalently bonded systems require at least a Peierls distortion of about 1.2. This can be regarded an additional indication that MVB is not just a result of a gradual transition from metallic to covalent(-ionic) bonding, but that there is a special boundary separating MVB from covalent(-ionic) bonding. In order to refute such a boundary, it is required to find p-bonded materials having a Peierls distortion in the range from 1.1 to 1.2. So, this can be the focus of future research.

## Supporting Information

Supporting Information is available from the Wiley Online Library or from the author.

## Acknowledgements

The authors gratefully acknowledge the help of Carl-Friedrich Schön in designing many of the figures and the animation shown here. Financial support by the Deutsche Forschungsgemeinschaft within SFB 917 ("Nanoswitches") and the Excellence Initiative of the German federal and state governments (EXS-SF-neuroIC005) as well as helpful discussions with Pavel Golub, Jean-Yves Raty, Mathias Schumacher, Julian Pries, Christian Stenz and Shuai Wei are gratefully acknowledged. Simulations were performed with computing resources granted by RWTH Aachen University under project rwth0508 and jara0167.

## Conflict of Interest

The authors declare no conflict of interest.

## Keywords

crystallization kinetics, incipient metals, materials for reconfigurable photonics, metavalent bonding, nanoscale size effects, phase change materials, thermoelectrics

Received: December 18, 2019

Revised: February 3, 2020

Published online: April 3, 2020

[1] X. D. Xiang, X. D. Sun, G. Briceno, Y. L. Lou, K. A. Wang, H. Y. Chang, W. G. Wallace-Freedman, S. W. Chen, P. G. Schultz, *Science* **1995**, 268, 1738.

[2] E. Danielson, J. H. Golden, E. W. McFarland, C. M. Reaves, W. H. Weinberg, X. D. Wu, *Nature* **1997**, 389, 944.

- [3] R. Gremaud, C. P. Broedersz, D. M. Borsa, A. Borgschulte, P. Mauron, H. Schreuders, J. H. Rector, B. Dam, R. Griessen, *Adv. Mater.* **2007**, 19, 2813.
- [4] C. C. L. McCrory, S. Jung, I. M. Ferrer, S. M. Chatman, J. C. Peters, T. F. Jaramillo, *J. Am. Chem. Soc.* **2015**, 137, 4347.
- [5] B. Meredig, A. Agrawal, S. Kirklin, J. E. Saal, J. W. Doak, A. Thompson, K. Zhang, A. Choudhary, C. Wolverton, *Phys. Rev. B* **2014**, 89, 094104.
- [6] G. B. Goh, N. O. Hodas, A. Vishnu, *J. Comput. Chem.* **2017**, 38, 1291.
- [7] Y. Liu, T. L. Zhao, W. W. Ju, S. Q. Shi, *J. Materiomics* **2017**, 3, 159.
- [8] J. C. Phillips, J. A. Vanvechten, *Phys. Rev. Lett.* **1969**, 22, 705.
- [9] J. St John, A. N. Bloch, *Phys. Rev. Lett.* **1974**, 33, 1095.
- [10] K. Gavroglu, A. Simoes, *Neither Physics nor Chemistry: A History of Quantum Chemistry*, MIT Press, Cambridge, MA, USA **2012**.
- [11] P. Ball, *Nature* **2011**, 469, 26.
- [12] A. E. van Arkel, *Molecules and Crystals in Inorganic Chemistry*, Interscience Publishers, New York **1956**.
- [13] J. A. A. Ketelaar, *Chemical Constitution: An Introduction to the Theory of the Chemical Bond*, Elsevier, Amsterdam, The Netherlands **1958**.
- [14] R. F. W. Bader, *Acc. Chem. Res.* **1985**, 18, 9.
- [15] C. Gatti, *Z. Kristallogr.* **2005**, 220, 399.
- [16] R. F. W. Bader, M. E. Stephens, *J. Am. Chem. Soc.* **1975**, 97, 7391.
- [17] X. Fradera, M. A. Austen, R. F. W. Bader, *J. Phys. Chem. A* **1999**, 103, 304.
- [18] G. N. Lewis, *Valence and the Structure of Atoms and Molecules, American Chemical Monograph Series*, The Chemical Catalog Co., Inc., New York **1923**, p. 172.
- [19] J. Y. Raty, M. Schumacher, P. Golub, V. L. Deringer, C. Gatti, M. Wuttig, *Adv. Mater.* **2019**, 31, 1806280.
- [20] P. Golub, A. I. Baranov, *J. Chem. Phys.* **2016**, 145, 154107.
- [21] A. Otero-de-la-Roza, E. R. Johnson, V. Luana, *Comput. Phys. Commun.* **2014**, 185, 1007.
- [22] R. Hoppe, *Z. Kristallogr.* **1979**, 150, 23.
- [23] M. Wuttig, V. L. Deringer, X. Gonze, C. Bichara, J. Y. Raty, *Adv. Mater.* **2018**, 30, 1803777.
- [24] Y. Yu, M. Cagnoni, O. Cojocar-Miredin, M. Wuttig, *Adv. Funct. Mater.* **2019**, 19, 1904862.
- [25] O. Cojocar-Miredin, T. Schwarz, D. Abou-Ras, *Scr. Mater.* **2018**, 148, 106.
- [26] O. Cojocar-Miredin, L. Abdellaoui, M. Nagli, S. Y. Zhang, Y. Yu, C. Scheu, D. Raabe, M. Wuttig, Y. Amouyal, *ACS Appl. Mater. Interfaces* **2017**, 9, 14779.
- [27] M. Zhu, O. Cojocar-Miredin, A. M. Mio, J. Keutgen, M. Kupers, Y. Yu, J. Y. Cho, R. Dronskowski, M. Wuttig, *Adv. Mater.* **2018**, 30, 1706735.
- [28] F. De Geuser, B. Gault, A. Bostel, F. Vurpillot, *Surf. Sci.* **2007**, 601, 536.
- [29] G. D. Costa, H. Wang, S. Duguay, A. Bostel, D. Blavette, B. Deconihout, *Rev. Sci. Instrum.* **2012**, 83, 123709.
- [30] M. Esser, V. L. Deringer, M. Wuttig, R. Dronskowski, *Solid State Commun.* **2015**, 203, 31.
- [31] M. Esser, S. Maintz, R. Dronskowski, *J. Comput. Chem.* **2017**, 38, 620.
- [32] D. Lencer, M. Salinga, M. Wuttig, *Adv. Mater.* **2011**, 23, 2030.
- [33] R. E. Peierls, *Quantum Theory of Solids*, Vol. 23, Oxford University Press, London **1955**.
- [34] C.-F. Schön, M. Wuttig, *3D Map of Materials: Bonding and Properties*, <http://materials-map.rwth-aachen.de/> (accessed: March 2020).
- [35] K. Shportko, S. Kremers, M. Woda, D. Lencer, J. Robertson, M. Wuttig, *Nat. Mater.* **2008**, 7, 653.
- [36] B. Huang, J. Robertson, *Phys. Rev. B* **2010**, 81, 4.
- [37] S. Lee, K. Esfarjani, T. F. Luo, J. W. Zhou, Z. T. Tian, G. Chen, *Nat. Commun.* **2014**, 5, 3525.
- [38] J. Maultzsch, S. Reich, C. Thomsen, H. Requardt, P. Ordejon, *Phys. Rev. Lett.* **2004**, 92, 4.

- [39] L. Pauling, *The Nature of the Chemical Bond*, Cornell University Press, Ithaca, New York **1960**.
- [40] M. Raghuvanshi, O. Cojocaru-Miredin, M. Wuttig, *Nano Lett.* **2020**, *20*, 116.
- [41] G. J. Snyder, E. S. Toberer, *Nat. Mater.* **2008**, *7*, 105.
- [42] D. J. Singh, *Semicond. Semimetals* **2001**, *70*, 125.
- [43] A. F. Ioffe, Infosearch, London, UK **1957**.
- [44] G. S. Nolas, D. T. Morelli, T. M. Tritt, *Annu. Rev. Mater. Sci.* **1999**, *29*, 89.
- [45] L. D. Hicks, M. S. Dresselhaus, *Phys. Rev. B* **1993**, *47*, 12727.
- [46] K. F. Hsu, S. Loo, F. Guo, W. Chen, J. S. Dyck, C. Uher, T. Hogan, E. K. Polychroniadis, M. G. Kanatzidis, *Science* **2004**, *303*, 818.
- [47] B. Poudel, Q. Hao, Y. Ma, Y. C. Lan, A. Minnich, B. Yu, X. A. Yan, D. Z. Wang, A. Muto, D. Vashaee, X. Y. Chen, J. M. Liu, M. S. Dresselhaus, G. Chen, Z. F. Ren, *Science* **2008**, *320*, 634.
- [48] C. J. Vineis, A. Shakouri, A. Majumdar, M. G. Kanatzidis, *Adv. Mater.* **2010**, *22*, 3970.
- [49] E. R. Sittner, K. S. Siegert, P. Jost, C. Schlockermann, F. R. L. Lange, M. Wuttig, *Phys. Status Solidi A* **2013**, *210*, 147.
- [50] M. Cagnoni, D. Fuhren, M. Wuttig, *Adv. Mater.* **2018**, *30*, 1801787.
- [51] G. W. Burr, B. N. Kurdi, J. C. Scott, C. H. Lam, K. Gopalakrishnan, R. S. Shenoy, *IBM J. Res. Dev.* **2008**, *52*, 449.
- [52] M. M. Qazilbash, M. Brehm, B. G. Chae, P. C. Ho, G. O. Andreev, B. J. Kim, S. J. Yun, A. V. Balatsky, M. B. Maple, F. Keilmann, H. T. Kim, D. N. Basov, *Science* **2007**, *318*, 1750.
- [53] J. Rensberg, S. Zhang, Y. Zhou, A. S. McLeod, C. Schwarz, M. Goldflam, M. K. Liu, J. Kerbusch, R. Nawrodt, S. Ramanathan, D. N. Basov, F. Capasso, C. Ronning, M. A. Kats, *Nano Lett.* **2016**, *16*, 1050.
- [54] W. L. Dong, H. L. Liu, J. K. Behera, L. Lu, R. J. H. Ng, K. V. Sreekanth, X. L. Zhou, J. K. W. Yang, R. E. Simpson, *Adv. Funct. Mater.* **2019**, *29*, 9.
- [55] J. L. Bosse, I. Grishin, Y. G. Choi, B. K. Cheong, S. Lee, O. V. Kolosov, B. D. Huey, *Appl. Phys. Lett.* **2014**, *104*, 053109.
- [56] W. K. Njoroge, H. W. Woltgens, M. Wuttig, *J. Vac. Sci. Technol., A* **2002**, *20*, 230.
- [57] W. Welnic, S. Botti, L. Reining, M. Wuttig, *Phys. Rev. Lett.* **2007**, *98*, 4.
- [58] T. P. L. Pedersen, J. Kalb, W. K. Njoroge, D. Wamwangi, M. Wuttig, F. Spaepen, *Appl. Phys. Lett.* **2001**, *79*, 3597.
- [59] B. Bradlyn, L. Elcoro, J. Cano, M. G. Vergniory, Z. J. Wang, C. Felser, M. I. Aroyo, B. A. Bernevig, *Nature* **2017**, *547*, 298.
- [60] M. G. Vergniory, L. Elcoro, C. Felser, N. Regnault, B. A. Bernevig, Z. J. Wang, *Nature* **2019**, *566*, 480.
- [61] M. Wuttig, D. Lusebrink, D. Wamwangi, W. Welnic, M. Gillissen, R. Dronskowski, *Nat. Mater.* **2007**, *6*, 122.
- [62] M. Eddrief, F. Vidal, B. Gallas, *J. Phys. D: Appl. Phys.* **2016**, *49*, 505304.
- [63] K. Chang, J. W. Liu, H. C. Lin, N. Wang, K. Zhao, A. M. Zhang, F. Jin, Y. Zhong, X. P. Hu, W. H. Duan, Q. M. Zhang, L. Fu, Q. K. Xue, X. Chen, S. H. Ji, *Science* **2016**, *353*, 274.
- [64] T. P. Kaloni, K. Chang, B. J. Miller, Q. K. Xue, X. Chen, S. H. Ji, S. S. P. Parkin, S. Barraza-Lopez, *Phys. Rev. B* **2019**, *99*, 134108.
- [65] Y. Tanaka, Z. Ren, T. Sato, K. Nakayama, S. Souma, T. Takahashi, K. Segawa, Y. Ando, *Nat. Phys.* **2012**, *8*, 800.
- [66] B. J. Kooi, B. Noheda, *Science* **2016**, *353*, 221.
- [67] K. Chang, T. P. Kaloni, H. C. Lin, A. Bedoya-Pinto, A. K. Pandeya, I. Kostanovskiy, K. Zhao, Y. Zhong, X. P. Hu, Q. K. Xue, X. Chen, S. H. Ji, S. Barraza-Lopez, S. S. P. Parkin, *Adv. Mater.* **2019**, *31*, 1804428.
- [68] D. M. Zhang, H. Baek, J. Ha, T. Zhang, J. Wyrick, A. V. Davydov, Y. Kuk, J. A. Stroscio, *Phys. Rev. B* **2014**, *89*, 12.
- [69] S. H. Yang, T. J. Zhu, T. Sun, S. N. Zhang, X. B. Zhao, J. He, *Nanotechnology* **2008**, *19*, 5.
- [70] A. Kumar, P. A. Vermeulen, B. J. Kooi, J. Rao, L. van Eijck, S. Schwarzmuller, O. Oeckler, G. R. Blake, *Inorg. Chem.* **2017**, *56*, 15091.
- [71] D. Di Sante, P. Barone, R. Bertacco, S. Picozzi, *Adv. Mater.* **2013**, *25*, 3625.
- [72] R. N. Wang, W. Zhang, J. Momand, I. Ronneberger, J. E. Boschker, R. Mazzarello, B. J. Kooi, H. Riechert, M. Wuttig, R. Calarco, *NPG Asia Mater.* **2017**, *9*, e396.
- [73] I. Hilmi, A. Lotnyk, J. W. Gerlach, P. Schumacher, B. Rauschenbach, *Mater. Des.* **2019**, *168*, 9.
- [74] S. Raoux, J. L. Jordan-Sweet, A. J. Kellock, *J. Appl. Phys.* **2008**, *103*, 114310.
- [75] U. Russo, D. Ielmini, A. Redaelli, A. L. Lacaíta, *IEEE Trans. Electron Devices* **2008**, *55*, 506.
- [76] I. M. L. Billas, A. Chatelain, W. A. Deheer, *Science* **1994**, *265*, 1682.
- [77] A. P. Alivisatos, *Science* **1996**, *271*, 933.
- [78] E. Roduner, *Chem. Soc. Rev.* **2006**, *35*, 583.
- [79] G. Herzer, *Acta Mater.* **2013**, *61*, 718.
- [80] D. A. Porter, K. E. Easterling, M. Y. A. Sherif, *Phase Transformation in Metals and Alloys*, CRC Press, Boca Raton, FL, USA **2009**.
- [81] M. A. van Huis, A. van Veen, H. Schut, B. J. Kooi, J. T. M. De Hosson, *Phys. Rev. B* **2003**, *67*, 235409.
- [82] M. A. van Huis, A. van Veen, H. Schut, S. W. H. Eijt, B. J. Kooi, J. T. M. De Hosson, *Acta Mater.* **2005**, *53*, 1305.
- [83] G. W. Burr, M. J. Breitwisch, M. Franceschini, D. Garetto, K. Gopalakrishnan, B. Jackson, B. Kurdi, C. Lam, L. A. Lastras, A. Padilla, B. Rajendran, S. Raoux, R. S. Shenoy, *J. Vac. Sci. Technol. B* **2010**, *28*, 223.
- [84] P. Noe, C. Vallee, F. Hippert, F. Fillot, J. Y. Raty, *Semicond. Sci. Technol.* **2018**, *33*, 013002.
- [85] X. Yu, J. Robertson, *Can. J. Phys.* **2014**, *92*, 671.
- [86] R. E. Simpson, P. Fons, A. V. Kolobov, T. Fukaya, M. Krbal, T. Yagi, J. Tominaga, *Nat. Nanotechnol.* **2011**, *6*, 501.
- [87] N. Takaura, T. Ohyanagi, M. Tai, T. Morikawa, M. Kinoshita, K. Akita, *Fabrication of Topological-Switching RAM (TRAM)*, IEEE, New York **2014**.
- [88] H. J. Zhang, C. X. Liu, X. L. Qi, X. Dai, Z. Fang, S. C. Zhang, *Nat. Phys.* **2009**, *5*, 438.
- [89] Y. L. Chen, J. G. Analytis, J. H. Chu, Z. K. Liu, S. K. Mo, X. L. Qi, H. J. Zhang, D. H. Lu, X. Dai, Z. Fang, S. C. Zhang, I. R. Fisher, Z. Hussain, Z. X. Shen, *Science* **2009**, *325*, 178.
- [90] J. Kim, J. Kim, S. H. Jhi, *Phys. Rev. B* **2010**, *82*, 4.
- [91] X. B. Li, N. K. Chen, X. P. Wang, H. B. Sun, *Adv. Funct. Mater.* **2018**, *28*, 21.
- [92] B. J. Kooi, J. Momand, *Phys. Status Solidi RRL* **2019**, *13*, 1800562.
- [93] L. M. C. Janssen, *Front. Phys.* **2018**, *6*, 18.
- [94] H. E. Kissinger, *Anal. Chem.* **1957**, *29*, 1702.
- [95] L. C. Chen, F. Spaepen, *J. Appl. Phys.* **1991**, *69*, 679.
- [96] J. Pries, S. Wei, M. Wuttig, P. Lucas, *Adv. Mater.* **2019**, *31*, 1900784.
- [97] J. A. Kalb, M. Wuttig, F. Spaepen, *J. Mater. Res.* **2007**, *22*, 748.
- [98] L. van Pieterse, M. H. R. Lankhorst, M. van Schijndel, A. E. T. Kuiper, J. H. J. Roosen, *J. Appl. Phys.* **2005**, *97*, 083520.
- [99] K. F. Kao, C. M. Lee, M. J. Chen, M. J. Tsai, T. S. Chin, *Adv. Mater.* **2009**, *21*, 1695.
- [100] S. Raoux, H.-Y. Cheng, B. Muñoz, J. Jordan-Sweet, *Proc. E|PCOS* **2009**, [https://2534e415-f50f-44ab-8808-eb608caa1472.filesusr.com/ugd/3d44dd\\_22788a7f40884493a429165fd27a636e.pdf](https://2534e415-f50f-44ab-8808-eb608caa1472.filesusr.com/ugd/3d44dd_22788a7f40884493a429165fd27a636e.pdf) (accessed: March 2020).
- [101] H. Y. Cheng, S. Raoux, Y. C. Chen, *J. Appl. Phys.* **2010**, *107*, 9.
- [102] S. Raoux, W. Welnic, D. Ielmini, *Chem. Rev.* **2010**, *110*, 240.
- [103] M. Zacharias, J. Blasing, P. Veit, L. Tsybesko, K. Hirschman, P. M. Fauchet, *Appl. Phys. Lett.* **1999**, *74*, 2614.
- [104] G. V. M. Williams, A. Bittar, H. J. Trodahl, *J. Appl. Phys.* **1990**, *67*, 1874.

- [105] I. Honma, H. Hotta, K. Kawai, H. Komiyama, K. Tanaka, *J. Non-Cryst. Solids* **1987**, 97–98, 947.
- [106] P. D. Persans, A. Ruppert, B. Abeles, *J. Non-Cryst. Solids* **1988**, 102, 130.
- [107] S. Miyazaki, Y. Ihara, M. Hirose, *J. Non-Cryst. Solids* **1987**, 97–98, 887.
- [108] M. Zacharias, P. Streitenberger, *Phys. Rev. B* **2000**, 62, 8391.
- [109] S. Raoux, H. Y. Cheng, J. L. Jordan-Sweet, B. Munoz, M. Hitzbleck, *Appl. Phys. Lett.* **2009**, 94, 183114.
- [110] H. Homma, I. K. Schuller, W. Sevenhans, Y. Bruynseraede, *Appl. Phys. Lett.* **1987**, 50, 594.
- [111] F. Oki, Y. Ogawa, Y. Fujiki, *Jpn. J. Appl. Phys.* **1969**, 8, 1056.
- [112] S. Raoux, R. M. Shelby, J. Jordan-Sweet, B. Munoz, M. Salinga, Y. C. Chen, Y. H. Shih, E. K. Lai, M. H. Lee, *Microelectron. Eng.* **2008**, 85, 2330.
- [113] B. J. Kooi, W. M. G. Groot, J. T. M. De Hosson, *J. Appl. Phys.* **2004**, 95, 924.
- [114] P. Noe, C. Sabbione, N. Bernier, N. Castellani, F. Fillot, F. Hippert, *Acta Mater.* **2016**, 110, 142.
- [115] R. Berthier, N. Bernier, D. Cooper, C. Sabbione, F. Hippert, P. Noe, *J. Appl. Phys.* **2017**, 122, 115304.
- [116] V. L. Deringer, R. Dronskowski, *J. Appl. Phys.* **2014**, 116, 173703.
- [117] V. L. Deringer, M. Lumeij, R. Dronskowski, *J. Phys. Chem. C* **2012**, 116, 15801.
- [118] L. V. Yashina, R. Puttner, V. S. Neudachina, T. S. Zyubina, V. I. Shtanov, M. V. Poygin, *J. Appl. Phys.* **2008**, 103, 094909.
- [119] J. A. Kalb, Q. Guo, X. Q. Zhang, Y. Li, C. Sow, C. V. Thompson, *J. Microelectromech. Syst.* **2008**, 17, 1094.
- [120] Q. Guo, M. H. Li, Y. Li, L. P. Shi, T. C. Chong, J. A. Kalb, C. V. Thompson, *Appl. Phys. Lett.* **2008**, 93, 3.
- [121] V. Weidenhof, I. Friedrich, S. Ziegler, M. Wuttig, *J. Appl. Phys.* **1999**, 86, 5879.
- [122] I. M. Park, J. Y. Cho, T. Y. Yang, E. S. Park, Y. C. Joo, *Jpn. J. Appl. Phys.* **2011**, 50, 4.
- [123] R. E. Simpson, M. Krbal, P. Fons, A. V. Kolobov, J. Tominaga, T. Uruga, H. Tanida, *Nano Lett.* **2010**, 10, 414.
- [124] R. Pandian, B. J. Kooi, J. T. M. De Hosson, A. Pauza, *J. Appl. Phys.* **2006**, 100, 123511.
- [125] R. Pandian, B. J. Kooi, J. T. M. De Hosson, A. Pauza, *J. Appl. Phys.* **2007**, 101, 053529.
- [126] J. Orava, A. L. Greer, B. Gholipour, D. W. Hewak, C. E. Smith, *Appl. Phys. Lett.* **2012**, 101, 091906.
- [127] C. A. Angell, *Science* **1995**, 267, 1924.
- [128] S. Wei, Z. Evensong, M. Stolpe, P. Lucas, C. A. Angell, *Sci. Adv.* **2018**, 4, 6.
- [129] A. Masuhr, T. A. Waniuk, R. Busch, W. L. Johnson, *Phys. Rev. Lett.* **1999**, 82, 2290.
- [130] J. Orava, A. L. Greer, B. Gholipour, D. W. Hewak, C. E. Smith, *Nat. Mater.* **2012**, 11, 279.
- [131] G. Ruitenbergh, A. K. Petford-Long, R. C. Doole, *J. Appl. Phys.* **2002**, 92, 3116.
- [132] B. J. Kooi, *Phys. Rev. B* **2004**, 70, 12.
- [133] C. L. Jackson, G. B. McKenna, *J. Non-Cryst. Solids* **1991**, 131–133, 221.
- [134] a) C. J. Ellison, J. M. Torkelson, *Nat. Mater.* **2003**, 2, 695; b) R. D. Priestley, C. J. Ellison, L. J. Broadbelt, J. M. Torkelson, *Science* **2005**, 309, 456.
- [135] P. Scheidler, W. Kob, K. Binder, *J. Phys. Chem. B* **2004**, 108, 6673.
- [136] K. Watanabe, T. Kawasaki, H. Tanaka, *Nat. Mater.* **2011**, 10, 512.
- [137] S. Sohn, Y. Jung, Y. J. Xie, C. Osuji, J. Schroers, J. J. Cha, *Nat. Commun.* **2015**, 6, 6.
- [138] *Science* **2005**, 309, 78, <https://science.sciencemag.org/content/309/5731/78.2>.
- [139] H. Weintraub, M. Ashburner, P. N. Goodfellow, H. F. Lodish, C. J. Arntzen, P. W. Anderson, T. M. Rice, T. H. Geballe, A. R. Means, H. M. Ranney, T. R. Cech, R. R. Colwell, H. R. Bourne, B. Richter, I. M. Singer, P. Marrack, D. T. Fearon, A. Penzias, A. J. Bard, W. F. Brinkman, P. A. Marks, B. Vogelstein, K. W. Kinzler, J. M. Bishop, R. N. Zare, G. Schatz, S. J. Benkovic, H. B. Gray, J. S. Valentine, P. J. Crutzen, D. W. Choi, S. Nakanishi, S. M. Kosslyn, J. I. Brauman, D. C. Rees, W. J. Brill, J. Schell, R. Luhrmann, C. L. Will, W. Wulf, G. J. Vermeij, K. J. Arrow, N. J. Smelser, D. L. Anderson, P. H. Abelson, *Science* **1995**, 267, 1609.
- [140] P. Buffat, J. P. Borel, *Phys. Rev. A* **1976**, 13, 2287.
- [141] K. M. Unruh, T. E. Huber, C. A. Huber, *Phys. Rev. B* **1993**, 48, 9021.
- [142] F. G. Shi, *J. Mater. Res.* **1994**, 9, 1307.
- [143] S. L. Lai, J. Y. Guo, V. Petrova, G. Ramanath, L. H. Allen, *Phys. Rev. Lett.* **1996**, 77, 99.
- [144] J. W. M. Frenken, J. F. Vanderveen, *Phys. Rev. Lett.* **1985**, 54, 134.
- [145] J. G. Dash, *Contemp. Phys.* **1989**, 30, 89.
- [146] X. H. Sun, B. Yu, G. Ng, M. Meyyappan, *J. Phys. Chem. C* **2007**, 111, 2421.
- [147] O. Yarema, A. Perevedentsev, V. Ovuka, P. Baade, S. Volk, V. Wood, M. Yarema, *Chem. Mater.* **2018**, 30, 6134.
- [148] K. Lu, Z. H. Jin, *Curr. Opin. Solid State Mater. Sci* **2001**, 5, 39.
- [149] Q. S. Mei, K. Lu, *Prog. Mater. Sci.* **2007**, 52, 1175.
- [150] M. Salinga, B. Kersting, I. Ronneberger, V. P. Jonnalagadda, X. T. Vu, M. Le Gallo, I. Giannopoulos, O. Cococar-Miredin, R. Mazzarello, A. Sebastian, *Nat. Mater.* **2018**, 17, 681.
- [151] M. Wuttig, N. Yamada, *Nat. Mater.* **2007**, 6, 824.
- [152] T. Matsunaga, J. Akola, S. Kohara, T. Honma, K. Kobayashi, E. Ikenaga, R. O. Jones, N. Yamada, M. Takata, R. Kojima, *Nat. Mater.* **2011**, 10, 129.
- [153] M. Zhu, M. J. Xia, F. Rao, X. B. Li, L. C. Wu, X. L. Ji, S. L. Lv, Z. T. Song, S. L. Feng, H. B. Sun, S. B. Zhang, *Nat. Commun.* **2014**, 5, 6.
- [154] F. Rao, K. Y. Ding, Y. X. Zhou, Y. H. Zheng, M. J. Xia, S. L. Lv, Z. T. Song, S. L. Feng, I. Ronneberger, R. Mazzarello, W. Zhang, E. Ma, *Science* **2017**, 358, 1423.
- [155] C. E. Wickersham, G. Bajor, J. E. Greene, *Solid State Commun.* **1978**, 27, 17.
- [156] G. Eising, B. J. Niebuur, A. Pauza, B. J. Kooi, *Adv. Funct. Mater.* **2014**, 24, 1687.
- [157] H. R. Yoon, W. Jo, E. H. Lee, J. H. Lee, M. Kim, K. Y. Lee, Y. Khang, *J. Non-Cryst. Solids* **2005**, 351, 3430.
- [158] H. S. Choi, K. S. Seol, K. Takeuchi, J. Fujita, Y. Ohki, *Jpn. J. Appl. Phys. Part 1* **2005**, 44, 7720.
- [159] G. S. Park, J. H. Kwon, M. Kim, H. R. Yoon, W. Jo, T. K. Kim, J. M. Zuo, Y. Khang, *J. Appl. Phys.* **2007**, 102, 5.
- [160] S. Raoux, C. T. Rettner, J. L. Jordan-Sweet, A. J. Kellock, T. Topuria, P. M. Rice, D. C. Miller, *J. Appl. Phys.* **2007**, 102, 094305.
- [161] Y. Zhang, S. Raoux, D. Krebs, L. E. Krupp, T. Topuria, M. A. Caldwell, D. J. Milliron, A. Kellock, P. M. Rice, J. L. Jordan-Sweet, H. S. P. Wong, *J. Appl. Phys.* **2008**, 104, 5.
- [162] M. A. Caldwell, S. Raoux, R. Y. Wang, H. S. P. Wong, D. J. Milliron, *J. Mater. Chem.* **2010**, 20, 1285.
- [163] I. U. Arachchige, R. Soriano, C. D. Malliakas, S. A. Ivanov, M. C. Kanatzidis, *Adv. Funct. Mater.* **2011**, 21, 2737.
- [164] M. J. Polking, H. M. Zheng, R. Ramesh, A. P. Alivisatos, *J. Am. Chem. Soc.* **2011**, 133, 2044.
- [165] B. Chen, G. H. ten Brink, G. Palasantzas, B. J. Kooi, *Sci. Rep.* **2016**, 6, 10.
- [166] K. F. Kelton, A. L. Greer, C. V. Thompson, *J. Chem. Phys.* **1983**, 79, 6261.
- [167] S. H. Lee, Y. W. Jung, R. Agarwal, *Nano Lett.* **2008**, 8, 3303.
- [168] Z. Zhang, M. Zhao, Q. Jiang, *Semicond. Sci. Technol.* **2001**, 16, L33.
- [169] W. Zhang, I. Ronneberger, P. Zalden, M. Xu, M. Salinga, M. Wuttig, R. Mazzarello, *Sci. Rep.* **2014**, 4, 6.
- [170] M. Ropo, J. Akola, R. O. Jones, *Phys. Rev. B* **2017**, 96, 8.
- [171] G. C. Sosso, J. Colombo, J. Behler, E. Del Gado, M. Bernasconi, *J. Phys. Chem. B* **2014**, 118, 13621.

- [172] A. Pirovano, A. L. Lacaíta, F. Pellizzer, S. A. Kostylev, A. Benvenuti, R. Bez, *IEEE Trans. Electron Devices* **2004**, *51*, 714.
- [173] M. Mitra, Y. Jung, D. S. Gianola, R. Agarwal, *Appl. Phys. Lett.* **2010**, *96*, 222111.
- [174] J. L. M. Oosthoek, D. Krebs, M. Salinga, D. J. Gravesteijn, G. A. M. Hurkx, B. J. Kooi, *J. Appl. Phys.* **2012**, *112*, 084506.
- [175] M. Le Gallo, D. Krebs, F. Zipoli, M. Salinga, A. Sebastian, *Adv. Electron. Mater.* **2018**, *4*, 1700627.
- [176] X. Peng, Y. D. Cheng, J. Pries, S. Wei, H. B. Yu, M. Wuttig, *Sci. Adv.* **2020**, *6*, 8.
- [177] G. E. Ghezzi, R. Morel, A. Brenac, N. Boudet, M. Audier, F. Fillot, S. Maitrejean, F. Hippert, *Appl. Phys. Lett.* **2012**, *101*, 233113.
- [178] B. Chen, G. H. ten Brink, G. Palasantzas, B. J. Kooi, *J. Phys. Chem. C* **2017**, *121*, 8569.
- [179] J. P. Reifenberg, M. A. Panzer, S. Kim, A. M. Gibby, Y. Zhang, S. Wong, H. S. P. Wong, E. Pop, K. E. Goodson, *Appl. Phys. Lett.* **2007**, *91*, 111904.
- [180] B. Chen, V. L. Do, G. ten Brink, G. Palasantzas, P. Rudolf, B. J. Kooi, *Nanotechnology* **2018**, *29*, 10.
- [181] X. L. Zhou, L. C. Wu, Z. T. Song, F. Rao, M. Zhu, C. Peng, D. N. Yao, S. N. Song, B. Liu, S. L. Feng, *Appl. Phys. Lett.* **2012**, *101*, 4.
- [182] G. B. Beneventi, L. Perniola, V. Sousa, E. Gourvest, S. Maitrejean, J. C. Bastien, A. Bastard, B. Hyot, A. Fargeix, C. Jahan, J. F. Nodin, A. Persico, A. Fantini, D. Blachier, A. Toffoli, S. Loubriat, A. Roule, S. Lhostis, H. Feldis, G. Reibold, T. Billon, B. De Salvo, L. Larcher, P. Pavan, D. Bensahel, P. Mazoyer, R. Annunziata, P. Zuliani, F. Boulanger, *Solid-State Electron.* **2011**, *65–66*, 197.
- [183] J. Pries, S. Wei, F. Hoff, P. Lucas, M. Wuttig, *Scr. Mater.* **2020**, *178*, 223.
- [184] S. Privitera, C. Bongiorno, E. Rimini, R. Zonca, *Appl. Phys. Lett.* **2004**, *84*, 4448.
- [185] J. Kalb, F. Spaepen, M. Wuttig, *Appl. Phys. Lett.* **2004**, *84*, 5240.
- [186] A. Sebastian, M. Le Gallo, D. Krebs, *Nat. Commun.* **2014**, *5*, 9.
- [187] O. Cojocaru-Miredin, H. Hollermann, A. M. Mio, A. Y. T. Wang, M. Wuttig, *J. Phys.: Condens. Matter* **2019**, *31*, 204002.
- [188] M. C. C. Rodenkirchen, S. Jakobs, Y. Cheng, J. Keutgen, Y. Yu, M. Wuttig, O. Cojocaru-Mirédin, *Adv. Funct. Mater.* **2020**, *31*, 1910039.
- [189] T. Siegrist, P. Jost, H. Volker, M. Woda, P. Merkelbach, C. Schlockermann, M. Wuttig, *Nat. Mater.* **2011**, *10*, 202.
- [190] W. Zhang, A. Thiess, P. Zalden, R. Zeller, P. H. Dederichs, J. Y. Raty, M. Wuttig, S. Blugel, R. Mazzarello, *Nat. Mater.* **2012**, *11*, 952.
- [191] P. Jost, H. Volker, A. Poitz, C. Poltorak, P. Zalden, T. Schafer, F. R. L. Lange, R. M. Schmidt, B. Hollander, M. R. Wirtsohn, M. Wuttig, *Adv. Funct. Mater.* **2015**, *25*, 6399.
- [192] V. Bragaglia, F. Arciprete, W. Zhang, A. M. Mio, E. Zallo, K. Perumal, A. Giussani, S. Cecchi, J. E. Boschker, H. Riechert, S. Privitera, E. Rimini, R. Mazzarello, R. Calarco, *Sci. Rep.* **2016**, *6*, 31679.
- [193] S. W. Nam, H. S. Chung, Y. C. Lo, L. Qi, J. Li, Y. Lu, A. T. C. Johnson, Y. W. Jung, P. Nukala, R. Agarwal, *Science* **2012**, *336*, 1561.
- [194] P. Nukala, R. Agarwal, X. F. Qian, M. H. Jang, S. Dhara, K. Kumar, A. T. C. Johnson, J. Li, R. Agarwal, *Nano Lett.* **2014**, *14*, 2201.
- [195] J. Orava, A. L. Greer, *J. Chem. Phys.* **2014**, *140*, 214504.
- [196] R. N. Wang, F. R. L. Lange, S. Cecchi, M. Hanke, M. Wuttig, R. Calarco, *Adv. Funct. Mater.* **2018**, *28*, 1705901.
- [197] Y. D. Cheng, O. Cojocaru-Miredin, J. Keutgen, Y. Yu, M. Kupers, M. Schumacher, P. Golub, J. Y. Raty, R. Dronskowski, M. Wuttig, *Adv. Mater.* **2019**, *31*, 1904316.
- [198] P. A. Vermeulen, J. Mulder, J. Momand, B. J. Kooi, *Nanoscale* **2018**, *10*, 1474.